2004

Investigation of pulse compression technique and time-frequency analysis in medical ultrasound imaging

Shyam Venkataraman

Investigation of Pulse Compression Technique and Time-Frequency Analysis in Medical Ultrasound Imaging

by

Shyam Venkataraman

B.E. Thiagarajar College of Engineering, Madurai, India (1989)

A dissertation submitted in partial fulfillment
of the requirements for the degree of Ph.D. in the
Chester F. Carlson Center for Imaging Science
of the College of Science
Rochester Institute of Technology

August 04

Signature of the Author V. Shyam

Accepted by Harvey E. Rhody
Coordinator, Ph.D. Degree Program

8/24/2004
Date

CHESTER F. CARLSON
CENTER FOR IMAGING SCIENCE
COLLEGE OF SCIENCE
ROCHESTER INSTITUTE OF TECHNOLOGY
ROCHESTER, NY

CERTIFICATE OF APPROVAL

Ph.D. DEGREE DISSERTATION

The Ph.D. Degree Dissertation of Shyam Venkataraman
has been examined and approved by the
dissertation committee as satisfactory for
the dissertation requirement for the
Ph.D. degree in Imaging Science

Dr. Navalgund A.H.K. Rao, Dissertation Advisor

Dr. James Vallino

Dr. Joseph Hornak

Dr. Robert Kremens

August 9, 2004
Date

DISSERTATION RELEASE PERMISSION
ROCHESTER INSTITUTE OF TECHNOLOGY
ROCHESTER, NY YORK

INVESTIGATION OF PULSE COMPRESSION TECHNIQUE AND TIME-FREQUENCY ANALYSIS IN MEDICAL ULTRASOUND IMAGING

I, Shyam Venkataraman, hereby grant permission to Wallace Memorial Library of R.I.T. to reproduce my dissertation in whole or in part. Any reproduction will not be for commercial use or profit.

V. Shyam

Shyam Venkataraman

Aug 9th, 2004

Date

INVESTIGATION OF PULSE COMPRESSION TECHNIQUE AND TIME-FREQUENCY ANALYSIS IN MEDICAL ULTRASOUND IMAGING

by

Shyam Venkataraman

Submitted to the Center for Imaging Science
in partial fulfillment of the requirements for the Ph. D.
degree at Rochester Institute of Technology

August 04

ABSTRACT

Linear frequency modulation (LFM) followed by pulse Compression processing has been used extensively in radar, seismic exploration, non-destructive testing and sonar to improve signal-to-noise ratio (SNR). Typically SNR improvement is determined by the transducer bandwidth times the time duration of LFM, also known as time-bandwidth (TB) product. Clinical medical ultrasound is entirely a B-scan imaging modality. A method was developed to incorporate pulse compression within the B-scan protocol. Its effect on the system point spread function (PSF) was examined. In B-scan the axial resolution is limited by the bandwidth of the transducer. Within the context of pulse compression protocol it is possible to apply at the transducer input an amplitude boost function that is the inverse of the transducer frequency response. Thus the output from the transducer is an equalized chirp pulse, with a wider effective bandwidth. Subsequent pulse compression processing preserves this bandwidth and consequently improves the resolution. The improvement that ensues from this step was examined experimentally on wire targets and tissue mimicking phantoms. In B-scan, generally transmit and receive functions are performed by the same transducer. Thus the time duration of LFM gets limited to 10-20 microseconds, consequently limiting the TB product. With separate transmit/receive transducers in cross-beam geometry, we can override this limitation. Now the image has to be created with a C-scan process. The last part of this dissertation examines various processing schemes for this modality. Possibility of using time-frequency distributions such as Short-Time Fourier transform and Wigner-Villet transform has been explored. The PSF was experimentally measured and evaluated for different schemes.

DEDICATION

This dissertation is dedicated to my father, Late Capt. C.N. Venkataraman (Retired Indian Airlines Commander). Flying high at 33,000 feet in an Airbus A300, you never failed to amaze me.

May Your Soul rest in Peace

ACKNOWLEDGEMENTS

I would like to thank Dr. Naval Rao, my advisor and a good friend, who was my single most catalyst and helped to create this document and its associated research the single most significant accomplishment of my life. His guidance, tireless patience, wisdom and inspiration has taught me so much more than he realizes. I will always be indebted to you to having for having brought this dissertation to a completion.

I would like to immensely thank Dr. Robert Kremens, Dr. Joseph Hornak, and Dr. James Vallino for their generous efforts monitoring the quality of this doctoral research and their informative advice.

I would like to thank my wife, Rajasree, for her entire devotion to my family, juggling work and taking full care of my family such that I can fully concentrate on completing this academic pinnacle.

I would like to thank my son, Ashwin, who loves to attend Montessori school even on Sundays and has brought me luck and happiness.

I would like to thank my second child who is currently in his/her fourth month growing within my wife for he/she is God's gift to us.

I would like to thank my parents for giving me the strength and foundation materially and spiritually that have accompanied me to come to this point. I could not have done this without their unselfish support.

I gratefully acknowledge the financial support provided by the Center for Imaging Science at RIT, Whitaker Foundation, Questra Corporation and Hewlett-Packard Company.

I would like to thank Dr. Kit Mayberry being kind and understanding during my time of need.

Finally, I would like to thank all my friends, colleagues and well-wishers at the Rochester Institute of Technology for their innumerable comments, inspirations, and encouragement to this research, especially, Prof. Nitin Sampat, James O'Hara, Di-Yuan Zheng, Amit Gupta, Ramesh Nagarajan, Rajeev Raman, Sumat Mehra amongst others.

Table of Contents

LIST OF TABLES

LIST OF FIGURES

Symbols and Abbreviations

A(t): Amplitude modulation function
B: Bandwidth of the signal
f_i: Instantaneous frequency
f_0: Center frequency of the transducer
SNR: Signal-to-noise ratio (in dB) = 20log(signal amplitude/noise standard deviation)
t: Time
μs : Microseconds
TB: Time-bandwidth product
RF: Radio-frequency waveform
2D: Two-dimensional image
3D: Three-dimensional image
B-scan: Brightness scan, this is the scanning mode used by all the clinical ultrasound scanners
F: Frequency
Axial resolution: In a B-scan protocol, the resolution seen along the beam axis of the transducer
Lateral resolution: In a B-scan protocol, the resolution seen perpendicular to the beam axis of the transducer
$\alpha(\mathbf{f})$: Frequency dependent attenuation in soft tissue
MHz: Mege Hertz = 10^6 Hertz
z or **z**: Propagation distance from the transducer face
dB: decibel
MI : Mechanical Index = peak negative pulse pressure(in megaPascal)/ $\sqrt{\textbf{frequency}}$
FWHM: Full width at half maximum
FM: Frequency Modulated
T: Time duration of the FM pulse
* : Convolution operation with respect to time t between two time signals
$\mathbf{t_o}$: two way travel time from the transducer to the scatterer.
a : scattering strength of the scatterer in question
n(t): additive electronic noise
p(t) : echo signal from the scatterer received by the transducer
$\otimes$: Cross-correlation operation with respect to time t between two time signals
$\delta(\mathbf{t}-\mathbf{t}_o)$: A delta function or a spike centered at t=to
T.B : Time-Bandwidth product = (time duration of FM signal) x (frequency sweep of the FM)

Δt : FWHM (Full width at half maximum) pulse time width of the compressed short pulse

μs : Microseconds

d_1 and d_2 : distance to the center of cross beam from the transmit and receive transducers respectively

c : speed of ultrasound in the medium

$\Delta\tau$: transmit to receive travel time difference between two scatterers; one at the center of the cross-beam region and the other at some off center location in the X-Y plane

TFR : Time-Frequency Representation of a non-stationary signal

t-f plane: time-frequency plane that gets defined when a TFR of a time signal is computed

WV : Wigner-Ville Distribution. This is a quadratic TFR

STFT : Short Time Fourier Transform. This is a linear TFR

PSF : Point Spread Function. Two dimensional image of a point scatterer (or wire target) generated when scanning is performed by any given imaging system or protocol

Chapter 1

INTRODUCTION AND MOTIVATION

As defined in the Webster Collegiate dictionary, ultrasound is defined as *vibrations of the same physical nature as sound but frequencies above the range of human hearing.* Ultrasound imaging is fundamentally a non-reconstructive or indirect form of imaging where the image formation is obtained by localizing an ultrasonic wave to a small volume in a three dimensional (3D) space. An ultrasound imaging system conveys information about echo generating objects. An ultrasound image depicts the multi-dimensional spatial distribution of some object dependent value.

Pulse compression (a.k.a. pulse coding) is a signal processing procedure that converts a long duration low amplitude signal to a short duration high amplitude output as depicted in figure 1.

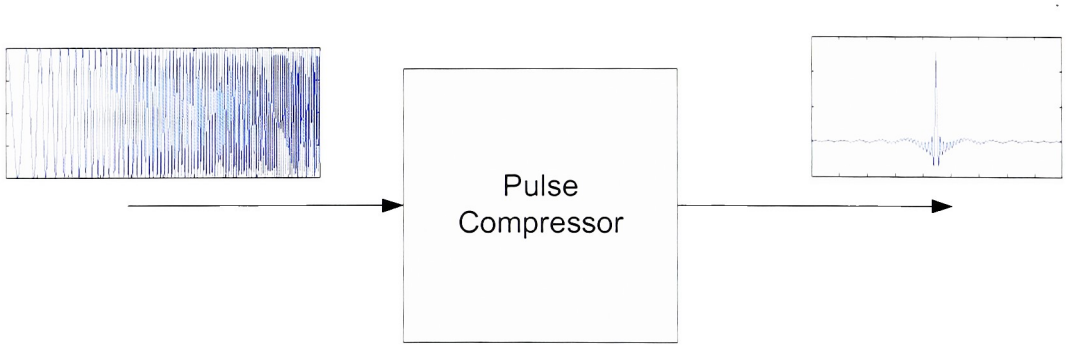

Figure 1: A simplified pulse compression system

Pulse compression techniques have been used extensively in radar, seismic exploration, non-destructive testing and sonar. With the advent of customized Application Specific Integrated Circuits (ASIC) and low-cost memory components, pulse compression has made inroads in to the field of medical ultrasound, even satisfying the real-time processing requirement. A major limitation of present ultrasound techniques is imposed by the frequency-dependent attenuation in soft tissue. Even to a lay person, the image quality perceived upon observing a scanned ultrasound image is rated at average to poor. An enhancement to the signal-to-noise ratio (SNR) is theoretically obtainable using pulse compression technique and it is equal to the product of signal duration and signal bandwidth. This implies that the peak amplitude of the compressed short pulse output (in Figure 1) is greater than the peak amplitude of the input Frequency Modulated (FM) pulse by a factor equal to the square root of the time-bandwidth product.

According to diffraction theory, the resolution of an ultrasonic imaging system increases with the frequency of the ultrasound. However, as per Food and Drug Administration (FDA) specifications, frequency is restricted to a maximum of 5 MHz for abdominal and fetal studies. If safety and nonlinearity were not an issue, the image quality could be increased by increasing the peak intensity of the probing short pulse indefinitely. Moreover, the tissue as a medium responds nonlinearly when subjected to high-intensity pressure waves, resulting in distortion and higher harmonics as it propagates in the medium. Bio-effects due to cavitation and heat production due to non-

linear phenomena prevent the increase of the peak amplitude of the probing pulse. The need to replace high intensity short pulse, with pulse compressed processing is obvious.

I. LITERATURE REVIEW

The pulse compression technique was invented during the early 1950-1960's and was widely used in radar to overcome peak power limitations [9-20], but it was not until the late 70's that it was introduced to the field of medical imaging [22]. With the advent of faster digital signal processing power and complex transducer configurations, pulse compression is once again favored by many investigators [25, 29, 32]. In addition, one has to consider the inherent capabilities of the ultrasound imaging system and cannot directly apply radar principles to pulse compression. Rao[58] has shown in medical ultrasound through system modeling and simulations that frequency-dependent attenuation in soft tissue will limit the attainment of a large time-bandwidth (TB) product.

One of the byproducts of using pulse compression is the artifact generated by sidelobes for which various techniques have been devised. The point spread function (lateral and axial resolution) for a conventional ultrasound imaging system is generally well understood [27, 30, 33]. Numerous investigators have used linear frequency modulation using chirp signal excitation as one form of pulse coding. Rao[41] and O'Donnell[29] have discussed the improvement in signal-to-noise ratio using coded

excitation. Pollakowski[20] has used a combination of pulse compression and inverse filtering as a method to improve the axial resolution of an acoustical imaging system.

Traditional Fourier transform techniques have been used to characterize stationary signals either in time (spatial) domain and frequency domain. This theory has been extended to characterize non-stationary signals using the information provided by joint time-frequency distributions. Hlawatsch et. al[69], Flandrin[67], Cohen[71] and Qian[70] amongst others have created comprehensive tutorials and have compared various time-frequency distributions and transformations. The application of joint time-frequency transformation in medical ultrasound has been few and far between [64, 65].

II. OVERVIEW OF SOLUTION

The main contributions of this thesis are:

- To develop a prototype ultrasound imaging system to investigate the applications of pulse compression. A system architecture that will allow for optimal change to the workflow mechanism including pre- and post-processing steps to capture useful signature data.
- A new adaptive method will be designed to implement an "inverse boost filter" that will compensate for the effect of transducer frequency response and improve resolution in medical ultrasound.

- A method using joint time-frequency transformation specifically information provided by the time (spatial) and frequency domain will be used to emphasize the overall system detection characteristics.

During the course of executing this Ph.D. project, the following papers were published related to pulse compression and ultrasound imaging:

- S. Venkataraman and N.A.H.K. Rao, "Combining pulse compression and adaptive signal design to inverse filter the transducer system response and improve resolution in medical ultrasound", *J. Medical & Biological Engineering & Computing,* vol. 34, pp. 318-320, 1996.
- N.A.H.K. Rao, S.Venkataraman and R. Raman, "Medical ultrasound imaging with frequency modulated pulse: A new technical approach", presented at America Institute of Medicine Annual Conference, March 1996.
- N.A.H.K. Rao, S. Mehra, J. Bridges and S. Venkataraman, "Experimental point spread function of FM pulse imaging scheme, *Ultrasonic Imaging,* vol. 17, pp. 114-141, 1995.
- N.A.H.K. Rao, P. Chandraroy, S. Venkataraman and Dong-li Yang, "Pulse coding in medical ultrasound: some possible applications", *Acoustical Imaging,* vol. 21, pp. 281-290, Plenum Press.

- N.A.H.K. Rao, S. Venkataraman and Y. Zhang, "On the role of system point spread function in scattering structure characterization with ultrasound", *J. Acoustical Soc. America*, 1995.

III. ORGANIZATION OF DISSERTATION

The research and development in pulse compression is divided into modules of theory of pulse compression processing, combining pulse compression and adaptive drive signal design to inverse filter the transducer system response and improve resolution in medical ultrasound and signature detection using time-frequency analysis.

The dissertation is organized as follows:

- **Chapter 2** gives a brief introduction to theory behind ultrasound reflection imaging and various scanning formats.
- **Chapter 3** describes the mathematical theory behind pulse compression processing and introduces the properties of linear frequency-modulated (FM) signals.
- **Chapter 4** describes the concepts behind derivation of a synthetic drive signal that could be used to inverse filter the transducer characteristics.
- **Chapter 5** describes the experimental results of using the inverse boosted drive signal processing both in attenuating and non-attenuating media.

- **Chapter 6** describes the mathematical theory and concepts behind time-frequency (TF) analysis.
- **Chapter 7** describes the experimental analysis and results using TF analysis to capture the signature of output waveforms.
- **Chapter 8** summarizes briefly the findings of the dissertation and future opportunities.

Chapter 2

BACKGROUND

I. ULTRASOUND REFLECTION IMAGING

A complete ultrasonic medical imaging system in reflection model is shown in Fig. 1. The object is generally three-dimensional (3D) and the object property refers to 3D spatial distribution of acoustic speed and density (in combination representing the acoustic impedance) and absorption coefficient and relaxation processes. The input probe is a short duration (a few microseconds) interrogating pulse generated by an ultrasonic transducer and the echo signal is generally received by the same transducer. The echo signal or the backscattered time series is produced by the interaction of the pulse with the object being imaged as depicted by the system box labeled "object-pulse interaction". The received signal is used to create a one-dimensional (1D) image along the line of sight of the transducer. Collection and display of several adjacent lines creates a raster two-dimensional (2D) image. A complete understanding of an ultrasonic imaging system includes cascaded chain of subsystems starting from the object property to be imaged to the human observer as the final interface.

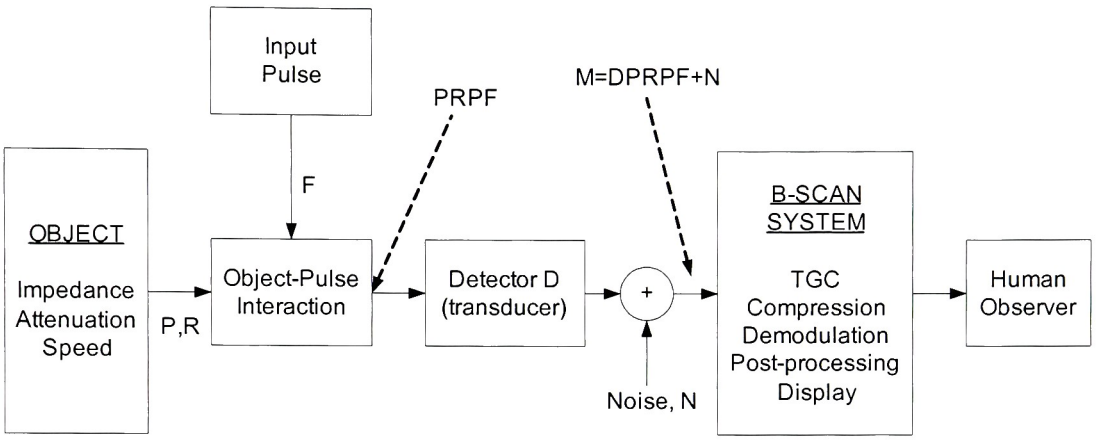

Figure 2: Block diagram of an ultrasound imaging system

Let us attempt to describe the above workflow with some simple physics. Let us assume that we are interested in the backscattered field from a small region of interest (ROI). Let "P" be the actual pulse arriving at ROI from the propagator. This gets modified due to some complex reflection process and is depicted as "R". The ROI now acts as a source of backscatter sound (RPF) which propagates back through the medium towards the transducer. The pulse arriving at the transducer is represented by PRPF and the detected signal is DPRPF + N where "D" stands for the transducer linear system response and "N" stands for additive noise. M = DPRPF + N is the received signal which is the fundamental equation that describes the system box labeled "object-pulse interaction". In actuality,

this equation is very complex and involves integration over several variables, and will be described in next section. As a system, it is neither linear nor shift invariant. But in practice, the overall system is assumed to be piecewise linear and shift-invariant.

II. ANALYTICAL SYSTEM MODEL

Medical ultrasound imaging systems attempt to visually represent the characteristics of the tissue microstructure by analyzing a particular mechanical property of the tissue. There are several factors that contribute to the shape of the reflected radio-frequency (RF) waveform. A source excites a transducer with a short duration pulse. This short pulse then propagates into the body where it is reflected by mechanical inhomogenities in the body. Reflected pulses propagate back to the transducer with a round trip delay,

$$t_{echo} = 2z/c \tag{2.1}$$

where z, is the depth of the transducer and c is the speed of propagation of sound through the medium. The cross-section of the ultrasound beam from the transducer determines the lateral extent of the reflected signal. One line of the image is obtained by recording the reflected signal as a function of time.

Macovski[30] derives a basic reflection imaging system with the following assumptions. First, the diameter of the transducer is assumed to be very large compared to the wavelength of the propagation wave. Second, the wave propagates with a velocity

c which is uniform throughout the medium of propagation and is attenuated with an attenuation coefficient α which is also uniform. Third, the target is modeled as an array of isotropic scatterers having a reflectivity, $R(x, y, z)$ which is assumed to be independent of the angle of approach of the ultrasound beam. It is also assumed that the medium is weakly reflecting in that the second order reflections are negligible.

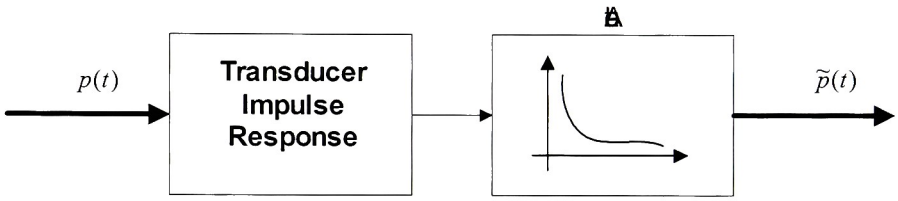

$$e(t) = K\left| \iiint \frac{e^{-2\alpha z}}{z} R(x,y,z)s(x,y)\tilde{g}\left(t - \frac{2z}{c}\right) dxdydz \right|$$

Figure 3: System model of a reflection imaging system

The simplest form used to describe a two-dimensional (2D) ultrasound imaging system is,

$$e(t) = K\left| \iiint \frac{e^{-2\alpha z}}{z} R(x,y,z)s(x,y)\tilde{p}(t - \frac{2z}{c})dxdydz \right| \qquad (2.2)$$

where,

- K is a normalizing constant
- $R(x, y, z)$ is the reflectivity of the body where reflection from the tissue is modeled as an array of isotropic point scatterers

- α is defined as the amplitude attenuation coefficient which is frequency dependent with a slope of 0.5 dB cm^{-1} MHz^{-1} in tissue
- $s(x, y)$ is the lateral distribution of the propagating wave
- $\tilde{p}(t - 2z/c)$ is the received pulse delayed by the round trip time and modified by various linear processes.

The received pulse $\tilde{p}(t)$ is the convolution of the transmitted pulse with the impulse responses of the transducer and other linear filters in the system. The absolute value represents the envelope detection which is phase insensitive. The factor $1/z$ is the loss in amplitude due to diffraction from each scatterer. For transducers operating in piston mode, we can assume that the effect due to diffraction is negligible resulting in $s(x, y)$ being constant over the face of the transducer and zero otherwise.

The resultant signal can be further simplified into a convolution form to be evaluated at $x = 0, y = 0$ as follows,

$$e_c(t) = K\left|R(x, y, \frac{ct}{2}) *** s(-x,-y)\tilde{p}(t)\right| \tag{2.3}$$

where *** represents a 3D convolution.

The brightness-scan (B-scan) represents by far the most widely used modality in ultrasonic imaging and will be explained in the following section. It provides a direct representation of the cross-sectional anatomy that can be readily evaluated. An estimate of the reflectivity in the Y_0 plane is given by,

$$\hat{R}(x, y_0, z) = K\sum_{n=0}^{N} \left| R(x, y, z) *** s(x, y)\tilde{p}(\frac{2z}{c}) \right| \qquad (2.4)$$

III. SCANNING AND DISPLAY FORMAT

There are four commonly used methods to display ultrasound echo data which they vary based upon complexity and amount of processed data.

3.1 A-scan Mode

This is the simplest mode in which a one-dimensional (1D) display of the transducer voltage versus time signal is generated by the echoes. It is readily observed by connecting the received output to an oscilloscope triggered at the instant of initial excitation. If the ultrasound propagation speed c in the object is constant, time t_{echo} represents the range distance z. A large amount of information is contained in the radio-frequency (RF) signal. The disadvantage of A-scan mode is that it provides information about the object only along the line of sight and within the beamwidth of the transducer. It is tedious and time consuming to move the transducer laterally, hence this modality cannot be used for real-time imaging applications. Furthermore, a large amount of spatial information has to be interpreted by the observer rapidly. A-scan mode is mainly used in eye examinations where precise measurement of the axial length of the eye is required.

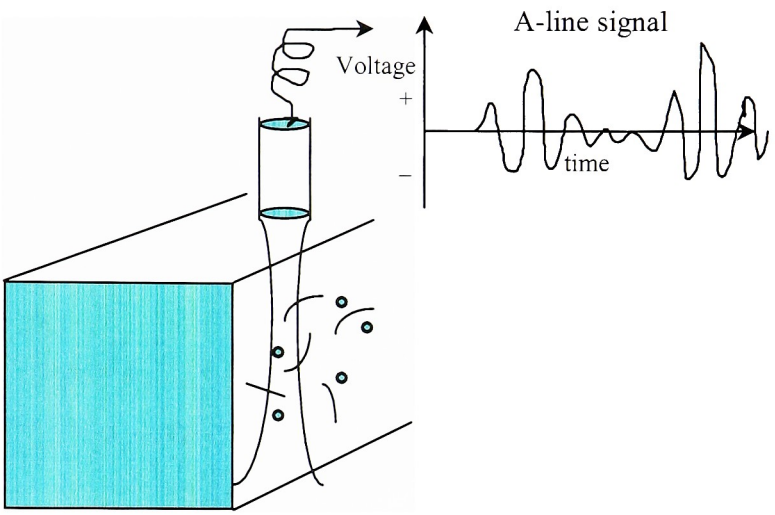

Figure 4: A-scan mode

3.2 B-scan Mode

This is the most commonly used mode and is used to display a grayscale/raster image of the target. Even though there are various forms of scanning arrangements such as linear scan, sector scan or compound scan, B-scan is essentially display of adjacent A-scan signals that are generated when the transducer is moving laterally. Only the envelope or the amplitude of the RF signal is used in the display. The movement of the transducer can be mechanical or the more recent 1D phased array transducer can be used. This modality is particularly suited for the development of fast scanning techniques that can produce real-time images. In one particular scanning technique called sector scan, the direction of the beam is varied by tilting the face of the transducer. A 2D image is generated in the X-Z plane determined by the range direction and scanning direction.

The brightness in the image provides a crude picture of the scatterers/reflectors located along a thin slice in the X-Z plane of the object. The point-spread-function (PSF) which is an image quality metric will be defined later. This PSF is not the same at various locations in the image.

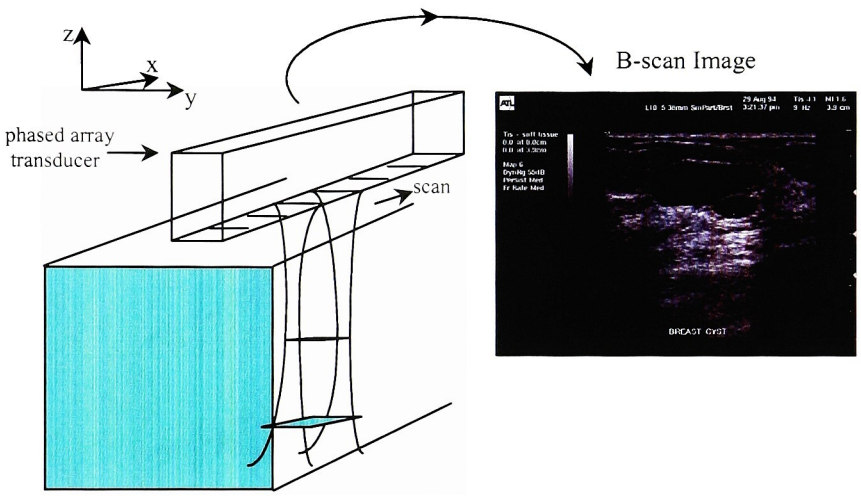

Figure 5: B-scan mode

3.3 C-scan Mode

C-scan refers to constant depth scanning mode that utilizes pulse-echo signals. Here, an electronically gated portion of the A-scan signal is used in a brightness-modulated display. The transducer has to be scanned laterally in the X-Y plane for this modality. The brightness image provides a picture of the scatterers/reflectors located in a thin slice in the X-Y plane of the object at a distance z_0. The advantage is that the transducer beam can be focused to a particular depth and optimal resolution can be

maintained at all portions of the image. A major disadvantage is that 2D scanning requires considerable time to acquire the data. Real time imaging is difficult even with 2D phased arrays at the present time, but future designs of 2D phased array scanners could make it feasible. For this reason, this modality has found applications in non-destructive testing (NDT) and is rarely used in medical imaging.

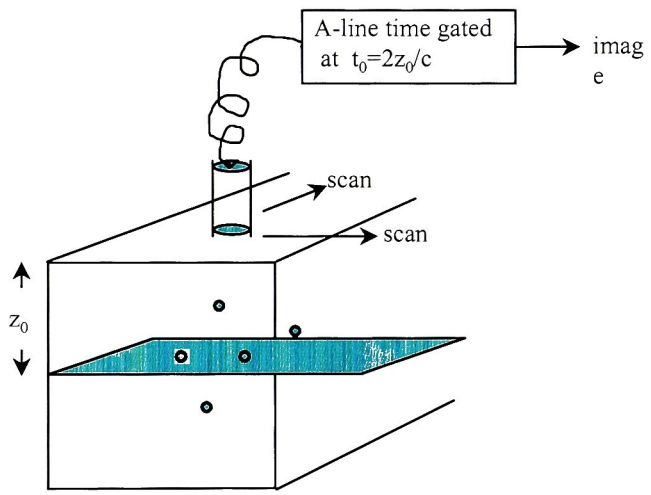

Figure 6: C-scan mode

3.4 M-scan Mode

M-scan mode is used to monitor changes in the A-scan as a function of time. The transducer is held at a fixed location and the A-scans for echoes arriving from the line of sight are recorded at regular intervals of time. The modulated brightness is displayed as a function of depth (vertical axis) and time (horizontal axis). It is used to detect pattern of time movement of a reflector/scatterer mainly along the line of sight. M-scan mode is

primarily intended for imaging large solid tissue displacements. Because it is based on amplitude demodulation of the ultrasonic echo, M-scan mode only offers course resolution (~ 10mm) limited first by the wavelength of the ultrasound and subsequently by the digitization rate of the received echo or the display pixelation. A typical example of an application of this modality is the examination of the pattern of movement of the heart valve leaflets.

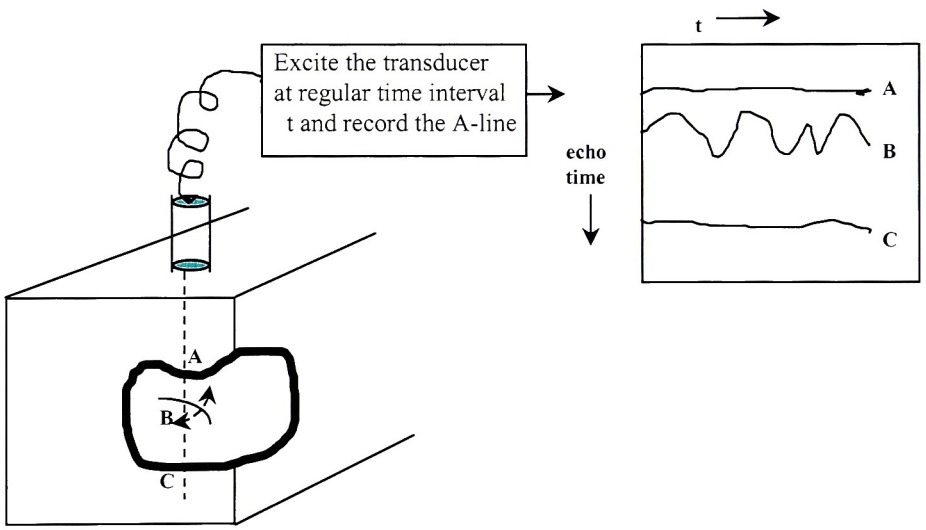

Figure 7: M-scan mode

IV. SPECKLE

Speckle as an artifact is inherent in various types of coherent imaging including holography, radar astronomy, synthetic aperture radar (SAR), astronomical imaging, etc. Speckle was originally defined in the field of optics and detailed analysis can be found in

[28, 33, 55, 56, 58, 59, 75]. When a surface is illuminated by coherent light such as laser, the light reflected by the surface includes contributions from various independent scatterers. At a given observation point, components of the received signal from these different areas interfere resulting in an intensity granularity pattern or mottled structure called speckle. Constructive interference leads to bright spots while destructive interference leads to dark spots. The interference process due to the sub-resolution scatterers results in a mottled appearance in coherent imaging.

In ultrasound imaging, relatively narrow bandwidth pulses are used resulting in coherent summation of the backscattered echoes upon reception. The major difference in pulse-echo imaging is that scattering arrives from inhomogenities within a tissue volume rather than from a surface. The granularity in intensity is caused due to the fact that these inhomogeneities make most tissue rough on the scale of an acoustic wavelength similar to that in optics. J.C. Bamber[76] proposed that the simultaneous arrival or integration of signals can be as a result of multiple scattering, high side lobe levels or due to inhomogeneous propagation medium which distorts the phase of the received waveform across the receiving aperture. In ultrasound imaging, a three-dimensional (3D) space called the resolution cell is defined wherein the pressure amplitude of sound has non-zero values. If there exists only a single scatterer within this resolution cell, resolving it is not an issue. If on the other hand, there are multiple scatterers within a single resolution cell, the wavelets scattered will interfere resulting in the blurring speckle artifact. This effect

is illustrated in the Figure 1-6. Since ultrasound speckle arises as a result of fluctuations in ensemble scattering geometry, small changes in position within a patient results in marked shifts in the speckle patterns. On most recent scanning equipment, an average of the most recently captured sequences of ultrasound scans results in speckle reduction. This technique of averaging is called compounding. In frequency compounding, images collected at different frequencies are averaged whereas, in spatial compounding, images at different spatial locations are averaged. The speckle pattern in an image does not have a direct mapping to echo producing targets within a patient. On the contrary, radiologists learn to interpret images from their vast experience using scanners, since individual scanners produce different speckle patterns for different tissues. Future ultrasound scanners might provide simultaneous display of conventional and speckle-reduced images to aid the radiologist as well as computer-based quantitative texture analysis.

Figure 8: Obstetric image of my spouse displaying the embryonic sac with the familiar speckle artifact at tissue boundaries

Burckhardt[28] described the phenomenon of speckle formation as a 2D random walk problem due to the random phase distribution of scatterers within the resolution cells. Analogous to laser speckle theory, the first order amplitude statistics of acoustic speckle and the signal-to-noise ratio (SNR) are related as the ratio of the mean to standard deviation of the speckle amplitude. Abbott and Thurstone[77] provided additional

analysis that affect speckle formation to be complex intervening media, multiple reflections and "other" factors.

V. IMAGE QUALITY CRITERIA

5.1 Lateral and Axial Resolution

The resolution in an ultrasound image is proportional to the wavelength and is inversely proportional to the frequency. Therefore in order to achieve good resolution, the operational frequency should be as high as possible. Unfortunately, attenuation of ultrasound increases with frequency. The length of the transmitted pulse τ_p determines the range resolution in an A-scan system. τ_p is inversely proportional to the transducer bandwidth BW and the range resolution is given by,

$$\Delta r = \frac{c\tau_p}{2} = \frac{c}{2(BW)} \tag{2.8}$$

An imaging system is often characterized by the ability to depict a point scatterer using the resolution cell. Scanning a point target in water results in the generation of a smeared image. The image of the point target is called the point spread function (PSF) of the imaging system and defines the spatial resolution limit of the system. The resolution along the direction of the beam is called the axial resolution and is determined by the transmitted pulse length and the receiver bandwidth. The resolution transverse to the beam is called its lateral resolution and is determined by the beam width. The lateral

resolution, contrast resolution and spatial uniformity are mainly a function of the transducer size, shape, center frequency and diffraction due to beam propagation. If two point targets are very close to one another, they will be difficult to differentiate since the backscattered RF signals will interfere upon reception.

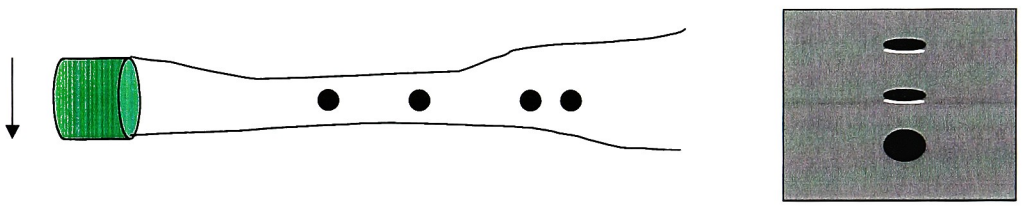

Figure 9: Differentiation of targets on-axis

In Figure 10, there are four point targets that are being scanned by the transducer. The resolution on-axis which is along the direction of the beam results in detecting the first two targets but not the third and forth targets.

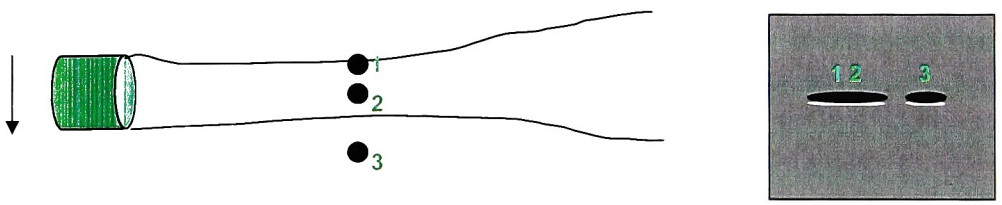

Figure 10: Differentiation of targets off-axis

In Figure 11, there are three point targets located lateral to the transducer face. Since the lateral resolution is determined by the beamwidth, targets 1 and 2 do not get differentiated.

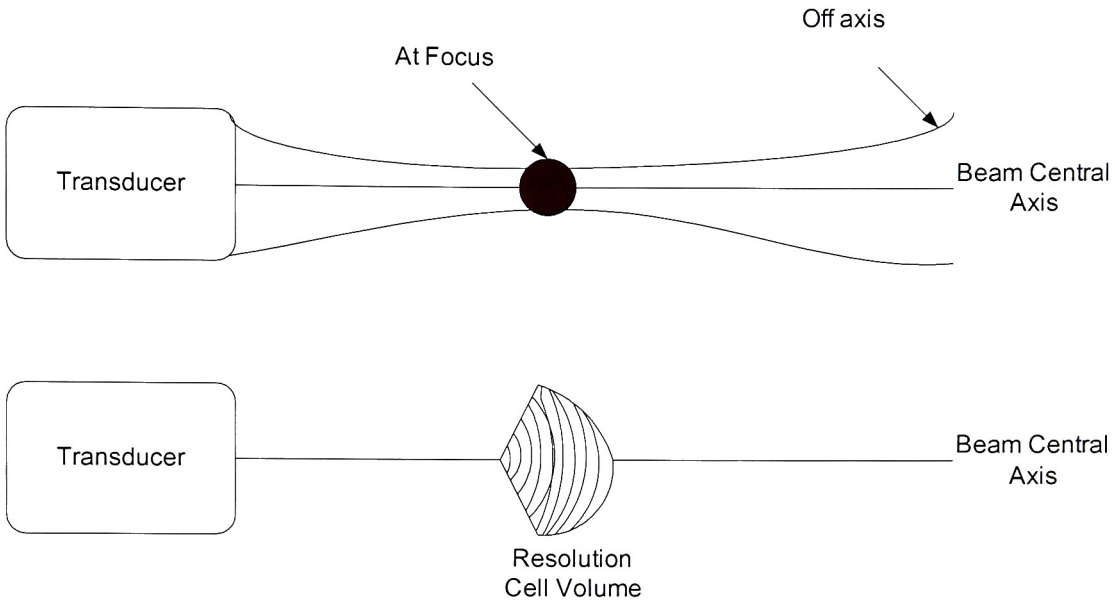

Figure 11: Beam geometry, pulse length and resolution cell volume

In Figure 12, the axial and lateral resolutions are directly visible in the image. The elevational resolution is orthogonal to the image plane. The resolution cell is defined by a border that has a given level relative to the maximum envelope response from a specific depth. The maximum response varies, and the resolution cell changes shape, as a function of depth. An illustration of this 3-D measure is given in Figure 11. The length of the pulse emitted from the transducer determines the axial resolution. The lateral resolution is determined by the pulse width.

Resolution is of great importance to the image quality of ultrasound images, because it defines the ability of the imaging system to resolve details. The spatial

variation of the speckle is approximately determined by the wavelength and becomes finer grained with increasing frequency.

The image quality of an ultrasound imaging system can be described by its spatial and contrast resolution. It depends greatly on the sidelobes generated around the main lobe of an input pulse, since backscattered signals from various directions will combine resulting in interference patterns. Inherent inhomogenities in tissue characteristics will result in spatial variations causing geometric distortion and wavefront aberrations.

Contrast Resolution

Contrast resolution is defined as the minimum difference in amplitudes of two signals in order to get detected, for e.g., an edge. It is used to characterize the spatial extent of the sidelobes in the PSF or the lateral and axial profiles on a logarithmic scale plot. If the sidelobes in the transducer beam profile are large, an off centered scatterer will be imaged at an incorrect lateral location. The lateral distance where the first sidelobes reach 50dB may be used to characterize contrast resolution.

Temporal Resolution

Temporal resolution is limited by the imaging system's frame rate. 2D B-scan images are generated by arranging 1D A-scan lines in rectangular or sector format. The maximum frame rate (or the temporal resolution) depends on the depth of penetration and

the speed of ultrasound. In order to visualize rapidly moving parts of the human body, temporal frame rates of 15-30/secs. are possible using real-time scanners.

Spatial Uniformity

The shape and size of the PSF varies with depth. As depth is increased, the size of the PSF is enlarged since the lateral resolution gets worse with depth. Lateral resolution can be improved by providing fixed focusing at the focal zone, but deteriorates at increased distance due to beam divergence. Optimal resolution is not possible at all depths and the system depicts a spatially variant PSF due to spatial nonuniformity. Beam forming and beam steering techniques could be used to focus the beam dynamically at various depths.

Chapter 3

A PULSE COMPRESSION PRIMER

Pulse compression techniques have been used widely in radar, sonar, geophysical exploration and nondestructive (NDE) testing mainly to overcome peak intensity limitations. This technique has been adopted in medical ultrasound imaging field in order to solve similar problems. The concept derived for radar are frequently applied to the ultrasonic case ignoring major differences such as the assumption of the ideal broadband transmission in the radar case. This assumption is not valid for the ultrasonic case.

There are several reasons that justify careful consideration of this technique in medical ultrasound. Peak intensity limitations in conventional short pulse imaging may arise from two different reasons. Firstly, tissue as a medium responds nonlinearly when excited to very high intensity pressure waves. The input pulse is distorted and becomes rich in higher harmonics as it propagates through the medium. The degree of pulse distortion depends on the source intensity, the distance that the wave has propagated, the frequency and the nonlinear parameter of the medium. In most clinical applications, the tissue through which the sound passes attenuates high frequency selectively and inhibits pulse distortion and shock formation even at high source intensities. An important case is the clinically common case in which a fetus is examined through a nonabsorbing acoustic window formed by the full bladder and/or amniotic fluid. Here, in contrast with the case

in which the entire path is solid tissue, higher harmonics are generated in the fluid may be absorbed in the fetal tissue. Temporal peak pressures in some modern ultrasound instruments approach such levels where finite amplitude waveform distortions have been observed in aqueous media. This is undesirable from the view point of safety and image quality. Secondly, under most favorable conditions, the probability for possible bioeffects caused by acoustic cavitation is significantly greater above certain threshold peak pressure levels. These thresholds range from 0.4Mpa to 1.0 Mpa for frequencies ranging from 1 to 7 MHz. These two potential risk factors are mentioned here only to indicate their relationship to peak pulse pressures. Their implication to in-vivo human exposure is a very complex issue and is a subject of active investigation and critical discussion. Let us start by reviewing linear frequency modulated (FM) signals and its properties.

I. HISTORICAL BACKGROUND

During World War II, intensive research and development was performed in the field of radar to improve the range resolution of targets. The problem was twofold. The prevailing technology at that time did not allow for operation of transmitter components at such high peak power requirements without sparking of the magnetrons. Several researchers resolved this problem but their results were available only after the war due to security reasons. The pioneering article on early history of pulse compression radar has been captured in [20]. In principle, a radio object-locating system includes a transmitter

providing short duration high carrier frequency exploratory pulses of radiant energy. Pulse compression allows radar to utilize a long pulse to achieve large radiated energy, but simultaneously to obtain the range resolution of a short pulse. This is accomplished by frequency or phase modulation to widen the signal bandwidth. Processing the received signal by a matched filter compresses the long pulse to a duration $1/B$, where B is the modulated-pulse spectral bandwidth.

Several patents were published that addressed the dilemma above [43 - 52]. The initial concept of linear frequency modulated (FM) pulse compression as described by R.H. Dicke in a patent filed in 1945 is shown in Figure 12. Dicke coined the term time-compressing filter from which was born the terms "pulse compressor" and "pulse compression ratio". Depicted in the figure (a) is a transmitted pulse of duration T in which the carrier frequency is linearly swept. A pulse-compression filter with the time delay versus frequency characteristic given in (b) is used to delay one end of the received pulse relative to the other, thus producing at the filter output (d) a narrower pulse of greater peak amplitude.

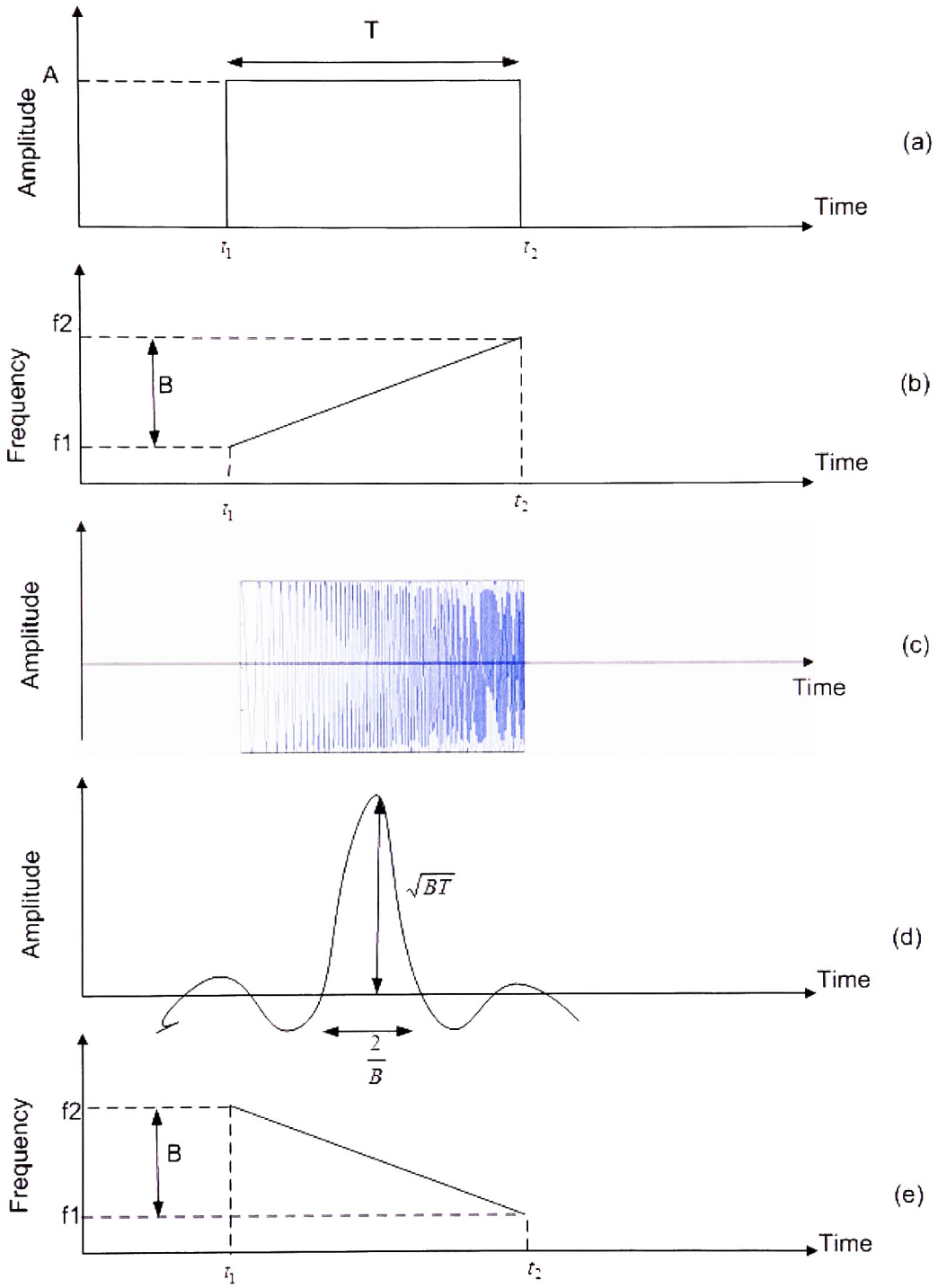

Figure 12: Pulse compression novel idea (redrawn from Dicke's patent)

II. LINEAR FREQUENCY MODULATED (FM) SIGNALS

Carson and Fry [102] defined the linear frequency modulated (FM) signal in 1937 in the field of electric circuit theory. They defined an FM wave as,

$$x(t) = \exp(j\left(2\pi f_0 t + \lambda \int_0^t m(t)dt\right)) \tag{3.1}$$

where λ is a real parameter termed as the "modulation index" and $m(t)$ represents a low-frequency signal to be transmitted with $|m(t)| \leq 1$. The instantaneous angular frequency was defined as,

$$\Omega(t) = 2\pi f_0 + \lambda m(t) \tag{3.2}$$

where $m(t)$ has the dimension of frequency and the instantaneous cyclic frequency as,

$$f_i(t) = f_0 + \frac{\lambda}{2\pi} m(t) \tag{3.3}$$

Van der Pol [103] in 1946 extended this definition of instantaneous frequency to,

$$f_i(t) = \frac{1}{2\pi} \frac{d\Phi(t)}{dt} \tag{3.4}$$

A complex analytic signal $z(t)$ can be defined as,

$$z(t) = x(t) + jy(t) \tag{3.5}$$

which can be expressed as,

$$z(t) = x(t) + jy(t) = A(t)e^{j\phi(t)} \tag{3.6}$$

The envelope of $z(t)$ is given by,

$$A(t) = |x(t) + jy(t)| \tag{3.7}$$

and the phase $\phi(t)$ is given by,

$$\phi(t) = \tan^{-1} \frac{y(t)}{x(t)} \tag{3.8}$$

If a real signal $s(t)$ has a spectrum $S(f)$, then the complex signal $z(t)$ has a spectrum composed of positive frequencies of $S(f)$ only. It is given by the inverse transform of $S(f)$, where the integration goes over only the positive frequencies,

$$z(t) = 2\frac{1}{\sqrt{2\pi}} \int_0^\infty S(f) e^{j2\pi ft} dt \tag{3.9}$$

Note a factor of 2 is inserted so that the real part of the analytic signal will be $s(t)$. Lets define $z(t)$ in terms of the real signal $s(t)$. Now,

$$S(f) = \frac{1}{\sqrt{2\pi}} \int_{-\infty}^\infty s(t) e^{-j2\pi ft} dt \tag{3.10}$$

Substituting in eq. 3.9, we get,

$$z(t) = 2\frac{1}{2\pi} \int_0^\infty \int s(t') e^{-j2\pi ft'} e^{j2\pi ft} dt' df \tag{3.11}$$

$$= \frac{1}{\pi} \int_0^\infty \int s(t') e^{j2\pi f(t-t')} dt' df \tag{3.12}$$

Using the inequality,

$$\int e^{j2\pi fx} df = \pi\delta(x) + \frac{j}{x} \tag{3.13}$$

Substituting we get,

$$z(t) = \frac{1}{\pi} \int s(t') \left[\pi\delta(t-t') + \frac{j}{t-t'} \right] dt' \tag{3.14}$$

Solving we get,

$$A[s] = z(t) = s(t) + \frac{j}{\pi} \int \frac{s(t')}{t-t'} dt' \tag{3.15}$$

Gabor proposed a method to generate a unique complex signal from its real counterpart. This second term is the Hilbert transform defined as,

$$H[s(t)] = \frac{1}{\pi} \int \frac{s(t')}{t-t'} dt' \tag{3.16}$$

where the Cauchy principle value of the integral is used.

Frequency modulated pulses $x(t)$ can be described as the product of a rectangular function (envelope) and a modulated sinusoidal signal.

$$x(t) = RECT\left(\frac{2t-T}{T} \right) \cdot \sin\left(2\pi (f_1 t + \frac{1}{2} k t^2) \right) \tag{3.17}$$

with

$$k = \frac{f_2 - f_1}{T} \tag{3.18}$$

The instantaneous frequency $f(t)$ increases linearly with time, beginning at a lower cut-off frequency f_1. The upper cut-off frequency f_2 is reached after the time $t = T$.

$$f(t) = \frac{d}{dt}\left(f_1 t + \frac{1}{2} k t^2 \right) = f_1 + \frac{f_2 - f_1}{T} t \tag{3.19}$$

$$f(t)|_{t=0} = f_1 \tag{3.20}$$

$$f(t)|_{t=T} = f_2 \tag{3.21}$$

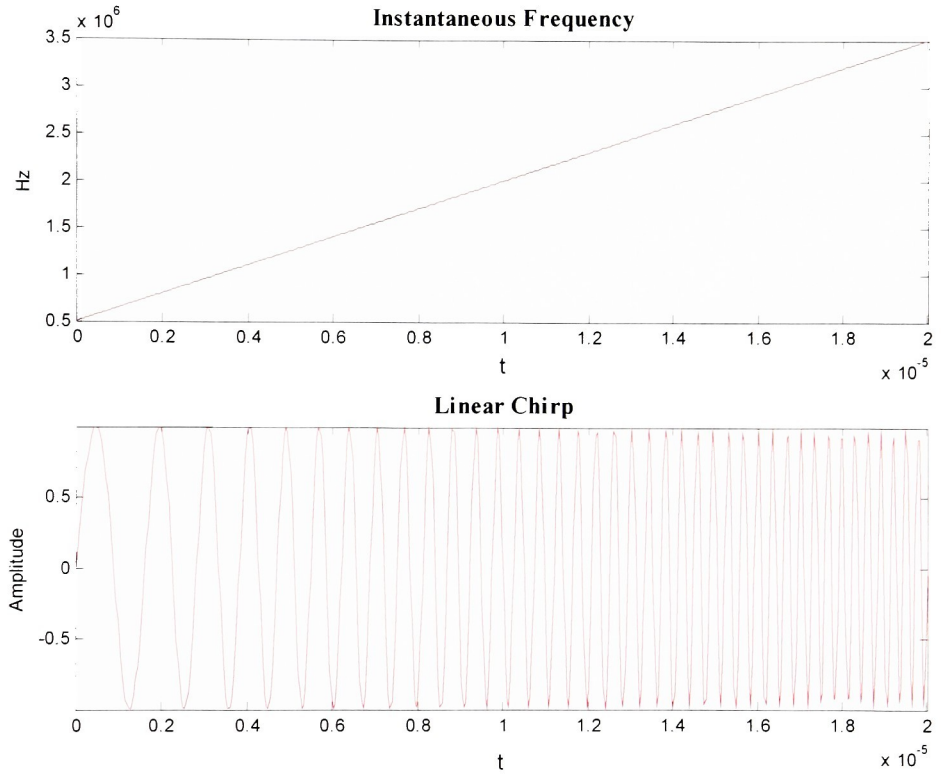

Figure 13: Linear chirp and its instantaneous frequency

III. SPECTRUM OF LINEAR FM SIGNAL

Let us consider a signal $x(t)$ which represents a weighted sum of harmonic vibrations. Given such a signal, a signal analyst would attempt to calculate its exact spectral

decomposition via its Fourier transform (FT). This can be done by using the Fourier transform of the signal defined as:

$$X(f) = \int_{-\infty}^{\infty} x(t) e^{-j2\pi ft} dt \tag{3.23}$$

The values of $X(f)$ characterize entirely the signal $x(t)$ so that it can be reconstructed using the inverse Fourier transform given by,

$$x(t) = \int_{-\infty}^{\infty} X(f) e^{j2\pi ft} df \tag{3.24}$$

The calculation of the spectrum of a linear frequency modulated pulse is described below. To a real signal, there exists a complex analytic signal $x(t)$,

$$x(t) = RECT\left(\frac{2t-T}{T}\right) \cdot e^{j2\pi\left(f_1 t + \frac{1}{2}kt^2\right)} \tag{3.25}$$

that fulfills the condition,

$$x_r(t) = \Re\{x(t)\} \text{ and } X(f) = 0,\ f < 0 \text{ with } X(f) = \Im^{-1}\{x(t)\}$$

Fourier transform of $x(t)$ results in the spectrum $X(f)$:

$$X(f) = \Im^{-1}\{x(t)\} = \int_{-\infty}^{\infty} x(t) \cdot e^{-2\pi ft} dt \tag{3.26}$$

$$= \int_{-\infty}^{\infty} RECT\left(\frac{2t-T}{T}\right) \cdot e^{j2\pi\left((f_1 - f)t + \frac{1}{2}kt^2\right)} dt$$

$$= \int_{0}^{T} e^{j2\pi\left((f_1 - f)t + \frac{1}{2}kt^2\right)} dt = \int_{v_1}^{v_2} c \cdot e^{j\frac{\pi}{2}v^2} dv$$

Using the principle of quadratic extension,

$$a^2 + 2abt + b^2t^2 = (f_1 - f)t + \frac{1}{2}kt^2 \Rightarrow b = \sqrt{\frac{k}{2}} \tag{3.27}$$

$$2ab = (f_1 - f) \Rightarrow a = \frac{(f_1 - f)}{\sqrt{2k}} \tag{3.28}$$

$$\Rightarrow X(f) = \int_0^T e^{\frac{(f_1-f)}{2k} + (f_1-f)t + \frac{1}{2}kt^2} \cdot e^{-j2\pi \frac{(f_1-f)^2}{2k}} dt \tag{3.29}$$

$$= e^{-j2\frac{\pi}{k}(f_1-f)^2} \cdot \int e^{j\frac{\pi}{2}(2\frac{(f_1-f)}{\sqrt{2k}} + \sqrt{2k}t)} dt \tag{3.30}$$

Let us substitute $y = \frac{f_1 - f}{\sqrt{\frac{k}{2}}} + \sqrt{2k}t$ in the above equation. This results in, $\frac{dy}{dt} = \sqrt{2k}$ and

$dt = \frac{1}{\sqrt{2k}} dy$. The limits of the integral become $y_1 = y|_{t=0} = \frac{f_1 - f}{\sqrt{\frac{k}{2}}}$ and

$y_2 = y|_{t=T} = \frac{f_1 - f}{\sqrt{\frac{k}{2}}} + \sqrt{2k}T$.

$$\Rightarrow X(f) = \frac{1}{2\sqrt{k}} \cdot e^{-j\frac{\pi}{k}(f_1-f)^2} \cdot \int_{y_1}^{y_2} e^{j\frac{\pi}{2}y^2} dy \tag{3.31}$$

The spectrum can be formulated using Fresnel-Integrals,

$$C(z) = \int_0^z \cos(\frac{\pi}{2}y^2)dy\ ,\ S(z) = \int_0^z \sin(\frac{\pi}{2}y^2)dy \tag{3.32}$$

$$X(f) = \frac{1}{2}\frac{1}{\sqrt{2k}} \cdot e^{-j\frac{\pi}{k}(f_1-f)^2} \cdot [Z(v_2) - Z(v_1)],\ f > 0 \tag{3.33}$$

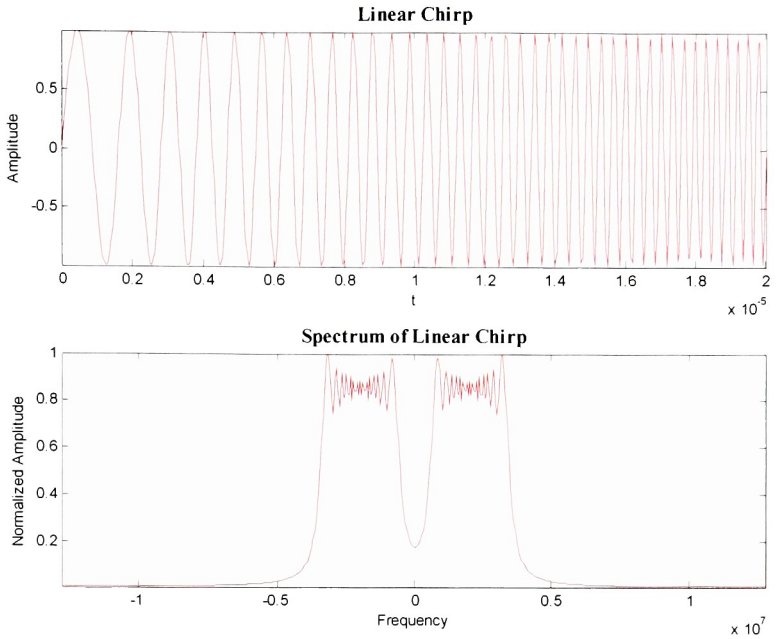

Figure 14: Linear chirp and its frequency spectrum

If the linear frequency modulated signal is directly fed into a compression filter, the gain in the SNR can be calculated to be,

$$SNR = \sqrt{\Delta f \cdot T_0} \tag{3.34}$$

IV. MATCHED FILTER FOR LINEAR FM SIGNAL

Klauder *et al.*[39] has shown the criterion for a matched filter to be,

$$H(f) = F^*(f) \tag{3.35}$$

where $H(f)$ is the transfer function of the filter, $F(f)$ is the spectrum of the input signal and, * denotes complex conjugate. A filter is defined as "matched" to the input signal when its transfer function is equal to the complex conjugate of the signal spectrum. Under these circumstances, the peak signal to rms noise ratio at the output of the filter is maximum.

For the case of a linear FM pulse-compression waveform, the initial signal is,

$$\varepsilon_1(t) = RECT\left(\frac{2t-T}{T}\right)\cdot e^{j2\pi\left(f_1 t+\frac{1}{2}kt^2\right)} \tag{3.36}$$

The matched filter for this signal $\widetilde{Y}_{m_1}(f)$ may be readily obtained from the analysis of the spectrum of $\varepsilon_1(t)$,

$$\widetilde{Y}_{m_1}(f) = \widetilde{\varepsilon}^*(f) \tag{3.37}$$

$$= \frac{1}{2}\frac{1}{\sqrt{2k}}\cdot e^{+j\frac{\pi}{k}(f_1-f)^2}\cdot\left[Z^*(v_2)-Z^*(v_1)\right] \tag{3.38}$$

where *v1* and *v2* are given in equation Eq, 3.33. The matched filter response is obtained by the relation: $Y_m(t) = \varepsilon^*(-t)$. Therefore,

$$Y_m(t) = \varepsilon_1{}^*(-t)$$

$$= RECT\left(\frac{2t-T}{T}\right)\cdot e^{j2\pi\left(f_1 t-\frac{1}{2}kt^2\right)} \tag{3.39}$$

The output response when the rectangular chirp is passed through its own matched filter is computed as,

$$\varepsilon_{m_1}(t) = \int_{-\infty}^{\infty} RECT\left(\frac{\tau - t}{T}\right) RECT\left(\frac{\tau}{T}\right) e^{j2\pi\left[f_1 t + \left(\frac{k}{2}\right)\tau^2 - \left(\frac{k}{2}\right)(\tau - t)^2\right]} d\tau \tag{3.40}$$

When $0 \le t \le T$,

$$\varepsilon_{m_1}(t) = e^{j2\pi\left(f_1 t - kt^2/2\right)} \int_{t-T/2}^{T/2} e^{j2\pi k\tau t} d\tau \tag{3.41}$$

This resolves to,

$$\varepsilon_{m_1}(t) = \frac{1}{\pi kt} e^{j2\pi f_1 t} \sin\pi(ktT - kt^2) \tag{3.42}$$

The envelope of $\varepsilon_{m_1}(t)$ is an even function of time. For $|t| \le T$, the envelope of the matched filter response is given by,

$$T\frac{\sin\pi\left(\Delta|t| - kt^2\right)}{\pi\Delta|t|} \tag{3.43}$$

V. PULSE COMPRESSION THEORY

Linear frequency modulation is one form of pulse compression technique amongst many others. The coded signal may be represented either in the time domain p(t) or by its Fourier transform P(f). In the time domain, the expanded pulse p(t) can be generated by sweeping the instantaneous frequency linearly within a certain bandwidth. This is equivalent to introducing a phase term in the spectrum that is quadratic in frequency. The received echo signal s(t) is fed to a matched filter, whose frequency response P*(f) is the complex conjugate of the coded pulse spectrum. The output of the matched filter section

is the compressed pulse, which is given by the inverse Fourier transform of the product of the echo signal spectrum S(f) and the matched filter reponse P*(f). This is equivalent to performing a crosscorrelation of s(t) with the transmitted signal p(t):

$$r(t) = s(t) \bullet p(t) = \int_{-\infty}^{\infty} p(t+t')s(t')dt' = \Im^{-1}\left[S(f) \cdot P^*(f)\right] \tag{3.44}$$

where $\bullet$ represents crosscorrelation and $\Im^{-1}$ stands for the inverse Fourier transform. Note that if $S(f) = P(f)$, the pulse compression processing subtracts the quadratic phase exactly giving a bandlimited short pulse. In medical applications, there are several factors that could change the amplitude and phase spectrum of the reflected signal and hence introduce artifacts such as range sidelobes in the compressed pulse. These factors were also discussed in one of the first examples of pulse compression technique applied to medical ultrasound and are considered in detail [51].

The generation of a backscattered signal from a scatterer at a fixed distance in response to an input pulse is assumed to be a linear shift invariant process. $p(t)$ is the input fm pulse and $n(t)$ represents the medium and system impulse response. The backscattered signal $s(t)$ can be expressed as a convolution of $p(t)$ with $n(t)$:

$$s(t) = p(t) * n(t) \tag{3.45}$$

After pulse compression,

$$r(t) = s(t) \bullet p(t) = \left[p(t) * n(t)\right] \bullet p(t) \tag{3.46}$$

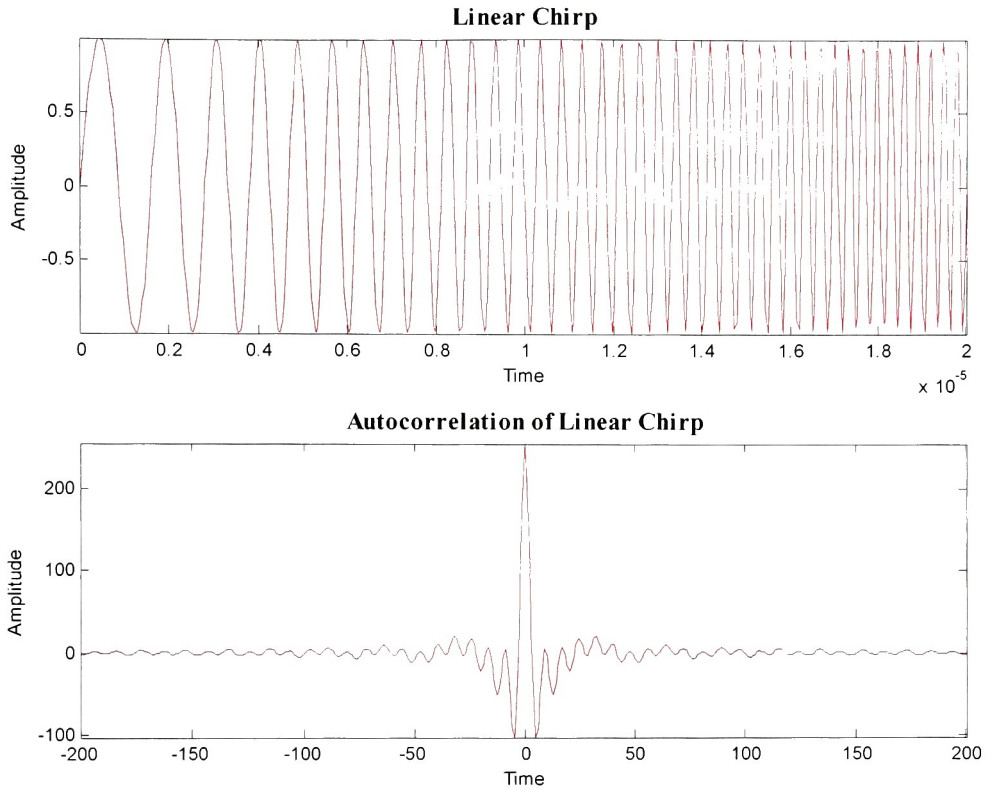

Figure 15: Linear chirp and its autocorrelation

If a scatterer is located in a nonattenuating medium along the transducer's central axis, and in the far field, then $n(t) = A \cdot \delta(t - t_i)$, where A is the reflection coefficient and t_i is the two-way travel time. Here the compressed pulse is simply the autocorrelation of the input fm pulse $p(t)$ and closely approximates a normal short pulse used in conventional imaging under similar bandwidth conditions.

$$n(t) = \left[A_1\delta(t - t_1) + A_2\delta(t - t_2) + ...\right] = \sum_{i=1}^{N} A_i\delta(t - t_i) \tag{3.47}$$

Hence using the commutative property,

$$r(t) = \sum_{i=1}^{N} A_i \left[p(t) * \delta(t - t_i) \right] \bullet p(t) = \sum_{i=1}^{N} A_i \left[\delta(t - t_i) * p(t) \right] \bullet p(t) \tag{3.48}$$

$$= \sum_{i=1}^{N} A_i \delta(t - t_i) * \left[p(t) \bullet p(t) \right] \tag{3.49}$$

VI. TIME BANDWIDTH PRODUCT

The peak amplitude of the compressed pulse is larger than the peak amplitude of the input FM pulse by a factor of $\sqrt{K}$. This gain factor K , is the effective time bandwidth product, is an indicator of the achievable signal-to-noise (SNR) ratio improvement. Any waveform with a gain factor greater than unity is referred to as a "pulse compression" waveform. Figure 16 depicts the amplitude spectra of two waveforms with varied time-bandwidth products.

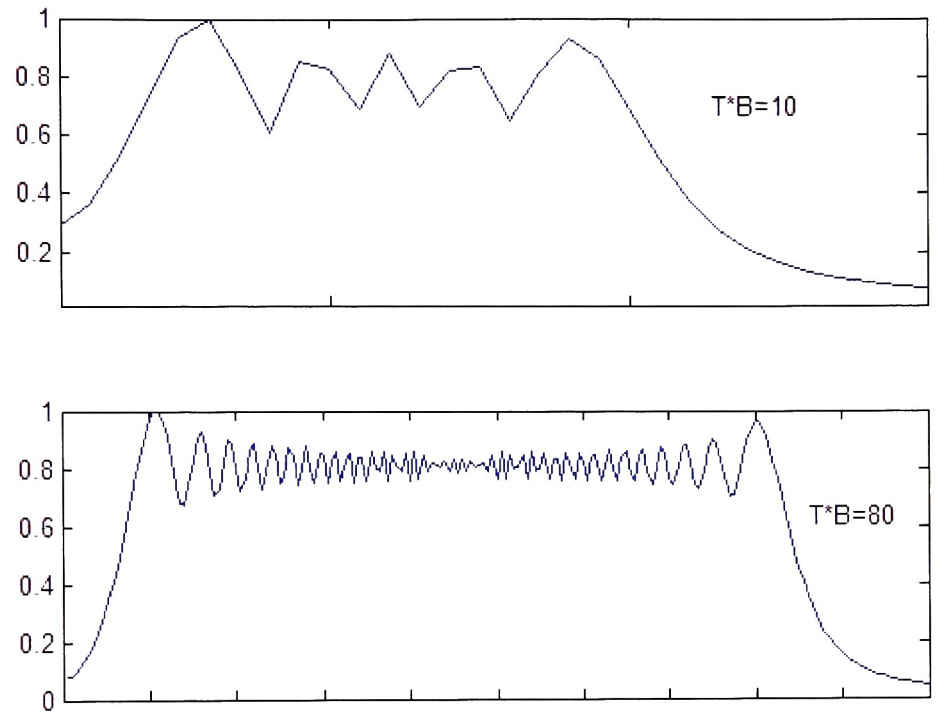

Figure 16: Amplitude spectra for different time-bandwidth products

The "pulse compression ratio" is derived as follows. Consider an input signal $x(t)$ to be input to a "pulse compression" filter with a time duration T defined as,

$$x(t) = RECT\left(\frac{2t-T}{T}\right)\cdot e^{j2\pi\left(f_1 t+\frac{1}{2}kt^2\right)}$$

$$= RECT\left(\frac{2t-T}{T}\right)\cdot e^{j2\pi\left(f_1 t+\frac{1}{2T}(f_2-f_1)t^2\right)} \tag{3.50}$$

The filter transfer function is given by,

$$H(f) = e^{j\frac{T}{2}\frac{(f_1-f)^2}{(f_2-f_1)}} \tag{3.51}$$

The output signal $y(t)$ is the convolution of the input $x(t)$ with impulse response of the filter $h(t)$,

$$y(t) = x(t) * h(t) \tag{3.52}$$

But the impulse response $h(t)$ is the inverse Fourier transform of the filter transfer function $H(f)$,

$$h(t) = \Im^{-1}\{H(f)\}$$

$$\Rightarrow h(t) = \sqrt{j\frac{(f_2 - f_1)}{T}} e^{-j\frac{\pi(f_2-f_1)}{T}t^2} e^{j2\pi f_1 t} \tag{3.53}$$

Thus, the output signal $y(t)$ is given by,

$$\therefore y(t) = x(t) * h(t) = \int_{-\infty}^{\infty} x(\tau) \cdot h(t-\tau) d\tau \tag{3.54}$$

$$= \int_{-\infty}^{\infty} RECT\left(\frac{2\tau - T}{T}\right) \cdot e^{j2\pi\left(f_1\tau + \frac{1}{2T}(f_2-f_1)\tau^2\right)} \sqrt{j\frac{(f_2 - f_1)}{T}} e^{-j\frac{\pi(f_2-f_1)}{T}(t-\tau)^2} e^{j2\pi f_1(t-\tau))} d\tau$$

$$= \sqrt{j\frac{(f_2 - f_1)}{T}} e^{-j2\pi\left(f_1 t - \frac{f_2-f_1}{2T}t^2\right)} \int_{-\infty}^{\infty} RECT\left(\frac{2\tau - T}{T}\right) \cdot e^{j2\pi\left(\frac{f_2-f_1}{T}t\tau\right)} d\tau$$

$$= \sqrt{j\frac{(f_2 - f_1)}{T}} e^{-j2\pi\left(f_1 t - \frac{f_2-f_1}{2T}t^2\right)} \Im\left\{RECT\left(\frac{2\tau - T}{T}\right)\right\} \tag{3.55}$$

Using the Fourier transform pair,

$$\Im\left\{RECT\left(\frac{t}{T}\right)\right\} = 2SINC(2\pi fT) = 2\frac{SIN(2\pi fT)}{2\pi f} \tag{3.56}$$

$$\Rightarrow \Im\left\{RECT\left(\frac{t-\frac{T}{2}}{\frac{T}{2}}\right)\right\} = T \cdot SINC(\pi fT) \cdot e^{j2\pi fT} \tag{3.57}$$

Thus, the output filtered signal can be re-written as,

$$y(t) = \sqrt{j\frac{(f_2 - f_1)}{T}} e^{j2\pi\left(\frac{\pi}{4}+\left(f_1+\frac{f_2-f_1}{2}\right)t-\left(\frac{f_2-f_1}{2T}\right)t^2\right)} \frac{SIN(2\pi fT)}{2\pi f} \tag{3.58}$$

The gain as a result of pulse compression is defined as,

$$\text{Gain, } K = \frac{\text{Peak amplitude of the compressed pulse}}{\text{Peak amplitude of the input FM pulse}} = \left.\frac{y(t)}{x(t)}\right|_{\max}$$

$$\therefore K = \sqrt{(f_2 - f_1)T} = \sqrt{B \cdot T} \tag{3.59}$$

In addition, the pulse duration d of the compressed pulse is given to be,

$$d = \frac{2\pi}{2\pi(f_2 - f_1)} = B^{-1} \tag{3.60}$$

Chapter 4

THEORY BEHIND PULSE COMPRESSION PSF AND INVERSE FILTERING

I. POINT SPREAD FUNCTION

Gaskill[32] and Macovski[2] clearly describe the concept of a 2D Point Spread Function (PSF). The point spread function of a B-scan imaging system is defined as the 2D output function produced as a result of scanning a point object (a 2D delta function).

Consider launching an FM pulse into a medium with a conventional circular disk transducer. Figure 17 shows a simple scanning geometry, where the center of a circular disk transducer moves along the X-axis for scanning, while the face of the transducer remains on the X-Y plane at z=0. We consider a point scatterer at point P with coordinates $(x_0, 0, z_0)$. The propagation medium is assumed to be homogenous but possesses properties similar to that of typical soft tissue. In particular, we assume a speed of sound c = 1540 m/s and the attenuation in the medium represented by $e^{-\alpha_0 f z_0}$, with α_0 being the slope of the attenuation coefficient in the range 0.3 to 0.5 dB/cm/MHz. Note that this attenuation transfer function modifies only the amplitude spectrum of the pulse and does not affect the phase (apart from a linear phase shift due to time delay). In other words, we are assuming negligible dispersion in soft tissue.

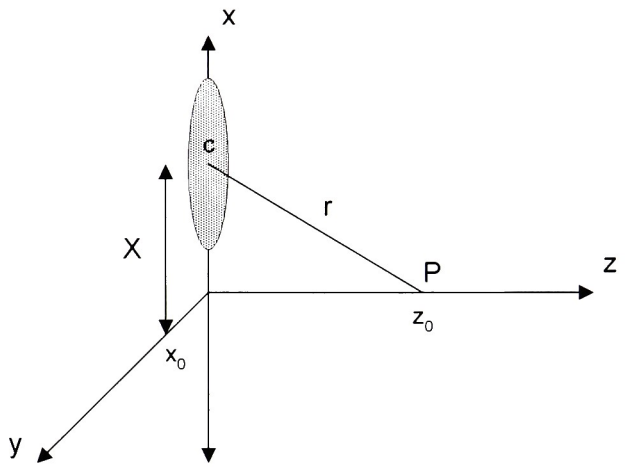

Figure 17: B-scan image formation of point object P by scanning in the X direction with a transducer whose aperture function is s(x,y)

The input signal is an FM pulse represented by $p_{in}(t)$. The backscattered FM pulse, received by the transducer at $x = X + x_0$ along the X-axis, can be represented as,

$$p(x, z_0, t) = \rho \frac{\partial P_{in}}{\partial t} * \left[g_t(t) * g_r(t) \right] * \left[h_t(X, z_0, t) * h_r(X, z_0, t) \right] * f_1(t) * h_a(z_0, t, \alpha_0) \tag{4.1}$$

The approach followed here is based on the impulse response method and has been suggested by several authors for short pulses. $g_t(t)$ and $g_r(t)$ correspond to the time domain impulse response of the transducer in the transmit and receive modes. In most cases, they are equal. $h_t(X, z_0, t)$ and $h_r(X, z_0, t)$ are the transmit and receive "transducer aperture impulse response" or "spatial impulse response" functions in a nonattenuating medium. Analytic solutions for these functions have been derived for

various transducer geometries encountered in medical ultrasound. $f_t(t)$ is the impulse response of the scatterer itself and ρ is the density of the medium. $h_a(z_0,t,\alpha_0)$ is the impulse response due to the two-way propagation in the attenuating medium. Assuming an attenuation coefficient that is linear with frequency and negligible dispersion, the attenuation impulse response has been calculated in closed form as:

$$h_a(z_0,t,\alpha_0) = (const)\cdot \frac{\left(\alpha_0 z_0 / \pi\right)}{\left[\left(\alpha_0 z_0 / \pi\right)^2 - \left(t - 2z_0 / c\right)^2\right]} \tag{4.2}$$

The final B-scan point spread function at depth K, after pulse compression processing and envelope detection can be expressed as:

$$PSF(x,z_0,t) = \left| p(x,z_0,t) \bullet p_{in}(t) \right| \tag{4.3}$$

II. POSSIBLE ISSUES WITH PULSE COMPRESSION

Pulse compression processing is performed on the received signal $p(x,z_0,t)$. From the point of view of optimal detection of the signal in additive noise [39], cross-correlation should be performed on the signal in eq. (4.1) with $p(x,z_0,t)$ itself. However, this amounts to adaptive processing and is a very difficult and time consuming process because a set of cross-correlation functions must be used for different X and z_0.

Furthermore, in medical ultrasound imaging, several randomly distributed scatterers with different x_0 and z_0 are present at the same time. It is impossible to optimize all of them simultaneously. An easier approach is to use $p_m(t)$, the FM signal used to drive the transducer, as the autocorrelating signal for all the RF lines of data, as implied by eq. (4.3). This will result in different degree of mismatch for different x and z_0 and could possibly degrade the PSF [91]. One of the major disadvantages using cross-correlation processing is the generation of large range sidelobe structures [39]. The sidelobes in turn will result in reduction in contrast resolution and must be kept 40-50 dB below the correlation peak value [42]. Pulse shaping techniques have been developed to reduce range sidelobes and used in other fields [8, 39]. Although our FM pulse design procedure takes this into account, the mismatch due to the imaging process and its effect on the sidelobe structure has to be evaluated using equation (4.1). The analysis is facilitated by taking the Fourier transform of Eq. (4.1), so that the factors that modify the spectrum of the input signal $P_{in}(f)$ could be studied.

$$P(x, z_0, f) = j\rho 2\pi f \cdot P_{in}(f) \cdot G_t(f) \cdot G_r(f) \cdot H_t(X, z_0, f) \cdot H_r(X, z_0, f) \cdot F_t(f) \cdot H_a(z_0, \alpha_0, f) \tag{4.4}$$

i. The terms G_t and G_t depend on the overall frequency response of the transducer. Some degree of amplitude weighting of the input FM pulse may result due to this, unless we operate well within the bandwidth of the transducer. The outcome can be significant in the range sidelobes after pulse compression for a small cost in effective

axial resolution and time-bandwidth product [39]. In our experiments, we do not depend on the transducer frequency response for amplitude weighting. Instead, we use an amplitude weighted FM pulse to drive the transducer. This pulse design procedure allows us to perform imaging with a pulse bandwidth that is much smaller than the transducer frequency response bandwidth [49, 92] without excessive penalty on the sidelobe levels.

ii. In a medium such as soft tissue, where the attenuation is frequency dependent, significant changes can occur in the reflected FM pulse. This is because the propagation transfer function $H_a(z_0, \alpha_0, f)$ is not a constant over the frequency range of interest. Therefore, the spectrum of the FM reflected pulse from a reflector at some depth z_0 will be different from the spectrum of the input interrogating pulse with which it is to be cross-correlated. This has two major implications. First a reduction in correlation can lead to a reduction in effective time-bandwidth product. This concern was examined by Rao[51] through simulation studies. It was shown that in medical ultrasound, unlike radar, the time-bandwidth product is depth dependent and small bandwidth operation can limit attainment of very large time-bandwidth products. Nevertheless, a time-bandwidth product of the order of 10 to 40 is possible under normal operating conditions. For example, in the current study, a 20 μs FM pulse with an effective bandwidth of 1 MHz is capable of SNR improvement by a factor of 20. Second, it is possible that the cross-correlation mismatch may contribute

to degradation of range sidelobes. We will use the same theoretical framework [51] to examine changes in sidelobe structure due to the $h_a(z_0, t, \alpha_0)$ term.

iii. The PSF (lateral and axial resolution) of a conventional B-scan imaging scheme is generally well understood. It is not obvious whether a PSF that is similar over a wide dynamic range (0 to 60 dB) can be achieved with the proposed FM pulse imaging scheme. This is due to the fact that the transducer diffraction pattern is frequency dependent. In Equation (4.1), the transfer function due to diffraction, $H_t \cdot H_r$ acts as a low-pass filter. Alternatively, the convolution terms $h_t(t) * h_r(t)$ in Eq. (4.1) reduce to a delta function only in the far field $\left(z_0 >> d^2/\lambda\right)$ and the on-axis condition ($X = 0$). Furthermore, for the off-axis case $(X \neq 0)$, H_t and H_r have a nonzero phase spectrum. Thus, both the amplitude and phase spectra of the reflected FM pulse are modified for an off-axis case. It is tempting to argue that this diffraction factor is the same for short and FM pulse imaging schemes and hence should affect the output in a similar fashion. However, the phase spectra of the two interrogating pulses are in general different even if their amplitude spectra are equal, and this may contribute to some subtle differences.

iv. The dispersive nature of the soft tissue can introduce frequency dependent phase distortions in the reflected signal (over and above a linear frequency phase shift due to time delay). This could result in incomplete pulse compression and possible artifacts

[8]. In medical ultrasound, according to our model, such phase distortions may result from the nature of the phase spectrum of the tissue propagation transfer function $H_a(z_0, \alpha_0, f)$. In Rao's simulation work [51] and in this work, zero phase assumption for the propagation transfer function $H_a(z_0, \alpha_0, f)$ has been used [94]. A more realistic model is the minimum phase model, where the phase transfer function is calculated from the amplitude transfer function via the Hilbert transform [93]. It can be argued that the dispersion in the soft tissue is small and, according to the minimum phase model, contributes an additional term to the phase transfer function that is also approximately linear over a small frequency range [93]. A linear phase distortion can only introduce a time shift in the FM pulse and probably no significant degradation of range sidelobes. This issue could be examined by performing simulations using the so-called minimum phase model for propagation in tissue [93]. Although dispersion in soft tissue is believed to be very small and its effect on pulse compression processing may be negligible, this topic needs further theoretical and experimental evaluation.

III. DESIGN OF THE DRIVE SIGNAL

As described by Fowle [32], a rectangular envelope signal is convenient to create and when limited, is distorted less than amplitude modulated signals. Design of long duration, rectangular FM signal resulting in an arbitrary autocorrelation function has been

addressed by Key et al. [95]. In addition, if the rectangular drive signal is designed to sweep a bandwidth much larger than that of the transducer frequency response, then the transducer frequency response could be effectively recovered and compensated. Let us assume that we have a narrowband signal $s(t)$ centered at frequency f_0 with an envelope $u_e(t)$ and a phase modulation $\varphi(t)$. We have,

$$s(t) = u_e(t)\cos[2\pi f_0 t + \varphi(t)] \tag{4.5}$$

Following the method of stationary phase, Fowle[32] and Key[95] have derived,

$$u(t) \cong \sqrt{2\pi}\,\frac{U_m(\lambda)}{\sqrt{|\theta''(\lambda)|}}\,e^{\left[2\pi\lambda t+\theta(\lambda)\pm\frac{\pi}{4}\right]} \tag{4.6}$$

This follows that, the envelope of the signal $u_e(t)$ is given by,

$$u_e(t) = \sqrt{2\pi}\,\frac{U_m(\lambda)}{\sqrt{|\theta''(\lambda)|}} \tag{4.7}$$

and the phase $\varphi(t)$ is given by,

$$\varphi(t) \cong 2\pi\lambda t + \theta(\lambda) \pm \frac{\pi}{4} \tag{4.8}$$

Fowle[32, 73] has proved that,

$$f(t) \cong T^{-1}(t) \tag{4.9}$$

which states that for FM signals of large time-bandwidth product, the group time delay and the instantaneous frequency are approximately inverse functions.

IV. INVERSE FILTERING

Inverse filter (a.k.a. deconvolution filter) has been used in the field of signal and image processing to restore the input signal from transmission errors. Figure 18 depicts a system with a post-filter.

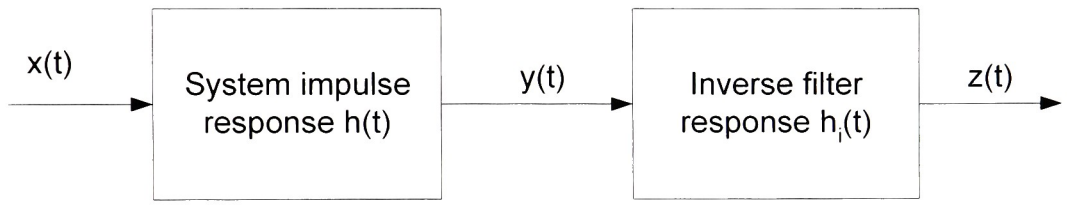

Figure 18: Inverse filter designed to compensate for the system response

The output is related to the input via the convolution property, i.e.,

$$y(t) = x(t) * h(t) \tag{4.10}$$

Taking the Fourier transform on both sides gives,

$$Y(f) = X(f) \cdot H(f) \tag{4.11}$$

$$\Rightarrow X(f) = \frac{Y(f)}{H(f)} = \frac{1}{H(f)} \cdot Y(f) \tag{4.12}$$

Thus, the inverse filter should be designed to be,

$$H_I(f) = \frac{1}{H(f)} \tag{4.13}$$

In the presence of additive noise, a Wiener filter would be more advantageous since it is the combination of a deconvolution filter that has been optimized in a minimum mean-squared sense.

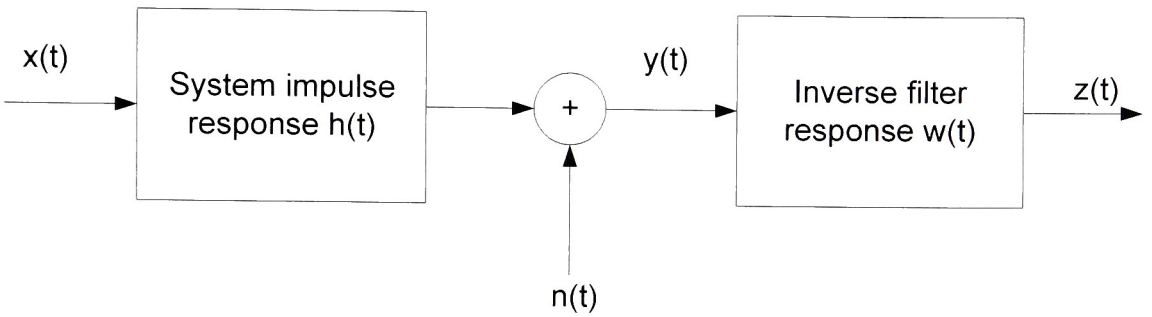

Figure 19: Wiener filter

Here, the output $y(t)$ is given by,

$$y(t) = x(t) * h(t) + n(t) \tag{4.14}$$

$$z(t) = w(t) * y(t) \tag{4.15}$$

Solving in a minimum mean squared sense yields,

$$W(f) = \frac{H_D^* \cdot P_S}{H_D H_D^* \cdot P_S + P_N} = \frac{1}{H_D}\left[\frac{P_S}{P_S + P_N / H_D H_D^*}\right] \tag{4.16}$$

where, P_S is the power spectral density of the signal, P_N is the power spectral density of the noise and H_D is the transfer function of the system. When the second term in the denominator $P_N / H_D H_D^*$ approaches zero, we can approximate,

$$W(f) = \frac{1}{H_D} = H_D^{-1} \tag{4.17}$$

This means when there is no noise or it has little effect on the overall system, the Wiener filter is the same as an inverse filter. When $P_N / H_D H_D^* >> 1$, the noise power is much larger than the signal power, the Wiener filter becomes a matched filter given by,

$$W(f) = \frac{H_D^*}{P_N} = \frac{1}{const} \cdot H_D^* \approx W_M(f) \tag{4.18}$$

Chapter 5

EXPERIMENTAL EVALUATION OF ADAPTIVE DRIVE SIGNAL

This chapter will describe the experimental procedure used to design and generate the input FM drive signal as well as the adaptive drive signal. The resolution of an ultrasound medical imaging system is limited in the lateral direction by the geometry of the sound beam and in the axial direction by the duration of the received echo signals. Researchers frequently perform inverse post filtering of the reflected RF signal to improve image quality. An adaptive technique that derives the pre-enhancement signal in a feedback loop has been developed. This method derives an input signal from the transducer frequency response to inverse modulate the chirp amplitude. The transducer output then becomes an equalized chirp with a wider effective bandwidth. Subsequent pulse compression processing consequently improves the resolution. It has been incorporated into a prototype digital B-Scan imaging system, and the resolution improvement is demonstrated with experiments on clinically relevant phantoms. Although the technique performs inverse filtering, it is operationally different from de-convolution or Wiener optimal inverse filtering, which is normally applied as a post-processing step on the reflected signal. The performance of the latter is generally limited by noise.

I. EXPERIMENTAL SETUP

A prototype ultrasound imaging system was setup to measure and analyze the effect of pulse compression and adaptive drive signal on the transducer frequency response. It consisted of an arbitrary/synthetic waveform generator on Analogic^{TM} model 2020. A series of linear chirp input drive signals were created using Matlab^{TM} and downloaded to the arbitrary waveform generator over the IEEE 488/GPIB bus. The output from the waveform generator was fed into a Ritek RF power amplifier which was used to drive the input to a Panametrics^{TM} immersion type focused ultrasound transducer via a transmit-receive (Tx-Rx) switch. The output of the transmit-receive switch was connected to a pre-amplifier to amplify the reflected RF data. This amplified data was then digitized using a Data Translation DT 6500 series 8-bit digitizer at a sampling frequency of 20 MHz. The external trigger source from the arbitrary waveform generator was used to sync both the digitizer and a CRT oscilloscope. Both channels of the oscilloscope were used to capture and analyze the input FM chirp waveform and the output reflected RF backscattered data prior to serial digitization. A Velmex inc. two motor stepper motor model 86mm-2 was attached to the transducer to provide translation in the X-Y direction. The instructions to control the movement of the stepper motor were downloaded via a serial port attached to a Pentium PC. The arbitrary waveform generator was piggy-backed to the 8-bit digitizer via an IEEE 488/GPIB bus and connected to the Pentium PC

using the same bus architecture. The data from the 8-bit digitizer were downloaded to Matlab for further analysis. Scripts were written in Matlab to generate the input FM chirp waveforms, process RF data to generate the inverse-boosted drive signal used to input to an adaptive second pass as will be described in later sections. Figure 19 depicts the prototype experimental setup used to input, capture and analyze ultrasound data. Figure 20 depicts the block diagram representing the connections and data flow amongst the various devices.

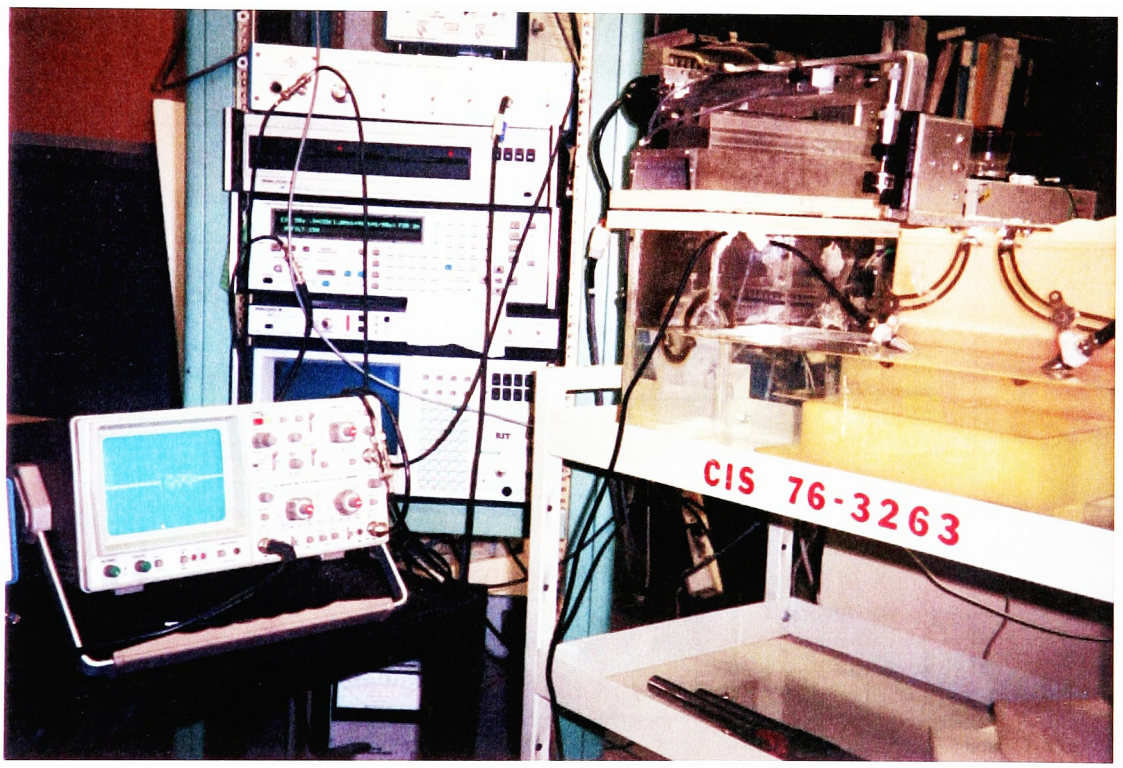

Figure 20: Experimental Prototype Ultrasound Scanning System

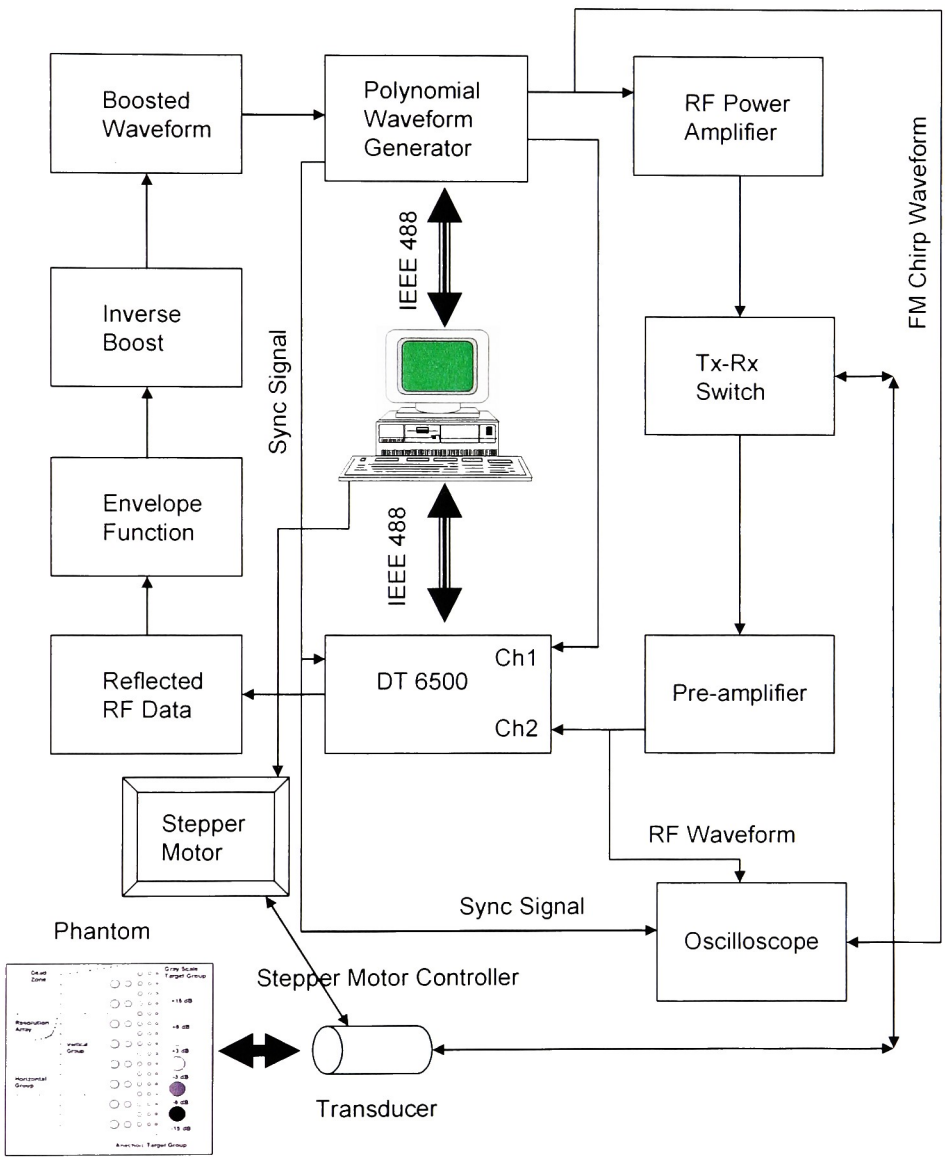

Figure 21: Block diagram of the Prototype Ultrasound Imaging System

Experiments were performed using a focused transducer with a center frequency of 2.25 MHz and a 6 dB bandwidth of 1.2 MHz. A water filled and a tissue-mimicking phantoms were scanned with a wire target at 5cm.

An adaptive technique was designed to create the pre-enhancement inverse-boosted drive signal in a two-step process. During the first step, an input FM linear chirp $p(t)$ was generated at time intervals of $10ns$ using the following equation.

$$p(t) = \sin\left[2\pi\left\{\left(f_0 - \frac{\Delta f}{2}\right)t + \left(\frac{\Delta f}{2T_0}\right)t^2\right\}\right] \tag{5.1}$$

The instantaneous frequency of the uniform amplitude chirp is swept linearly with time, from $(f_0 - \Delta f/2)$ to $(f_0 + \Delta f/2)$ over a time period $T_0 = 20\ \mu$s. In our experiments, we set $f_0 = 2.4$ MHz and $\Delta f = 1.8$ MHz to drive the transducer beyond its 20 dB bandwidth. Pulse shaping technique was used in order to reduce the effect of range sidelobes. A 10^{th}-order Butterworth weighting function $b(t)$ was applied at the beginning and end of the chirp signal to minimize transient response.

$$b(t) = \frac{1}{1 + \left((t - 10\mu)/9\mu\right)^{10}} \tag{5.2}$$

The resultant input drive signal is given by,

$$p'(t) = b(t) \cdot p(t) \tag{5.3}$$

Fig. 22 depicts $p(t)$, $b(t)$ and $p'(t)$.

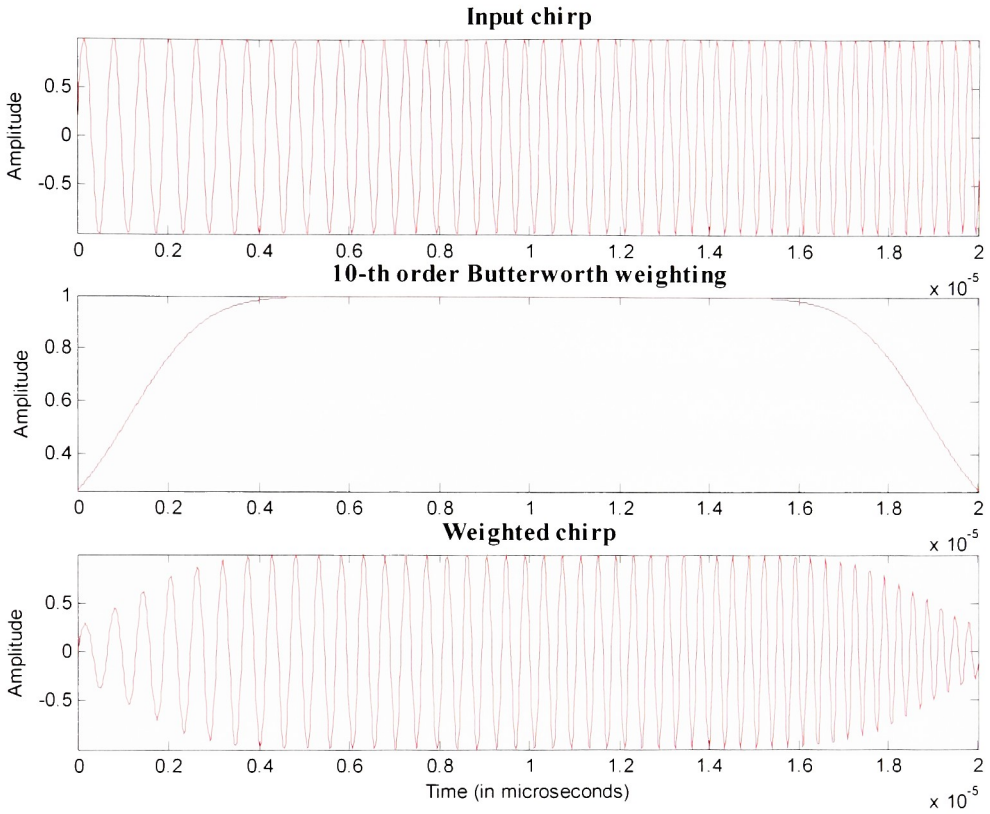

Figure 22: Input FM chirp drive signal, 10-th order Butterworth weighting function and the resultant pulse shaped chirp drive signal

Initially the stepper motor was initialized such that the transducer was located at the point where there was maximum reflection from the wire target. This would be referred to as the "Center line". The input $p'(t)$ was loaded on to the polynomial waveform generator, amplified by the power amplifier and transmitted by the transducer. The reflected RF data was collected, pre-amplified, digitized and stored to a file. In Figure 23, the "Center RF data – Pass 1" depicts the reflected RF waveform collected by the transducer during

the first pass. The RF data was then envelope detected using the Hilbert transform. The envelope of the RF data was inverted and then multiplied with the input FM chirp $p'(t)$. This is called the inverse-boost drive signal which is used as the input to the second pass as depicted in Figure 22. During the first pass, a flat chirp with weighting at its extremities resulted to measure the frequency response of the transducer. This was then inverted and used in the corrected signal created by the inverse-boosted chirp signal. The final output from the second pass is the RF data which appears to be almost flat at all the frequencies under investigation. The RF data from the first pass was cross-correlated with the input drive signal resulting in the creation of a short pulse. Similarly, the RF data from the second pass was cross-correlated with the derived inverse-boosted signal.

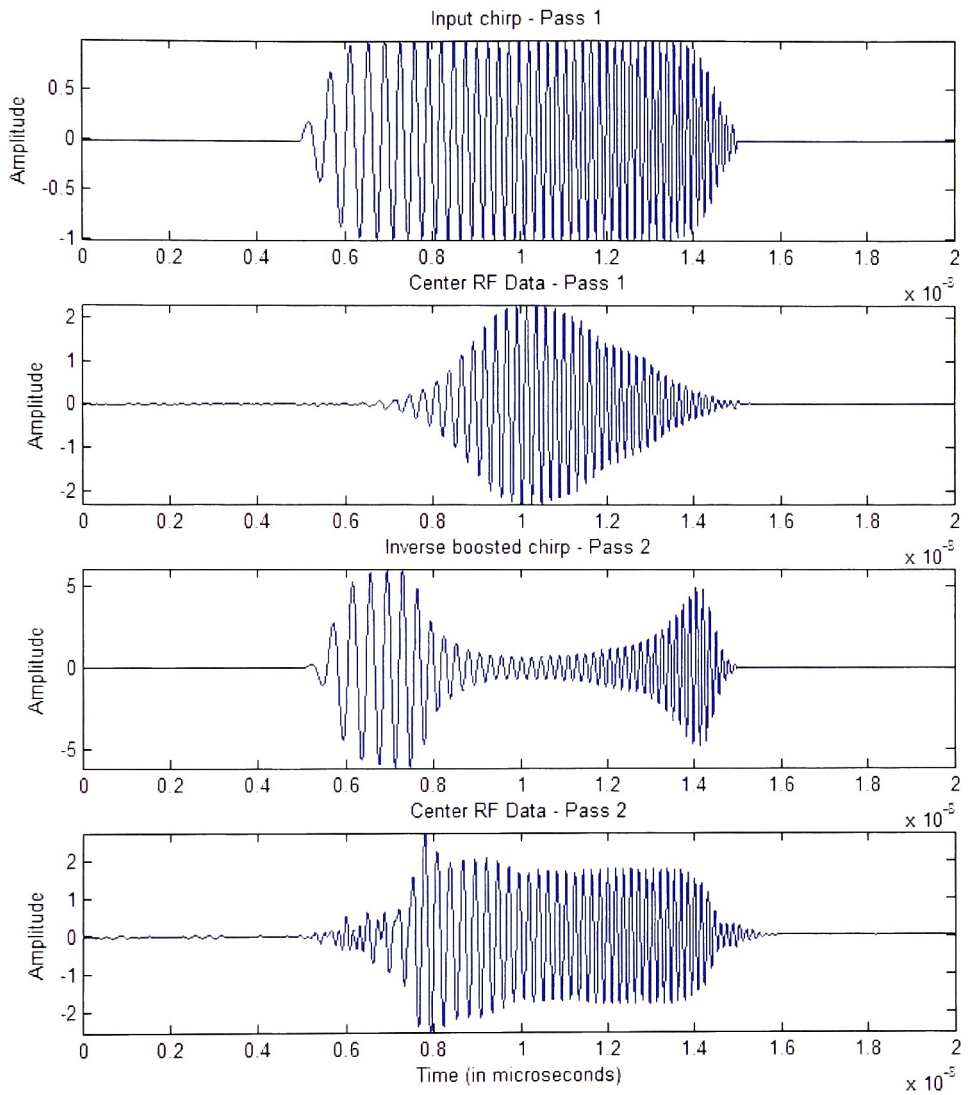

Figure 23: Adaptive drive process in a non-attenuating medium – Input chirp from the first pass, Center RF data from the first pass, Inverse boosted chirp from the second pass, Center RF data from the second pass

The transducer was moved with a stepper motor at 0.15mm interval for 100 lateral positions and the reflected chirp signal was recorded at each location. In Fig. 24 (a - f) the vertical direction represents transducer lateral position and horizontal represents time in μs. Fig. 24(a) is the reflected chirp signal for all lateral positions shown as a gray scale image. The horizontal line through the center represents the reflected chirp when the transducer is right on top of the wire target. The amplitude reduction at low and high frequencies due to the finite bandwidth of the transducer is visible. This signal referred to as $r(t)$ was used adaptively to derive an inverse boost function for the second pass. The signal was first cross-correlated with the constant amplitude input chirp to estimate any residual time shift needed to align it with the input chirp. Envelope detected signal $A(t)$ was obtained from $r(t)$ using the Hilbert transform. The data was downloaded from the digitizer to the PC via the IEEE-488/GPIB interface. The inverse boost envelope function $A^{-1}(t)$ was calculated in software and multiplied by the constant amplitude chirp to produce the new drive signal (inverse amplitude boostedchirp) for the second pass. This function was then uploaded into the waveform generator via IEEE-488 interface. The reflected signal from the second pass is shown in Fig. 24(c). The amplitude boost at the low and high frequencies and amplitude equalization is visible in the 2D image. The pulse compression step is accomplished by cross-correlating every horizontal line of reflected signal with the constant amplitude chirp signal. Finally envelope detection is performed using Hilbert transform on each line and the final 2D

PSF is shown in Fig. 24(b), for the first pass and in Fig. 24(d) after second pass.

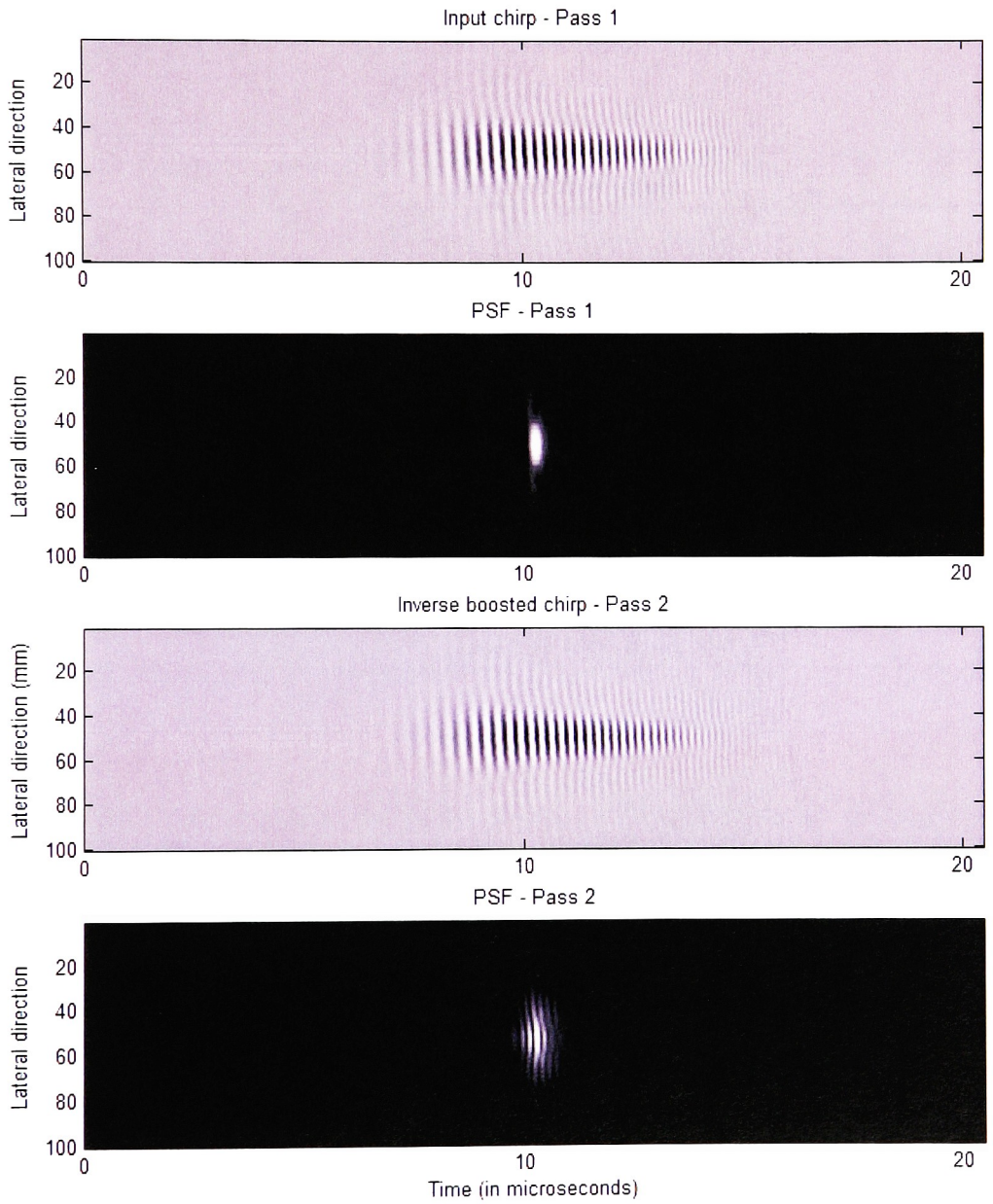

Figure 24: B-scan image of adaptive inverse boost of a wire target scanned in a non-attenuating medium (water)

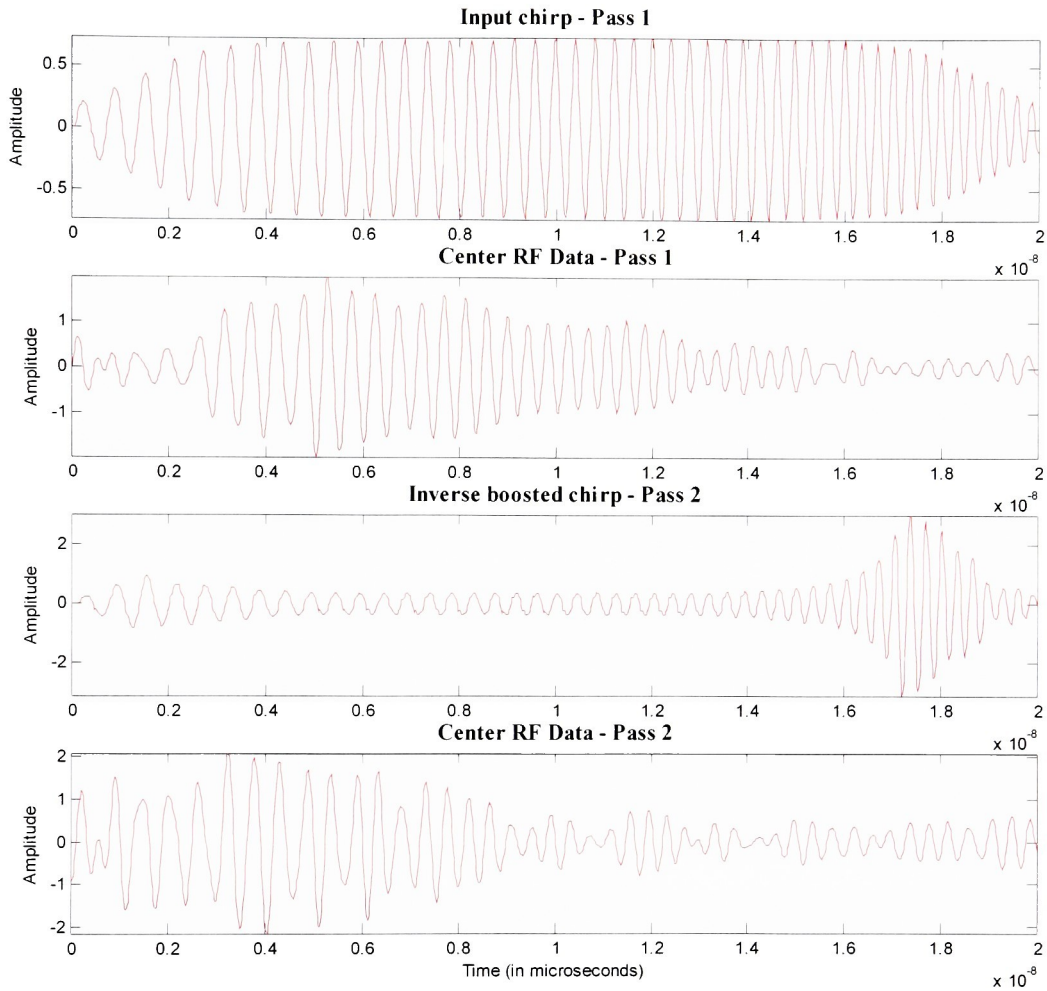

Figure 25: Adaptive drive process in an attenuating medium – Input chirp from the first pass, Center RF data from the first pass, Inverse boosted chirp from the second pass, Center RF data from the second pass

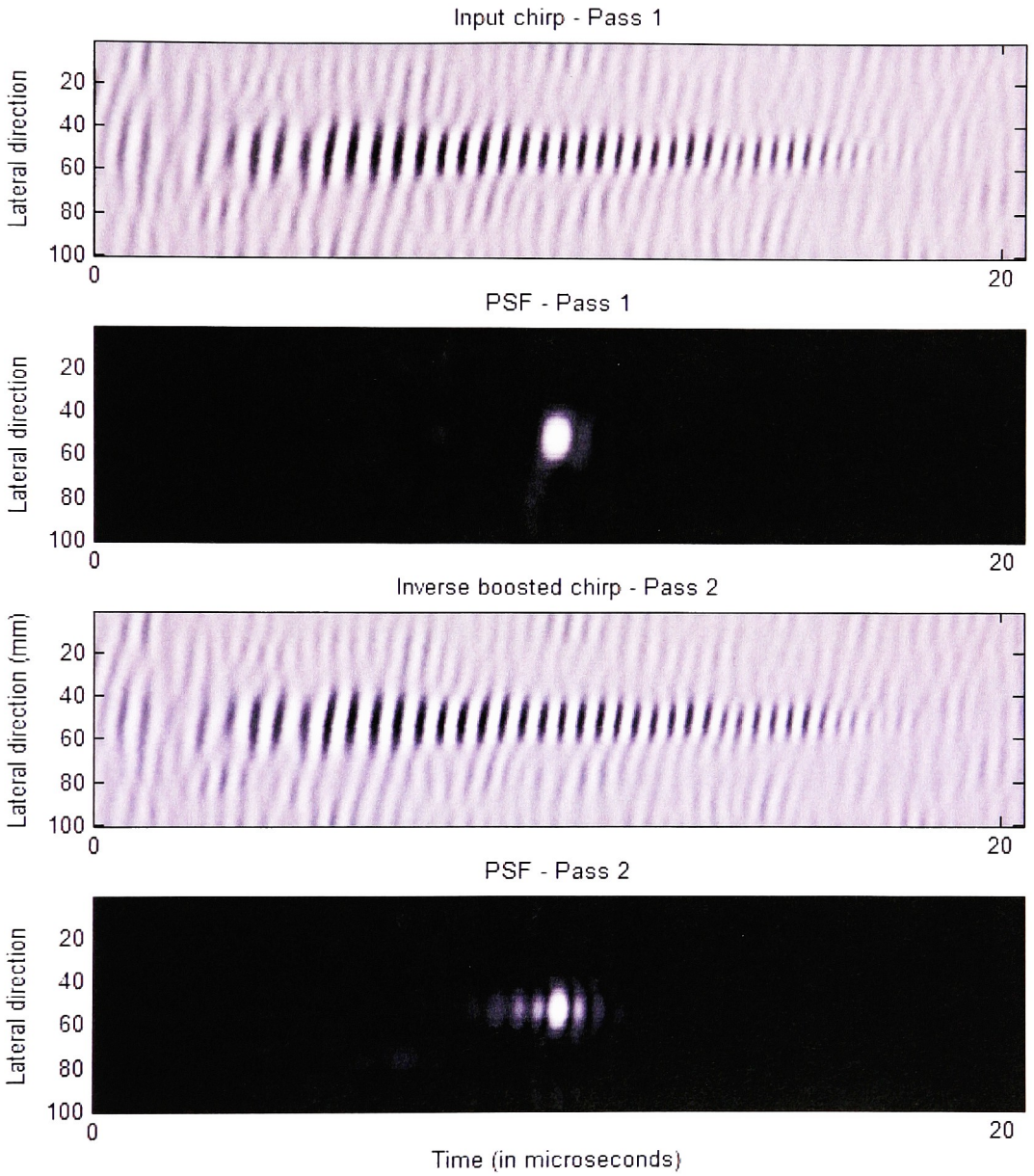

Figure 1: B-scan image using adaptive inverse boost technique of a wire target scanned in an attenuating medium

Similar experiments were performed on a tissue mimicking phantom with attenuation coefficient α_0 = 0.5 dB/cm/MHz. The final PSF is shown in Fig. 25(e) and (f) for first and second pass respectively for the attenuating case.

The 6dB width of the 2D PSF was measured in the axial (horizontal) and lateral (vertical) directions defining the axial and lateral resolution for all the four cases. The axial resolution improved from 1.06μs to 0.82μs (compare Fig. 24(b) and 24(d)) in the non-attenuating case and from 1.016 μs to 0.801μs in the attenuating case. This is a direct consequence of increasing the bandwidth beyond the 6dB bandwidth of the transducer by the inverse boost step. It is important to note that the conventional impulse excitation of the transducer will only produce resolution similar to first pass results. There is a small price to pay in terms of increased sidelobe levels in Fig. 24(d). The lateral resolution was 3.3mm for first and second pass in the non-attenuating medium and 2.25mm in the attenuating medium. For the attenuating case, the same inverse boost function that was adaptively derived for the water phantom was used. Therefore we have inverse filtered only the transducer's frequency response, not that of the attenuating medium. Improvement in lateral resolution here is encouraging but the reason is not obvious.

In summary, we have presented here a prototype experimental ultrasonic imaging system with chirp excitation and a feedback loop to perform adaptive inverse filtering. The outcome is an improvement in the effective bandwidth and hence the resolution and SNR, that is otherwise not possible with conventional impulse driven system. The

technique could potentially be used to inverse filter the frequency dependent attenuation of soft tissue also in addition to the transducer response.

A phantom with embedded cyst-like targets were then scanned using the adaptive inverse boost technique. A noticeable reduction in the speckle size is observed upon comparing the standard short pulse versus the inverse boost FM chirp technique.

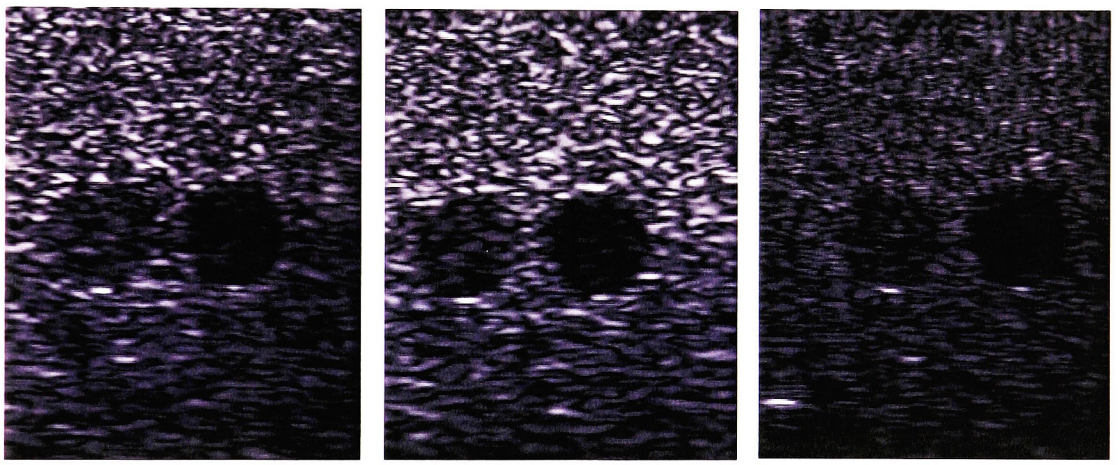

(a) (b) (c)

Figure 27: Specular negative contrast phantom displaying cyst-like targets scanned using (a) Short Pulse drive signal (b) FM Chirp from the first pass (c) Inverse boosted chirp from the second pass

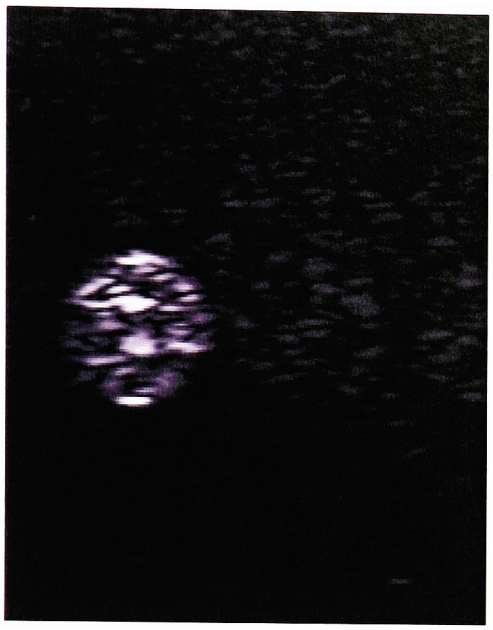

(a)

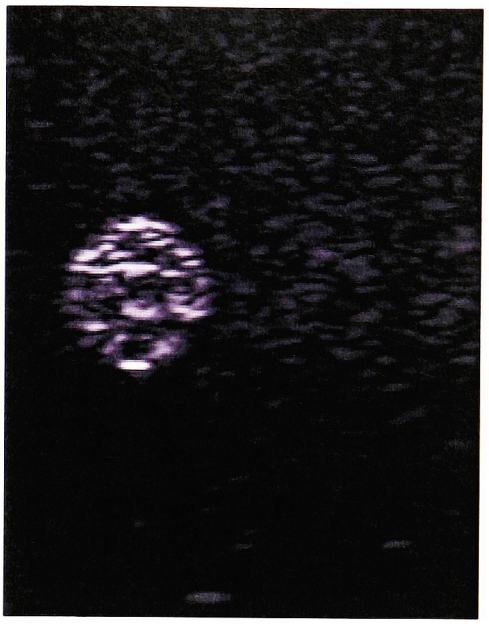

(b)

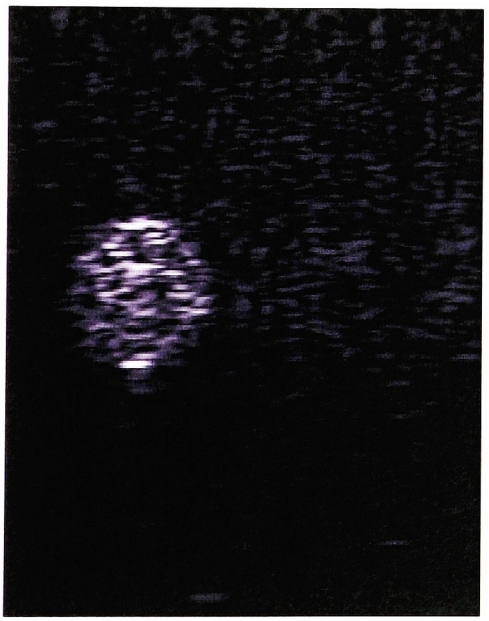

(c)

Figure 28: Speckle positive contrast phantom displaying cyst-like targets scanned using (a) Short Pulse drive signal (b) FM Chirp from the first pass (c) Inverse boosted chirp from the second pass

II. CONCLUSIONS

In summary, we have derived a prototype experimental ultrasonic imaging system with FM pulse excitation and a feedback loop to perform adaptive inverse filtering. The outcome is an improvement in the effective bandwidth and hence the resolution that is otherwise not possible with a conventional impulse-driven system. We have also demonstrated an improvement in the speckle texture pattern. Smaller speckle spot size will help improve the low contrast lesion detectability. The technique could also be used to inverse filter the frequency-dependent attenuation of soft tissue in addition to the transducer response.

Chapter 6

TIME FREQUENCY ANALYSIS CONCEPTS

In this chapter, we develop the basic ideas of time and frequency analysis and clarify the motivation of a joint time-frequency description. "Stationary" signals are those whose statistical properties are independent relative to an absolute time. Extending this, we define non-stationary signals are those whose spectral content and other properties vary with time. Traditional Fourier analysis characterizes stationary signals in either the time domain or frequency domain; joint time-frequency information is simultaneously not available. For non-stationary signals, joint time-frequency analysis becomes a very powerful tool during analysis and synthesis.

I. FOURIER ANALYSIS

In 1822, Jean Baptiste Fourier published his *Theorie analytique de la chaleaur* to prove that any functions of a variable, whether continuous or discontinuous, can be regarded as an infinite superposition of complex exponentials. To this day, Fourier analysis is one of the major advancements in signal processing, physics and mathematics. It is mainly utilized to decompose a signal into individual frequency or spectral components and measure the relative intensity of each component.

Leon Cohen [72] clearly lists the four main reasons to perform spectral analysis. Firstly, spectral analysis provides some information about the characteristics of the source. Secondly, in the study of signals propagating through frequency dependent medium, the signal is decomposed into different frequency bins. Analysis is performed on each frequency component followed by reconstruction of the resulting waveform. Third, decomposing a signal into a series of sinusoids allows for simpler description of the signal. Lastly, it is a powerful mathematical tool for the solution of ordinary and partial differential equations.

A typical Fourier transform pair can be mathematically described as,

$$X(f) = \int_{-\infty}^{\infty} x(t) \bullet e^{-j2\pi ft} dt \tag{6.1}$$

$$x(t) = \int_{-\infty}^{\infty} X(f) \bullet e^{j2\pi ft} df \tag{6.2}$$

It is clear that a Fourier transform identifies all the spectral components that exist in a signal. However, it does not provide any information regarding the time localization of these components.

II. HEISENBERG-GABOR UNCERTAINITY PRINCIPLE

Skolnik [8] has stated that (based on the uncertainity principle) a narrowband signal yields a wide spectrum and a wideband signal yields a narrow spectrum, and both the time signal and frequency spectrum cannot be made arbitrarily small simultaneously.

This type of constraint is imposed on the Fourier transform in that one cannot find a signal that can be concentrated on an arbitrarily small time-frequency region. Flandrin [68] has established the inequality based on a signal *x(t)* with finite energy,

$$E_x = \int_{-\infty}^{\infty} |x(t)|^2 \, dt < +\infty \tag{6.3}$$

It is assumed that the signal and its Fourier transform possess a vanishing center of gravity,

$$\int_{-\infty}^{\infty} t|x(t)|^2 \, dt = 0 = \int_{-\infty}^{\infty} f|X(f)|^2 \, df \tag{6.4}$$

The corresponding moments are defined as,

$$\Delta t^2 = \frac{1}{E_x} \int_{-\infty}^{\infty} t^2 |x(t)|^2 \, dt; \; \Delta f^2 = \frac{1}{E_x} \int_{-\infty}^{\infty} f^2 |X(f)|^2 \, df \tag{6.5}$$

Let us define an auxiliary quantity,

$$I \equiv \int_{-\infty}^{\infty} t x^*(t) \frac{dx}{dt}(t) dt \tag{6.6}$$

Using Parseval's identity and Cauchy-Schwarz inequality,

$$(\mathrm{Re}[I])^2 \le |I|^2 \le \int_{-\infty}^{\infty} t^2 |x(t)|^2 \, dt \cdot \int_{-\infty}^{\infty} \left| \frac{dx}{dt}(t) \right|^2 dt = 4\pi^2 E_x^2 \Delta t^2 \Delta f^2 \tag{6.7}$$

$$\Rightarrow I = \left[t|x(t)|^2 \right]_{-\infty}^{\infty} - E_x - \int_{-\infty}^{\infty} t x(t) \frac{dx^*}{dt}(t) dt = -E_x - I^* \tag{6.8}$$

$$\mathrm{Re}\{I\} = -\frac{E_x}{2} \tag{6.9}$$

Thus the Heisenberg-Gabor uncertainity principle can be expressed by the inequality,

$$\Delta t \cdot \Delta f \geq \frac{1}{4\pi} \tag{6.10}$$

The Gaussian functions are the only kind of signals that minimize the time-bandwidth product in the Heisenberg's sense. These are the only functions whose time and frequency resolution could be improved simultaneously.

III. SHORT TIME FOURIER TRANSFORM

Short-time Fourier transform (STFT) is one of the most widely used technique to study non-stationary signals. In simplest terms, the STFT divides the signal into truncated time segments; Fourier transforms each time segment to calculate the frequencies in that segment and finally depicts the global time-frequency structure as shown in Fig. 29. The original signal $x(t)$ is multiplied by a pre-windowing function $W(t)$, centered at t, to create the modified signal.

$$x_t(\tau) = x(\tau)W(\tau - t) \tag{6.11}$$

STFT was proposed by Gabor in 1942 and has since been extensively used in the fields of speech and signal processing. STFT find vast applications in time-varying filtering of non-stationary signals since their spectral content vary with time. Additionally, STFT is linear and invertible and could be used during the analysis/synthesis phase. The square of the STFT is called the STFT spectrogram to distinguish it from time-varying spectrum

based upon other techniques, such as Gabor expansion and the adaptive representations. The STFT spectrogram could be used to get a rough idea of a signal's energy distribution in the joint time-frequency domain.

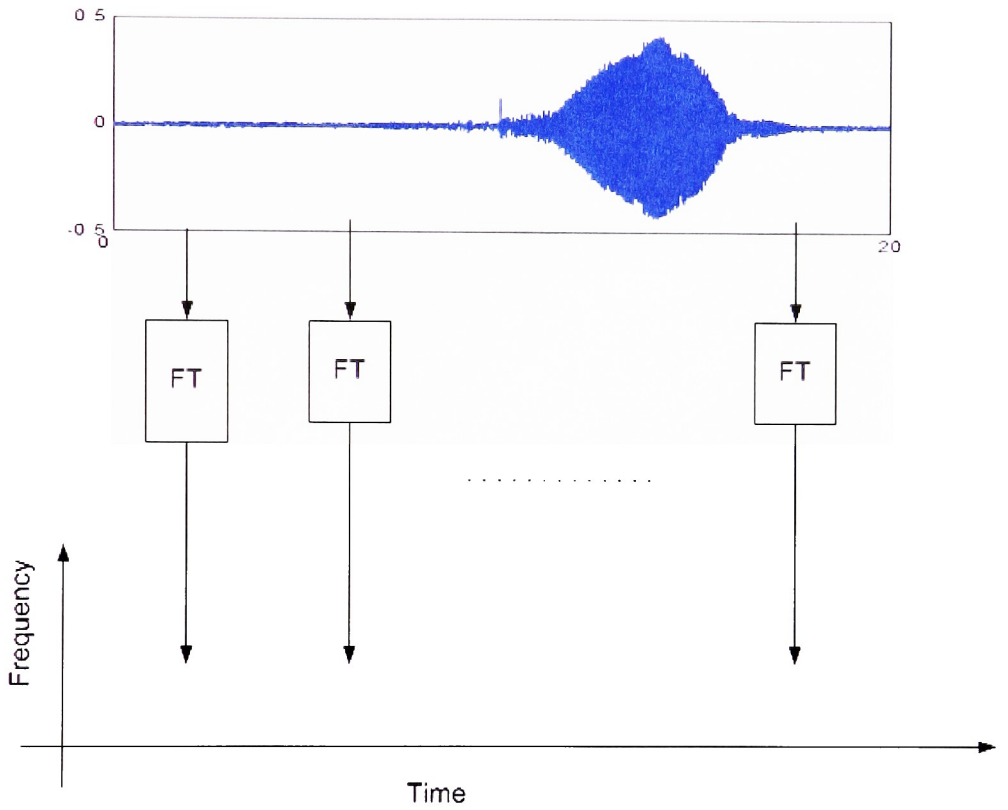

Figure 29: STFT depicted as a series of pre-windowed Fourier Transforms

The short-time spectrum of a signal *x(t)* is defined as,

$$STFT_x^{(\gamma)}(t,f) = \int_{t'}\left[x(t')\gamma^*(t'-t)\right]e^{-j2\pi ft'}dt'$$
$$= e^{-j2\pi ft}\int_{f'}X(f')\Gamma^*(f'-f)e^{j2\pi ft'}df' \qquad (6.12)$$

The energy density spectrum or spectrogram is,

$$P_S(t,f) = \left|STFT_x(t,f)\right|^2 \tag{6.13}$$

The STFT is a linear form of time-frequency representation and is complex-valued. It is significantly influenced by the choice of the analysis window. The time-resolution of the window gets better when the analysis window becomes shorter resulting in degradation of the frequency-resolution. Conversely, analysis by a filter bank with selective filters has a better frequency-resolution with degradation in time-resolution, since the impulse responses of the filter have a longer duration.

Properties of STFT

1. STFT preserves the frequency shifts and time shifts up to a modulation factor:

$$\begin{aligned} y(t) = x(t)e^{2\pi f_0 t} &\Rightarrow F_y(t,f;h) = F_x(t,f-f_0;h) \\ y(t) = x(t-t_0) &\Rightarrow F_y(t,f;h) = F_x(t-t_0,f;h)\cdot e^{2\pi f t_0} \end{aligned} \tag{6.14}$$

2. STFT is reversible.
3. STFT distribution is positive.

Fig. 30 depicts the STFT of a linear chirp signal. As expected, time varies linearly as a function of frequency.

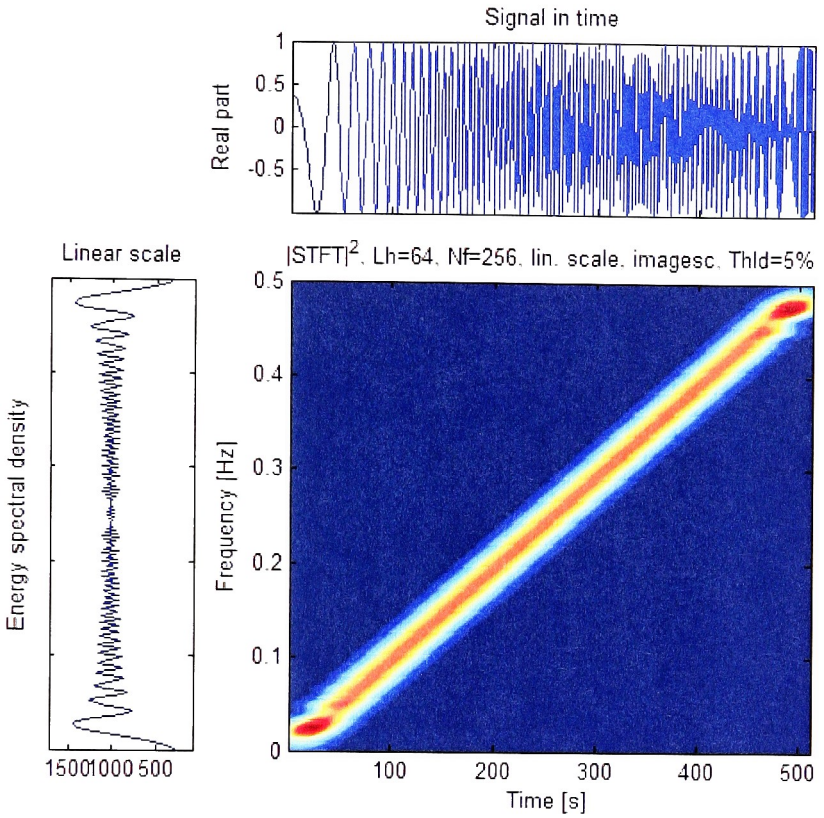

Figure 30: STFT of a linear chirp

IV. WIGNER-VILLET DISTRIBUTION

For a signal $x(t)$, the Wigner-Ville (WV) distribution is given by,

$$WV_x(t,f) = \int_{-\infty}^{\infty} x(t+\frac{\tau}{2})x^*(t-\frac{\tau}{2})e^{-j2\pi f\tau}d\tau \qquad (6.14)$$

The WV distribution is bilinear since the signal appears twice in its calculations. In addition, the signal is supposed to be analytic. WVD has served as a useful tool in the

fields of quantum mechanics, optics, acoustics, bioengineering and image processing. Several researchers have used WVD to analyze time-varying systems and its applications to ultrasound imaging [65, 67, 90].

Properties of WV Distribution:

1. Time-shift invariant

If the WV distribution of a signal is $WV_x(t, f)$, then the WVD of the time shifted version $y(t) = x(t - t_0)$ is the time-shifted WV distribution of $x(t)$.

$$y(t) = x(t - t_0) \Rightarrow WV_y(t, f) = WV_x(t - t_0, f) \tag{6.15}$$

2. Marginal properties

The WV distribution preserves the time and frequency marginal properties of any signal.

$$\int_{-\infty}^{\infty} WV_x(t, f)df = |x(t)|^2 \tag{6.16}$$

$$\int_{-\infty}^{\infty} WV_x(t, f) = |S(f)|^2 \tag{6.17}$$

3. Real Valued

$$WV_x(t, f) \in R \vee t, f \tag{6.18}$$

Fig. 31 depicts the WV transformation of a linear chirp signal. Note the width of the energy distribution is much smaller than that obtained using STFT. This is confirmed by

analytically computing the WV of the chirp equation. This proves that the WV distribution for a chirp localizes to its instantaneous frequency.

$$x(t) = e^{\left\{ j2\pi\left(f_0 t + \frac{k}{2} t^2 \right) \right\}} \Rightarrow WV_x(t, f) = \delta(f - (f_0 + kt)) \tag{6.19}$$

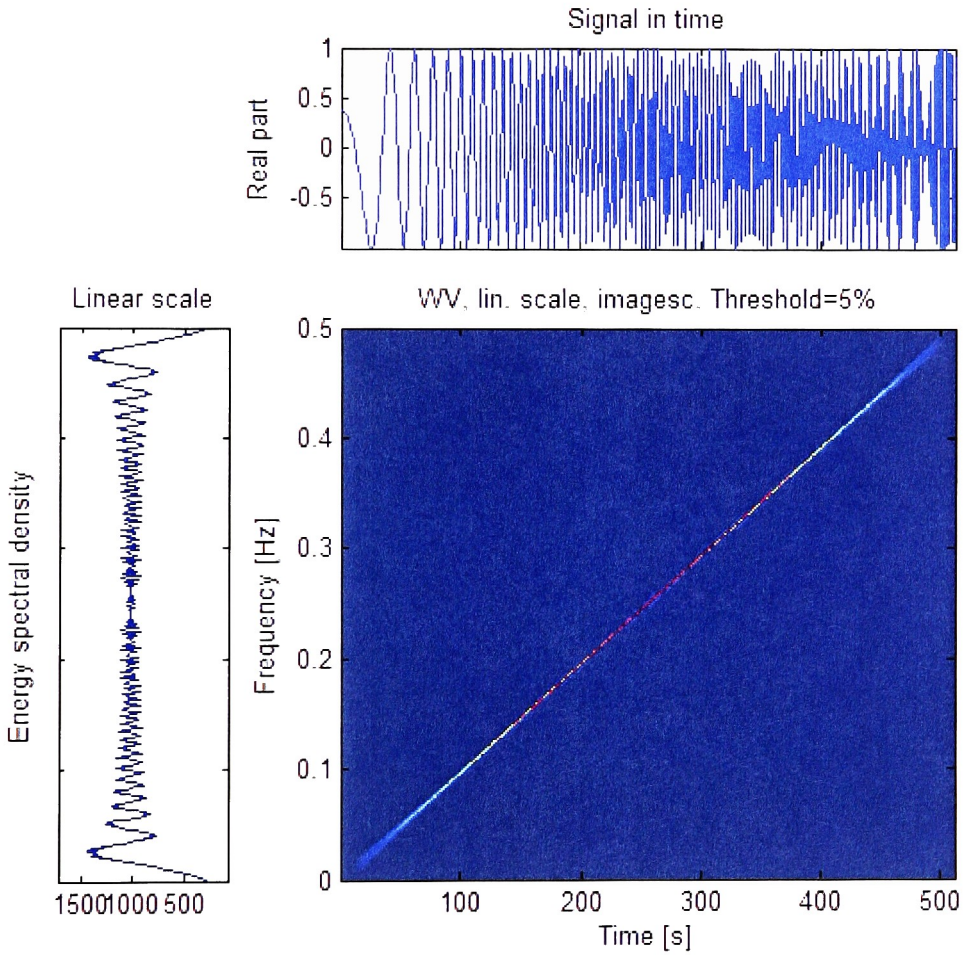

Figure 31: Wigner-Villet transform of a linear chirp signal

Table 1 provides a list of constraints that are verified by both STFT and WV distribution.

CONSTRAINT	STFT	WV
Energy	X	X
Marginal in time		X
Marginal in frequency		X
Reality	X	X
Positivity	X	
Causality		
Invertibility		X
Dilations		X
Convolution		X
Modulation		X
Time support (in the wide sense)		X
Frequency support (in the wide sense)		X
Unitarity		X
Instantaneous frequency		X
Group delay		X

Table 1: A List of Constraints

V. STFT VERSUS WIGNER-VILLET

The spectrogram of STFT as described in Eq.6.13 is defined by,

$$P_S(t,f) = \left| \int_{-\infty}^{\infty} x(\tau) h^*(s-t) e^{-j2\pi fs} ds \right|^2 \tag{6.20}$$

Eq. (6.20) combines a linear operation (Fourier transform) with a quadratic operation (modulus squared). In the case of WV distribution, $WV_x(t,f)$ as defined by Eq. (6.14) uses a quadratic operation applied to the signal followed by a linear (Fourier) transformation. The other major difference is that the WV transform does not require the introduction of an analysis window function, which is external to the signal. The second difference is that the spectrogram is derived from a STFT with an external window/analysis function. The WV distribution is regarded as the same type of analysis with a window which is persistently matched with the signal. Thirdly, in a WV distribution, two points of the plane interfere, so that they create a contribution at a third point, which is the midpoint of a straight line connecting the two.

Chapter 7

EXPERIMENTAL EVALUATION OF CROSS BEAM IMAGING

In B-scan imaging, transmit and receive functions are generally performed by the same transducer. Thus, the time duration of linear frequency modulated (LFM) signals is limited to 10-20 μ s, consequently limiting the time-bandwidth product. With separate transmit and receive transducers in cross-beam geometry, we can overcome this limitation. Now, the image has to be created with a C-scan process as described in Chapter 2. This chapter of the dissertation examines various processing schemes for this modality. The possibility of using time-frequency distributions such as Short-Time Fourier transform (STFT) and Wigner-Villet (WV) transform have been explored. The PSF was experimentally measured and evaluated for different schemes.

I. A COMPUTATIONAL CONSIDERATION

The four techniques used to compare and contrast each other are depicted in Fig. 32 have been analytically described in previous chapters. To generate a 2D image, a C-scan has to be performed by moving two transducers in unison but not change the center of the overlap region. The backscattered signal received by the transducer will be a linear sum of echoes from all scatterers within a cell volume that will be determined by the overlapping beam profiles.

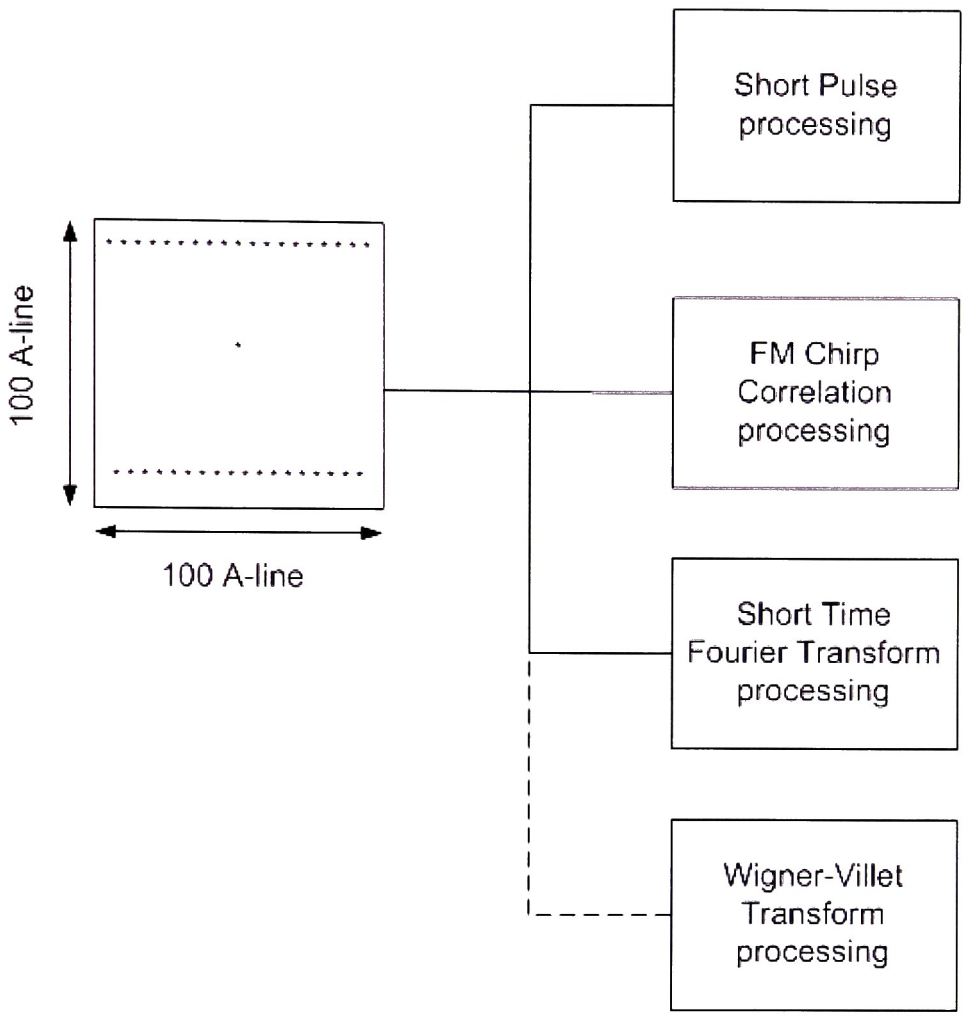

Figure 32: Comparison of four scanning techniques

In Short pulse processing as depicted in Fig. 33, a short pulse drive signal is impinged on the object of study. Each RF A-line is amplitude detected using a Hilbert transform and envelope detected. The maximum value from each envelope detected A-line is captured and stored in an index within a 100x100 array. The maximum of this array provides a

time location which will be used as the time-gate value t_0. At this fixed time-gate t_0, as well as averaged over ten time locations ($\pm 5\Delta t$) around this time gate, the envelope detected values of the 100x100 array are processed resulting in a B-scan PSF image. Thus, the energy at $t = t_0$ is assigned to each pixel in the C-scan image.

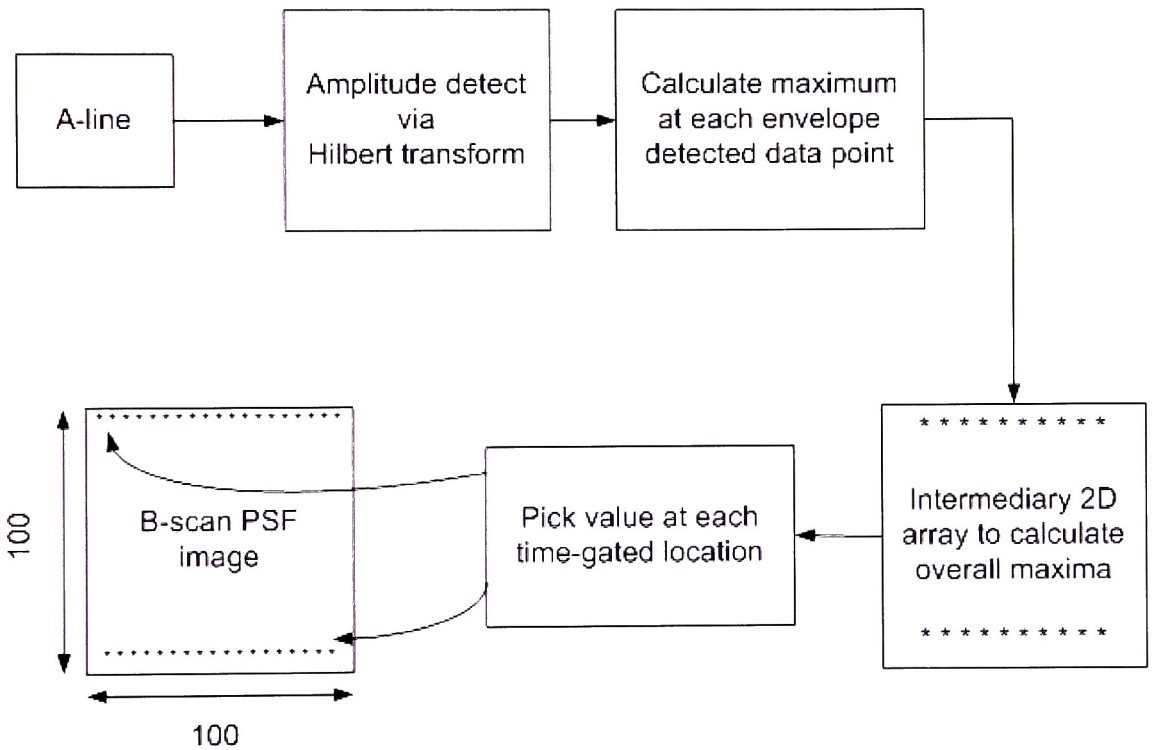

Figure 33: Short Pulse processing steps

FM Chirp processing is similar to short pulse processing except that there is an additional intermediate step as depicted in Fig. 34. This is due to the fact that the advantage of FM chirp processing is in the cross-correlation with the input drive signal. As described in

previous chapters, this results in a SNR improvement equal to the time-bandwidth product of the system.

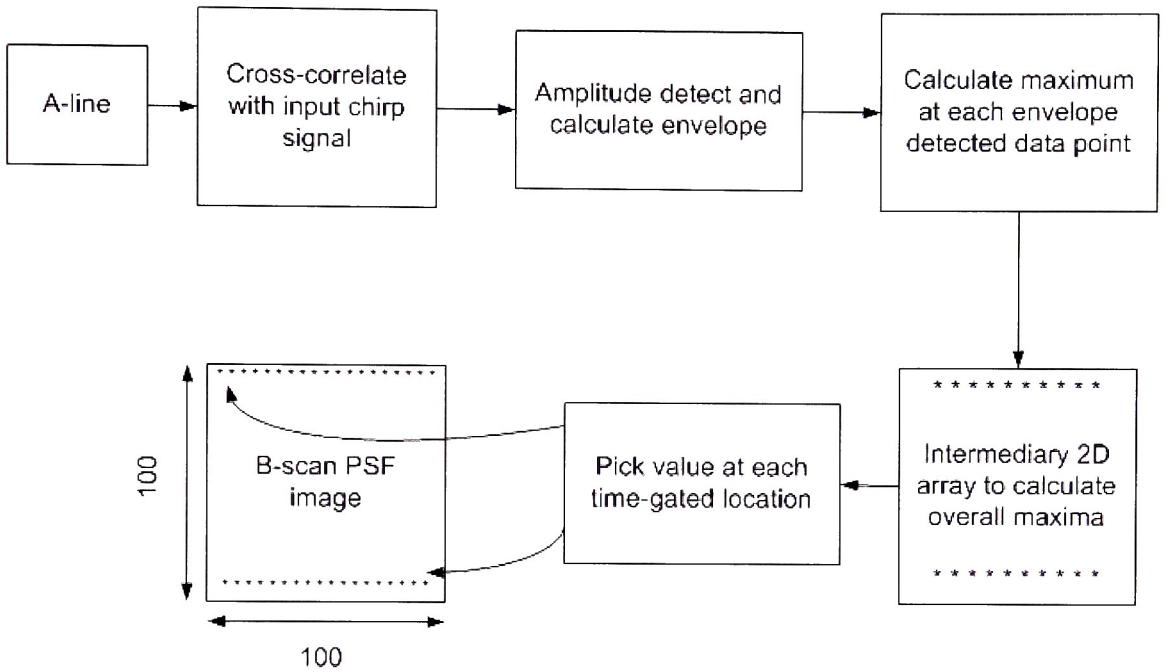

Figure 34: FM cross-correlation processing

As depicted in Fig. 35, each RF A-line is transformed to time-frequency domain. In this transformed domain, a slant window is multiplied to the energy density as shown in Fig, 36. All values within this slant window are retained and others are discarded. Thus the slant window acts as a region-of-interest (ROI) mask. Energy density values within the slant window are summed up for each A-line and is posted as a pixel in the C-scan image. If there are two scatterers in the medium, each scatterer will appear at a unique time gate within this mask unless they are separated by a distance less than the resolution cell volume.

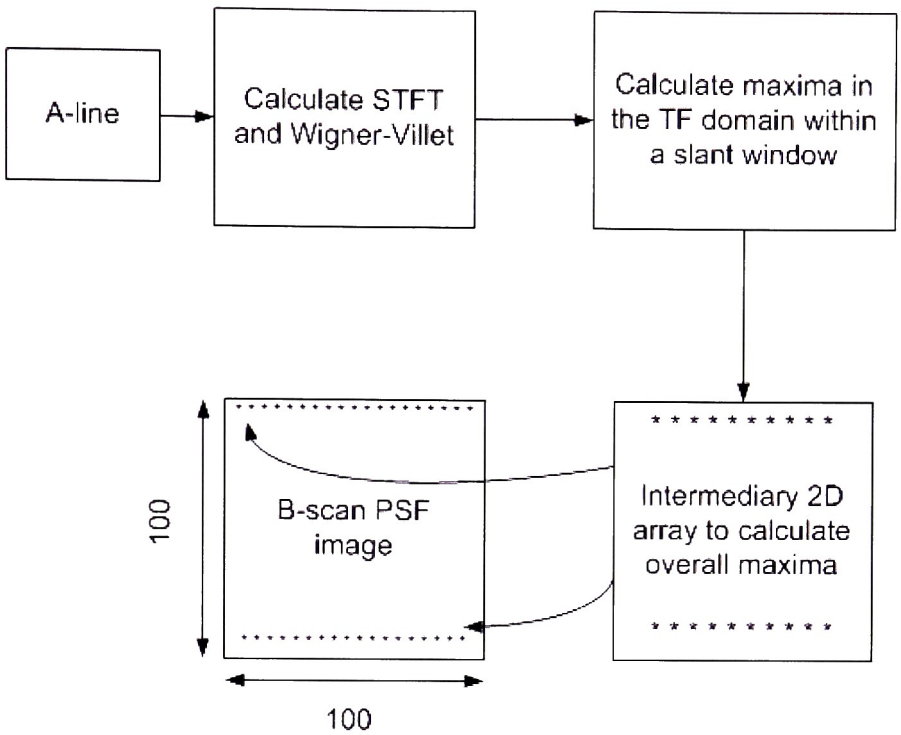

Figure 35: STFT processing

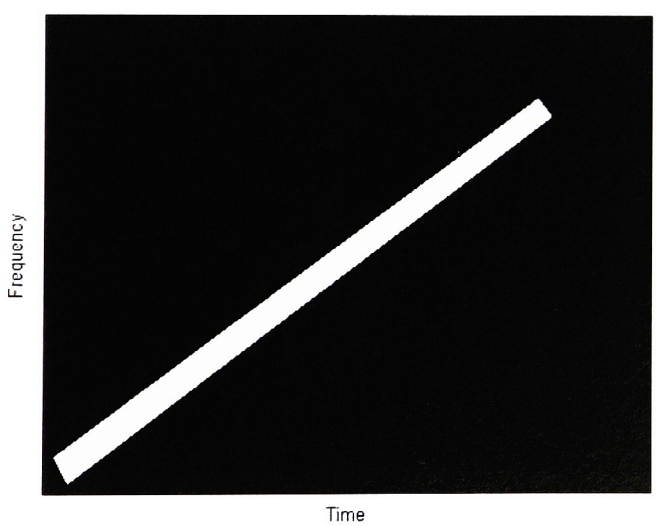

Figure 36: Slant window used as a ROI mask in TF processing

II. EQUIPMENT AND PROCESSING

Two separate Panametrics transducers, one to transmit the input drive signal and the other to receive the RF data were used. Both the transducers operated at a center frequency of 5MHz but their diameters were 0.375in and 0.25in respectively (Please refer to Appendix A for details and specifications of the transducers). The transducers were clamped on to a metal bridge connected to the stepper motor as shown in Fig. 37 and Fig. 38. The transducers were located such that the intersection point from the center of each transducer face would correspond to the focal points of each transducer based on their specifications. Hence, the total travel time to the object in study would be the sum of the travel time of the transmit drive transducer signal and the travel time to receive the RF signal at the receive transducer.

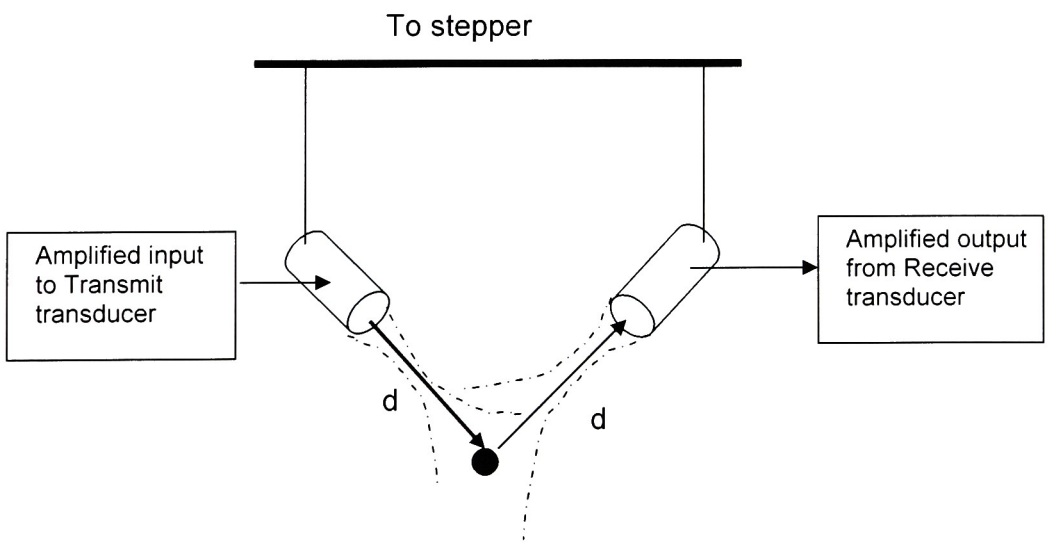

Figure 37: Cross-beam scanning geometry

To calibrate the system, the stepper motor micrometer combination was adjusted to receive the maximum signal from the wire target. The two transducers were securely tightened on the bridge such that the focal point intersection was at a distance $d_1 = 10\,\text{cm}$ and $d_2 = 5\,\text{cm}$.

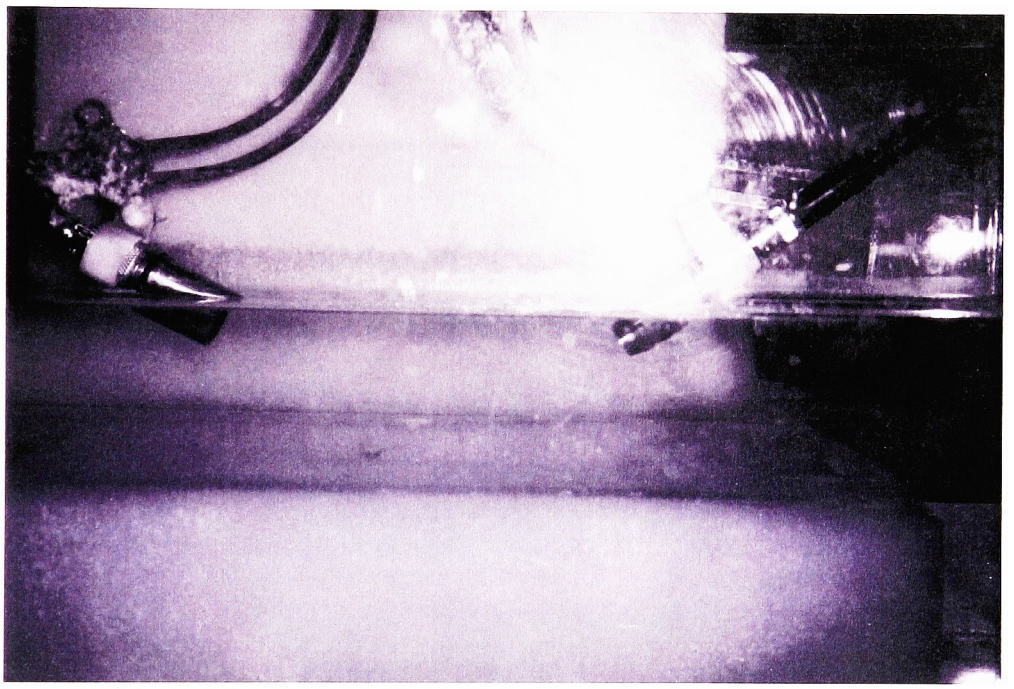

Figure 38: Transducer setup depicting cross-beam geometry

The transducers were immersed in a water tank that contained the wire target. The water tank was completely padded on all sides with thick sponges in order to prevent any reflection from the specular surface of the tank. A XY stepper motor was used to move the two transducers in unison laterally across the wire target and a manual micrometer to move the setup vertically. A 100x100 grid was scanned with a lateral spacing of 0.15mm

between each pixel on the grid. RF A-line echo data of interest as shown in Fig. 39 was digitized with a National Instruments NI 5112 8-bit digitizer. This resulted in a region-of-interest scan plane of 1.5cm by 1.5cm. Since the digitizer is installed on the PC via PCI-bus, RF data for each scan line could be captured into RAM and stored to a file for future processing.

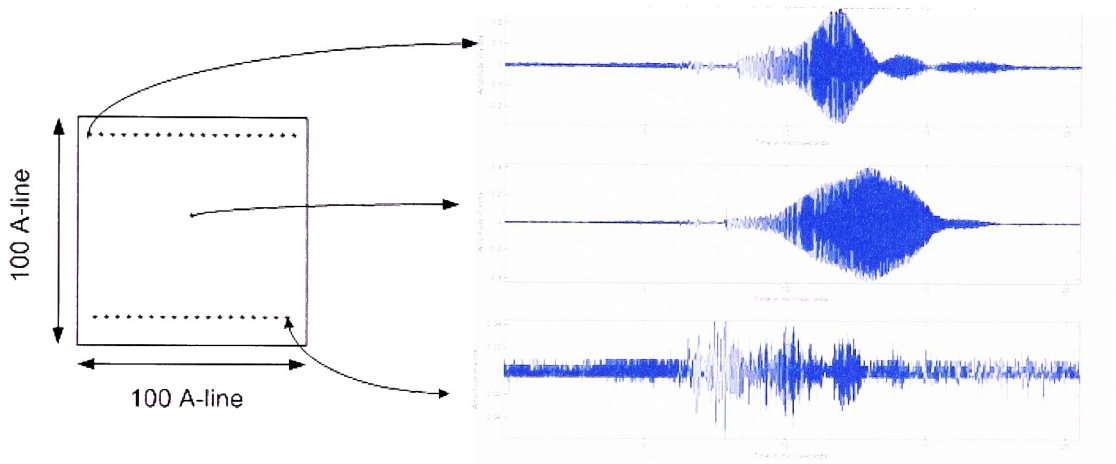

Figure 39: 100x100 A-line grid

The experimental setup is depicted in Fig. 40. Short pulse or Chirp pulse drive signals were synthetically generated using Matlab and loaded into National Instruments NI 5411 12-bit 40MSamples/sec arbitrary waveform generator. The input drive signal was then pre-amplified and fed to the transmit transducer. An overall National Instruments Virtual Instrument (VI) user-interface (UI) and processing components were connected to control the stepper motor in conjunction with the waveform generator and digitizer (Please refer to Appendix B for UI details). To keep the processing time to a bare minimum, the VI is

abstracted to capture the raw RF data so that it could be processed differently based on the imaging technique. All subsequent processing was done on the PC using Matlab. There were two types of scans' conducted using SP and FM as input drive signal. Data was calculated in a 100x100 grid:

- Vertical scan
- Horizontal scan

Let's visualize a vertical scan using Fig. 37. In this figure, the wire target is pointed 'into' the page and the two transducers are positioned as shown. Assume that the transducer assembly is moved in a left-right direction which represents the "X" axis using a stepper motor. The overall assembly is manually moved from top-to-bottom which represents the "Y" axis using a micrometer.

In the case of a horizontal scan, the wire target is still pointed 'into' the page. Assume that the transducer assembly is moved into-out of the page (using a stepper motor)in a horizontal plane which represents the "X" axis. The overall assembly is manually moved from top-to-bottom which represents the "Y" axis using a micrometer.

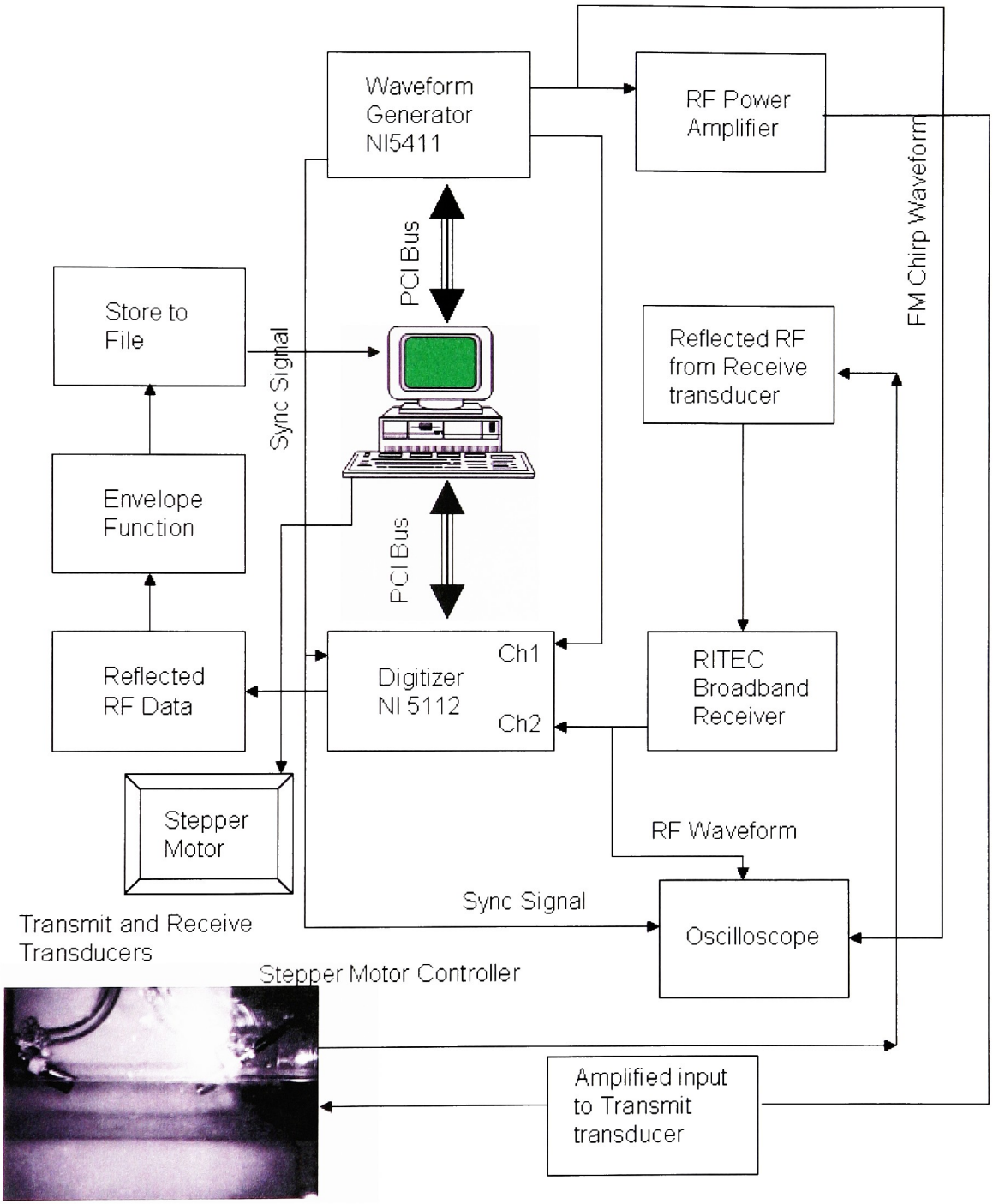

Figure 40: Cross-beam geometry experimental setup

III. EXPERIMENTS, IMAGES AND CONTOURS

Results obtained from twelve imaging experiments along with relevant imaging parameters are shown in Figs. 43-62 which are grouped at the end of this chapter for convenience. Figures containing grayscale image which depicts the 2D-PSF are followed by a 3D plot and a contour plot. The 3D mesh plot depicts the volume and shape of the PSF. The contour plot depicts the full-width-at-half-maximum (FWHM is the amplitude at -6dB or when the amplitude drops to one-half of the maximum amplitude) of the major and minor axis of the PSF.

Experiments in the absence of noise

A first set of experiments were conducted to investigate the four scanning techniques – Short pulse, FM with cross-correlation, STFT and WV. The experiments were scanned based on the two scanning types – vertical scan and horizontal scan. The 100x100 A-line data captured using FM technique was used as input to the STFT and WV study. Experimental data collection using Short Pulse and FM using cross-correlation were straightforward. There were various parameters that were setup while conducting the STFT and WV:

1. In STFT, the analysis window was chosen to be a Hamming window with a width of 256 (note there were 4096 data points for each A-line scan)

2. In STFT, the ROI mask as depicted in Fig. 36 was fixed in the time-frequency domain at the following coordinates:
    a. Lower mask: [46 1387], [2032 263], [2090 321] and [104 1471]
    b. Upper mask: [96 218], [314 99], [2394 1287] and [2175 1460]
3. In WV, the ROI mask was fixed at different coordinates on the time-frequency domain:
    a. Lower mask: [465 1318], [496 1337], [1600 38] and [1459 24]
    b. Upper mask: [664 515], [700 497], [1490 1430] and [1459 1448]

The following plots represent the noise-free cases:

- Figs. 44-45 represent SP processing using vertical scan data
- Figs. 48-49 represent FM processing using vertical scan data
- Figs. 52-53 represent SP processing using horizontal scan data
- Figs. 56-57 represent FM processing using horizontal scan data
- Figs. 60- represent STFT processing using vertical scan data
- Fig. 62 represents WV processing using vertical scan data
- Fig. 63 represents STFT processing using horizontal scan data

- Fig. 64 represents STFT processing of a fixed time-gate sum up energy at all frequencies using vertical scan data

Within figs. 44-45, 48-49, 52-53 and 56-57, the sub-sequence of figures is as follows:

- First figure is noise-free case at a particular time-gated location
- Second figure is noise-free case where an average of +/- five locations around the time-gate are calculated to post a single entry

Experiments in the presence of additive white noise

The experiments using the four scanning techniques were repeated with additive white noise added to each original A-line data. Figs. 41 and 42 depict the sample realizations of RF data from SP and FM technique in the presence of additive white noise. Note, a unique realization of the additive noise is created for each instance. The standard deviation of the additive white noise was calculated based on the center line maximum A-line scan. The same amount of noise was added to each A-line scan except that it was a unique realization. The input SNR for the center A-line scan was calculated as follows:

$$SNR_{input} = \frac{\text{Amplitude of the signal}}{\sigma_{noise}} \tag{7.1}$$

The output SNR for the 100x100 image was calculated by first locating the peak value in the 2D PSF image. A 5x5 average of the pixels around the peak value was calculated. In addition, a 20x20 average standard deviation of the pixel values between coordinates [80, 80] and [100,100] was calculated.

$$SNR_{output} = \frac{5x5 \text{ average around the peak value}}{\sigma_{noise} \text{ across 20x20 pixel values}} \tag{7.2}$$

The following plots represent the simulated additive noise cases:

- Figs. 46-47 represent SP processing using vertical scan data
- Figs. 50-51 represent FM processing using vertical scan data
- Figs. 54-55 represent SP processing using horizontal scan data
- Figs. 58-59 represent FM processing using horizontal scan data
- Figs. 61 represent STFT processing using vertical scan data

Within figs. 46-47, 50-51, 54-55 and 58-59, the sub-sequence of figures is as follows:

- First figure is in the presence of additive white noise at a particular time-gated location
- Second figure is in the presence of additive white noise where an average of +/- five locations around the time-gate are calculated to post a single entry

IV. DISCUSSION OF RESULTS

From Table 2, it can be noted that along a noise-free vertical scan, FM Chirp cross-correlation processing provided the highest resolution. This was followed by STFT/WV processing with Short pulse being the worst. Along a noise-free horizontal scan, Short pulse provided the highest resolution followed by FM and STFT. In the presence of additive white noise, a vertical scan provided comparative results for SP and FM.

Scanning technique	For vertical scan along the X direction (mm)	For vertical scan along the Y direction (mm)	For horizontal scan along the X direction (mm)	For horizontal scan along the Y direction (mm)
Noise Free Case				
SP	7.35	0.9	10.5+	0.75
FM	5.85	1.05	12+	1.05
STFT	6.9	7.95	15+	5.25
WV	6.9	4.5	-	-
Noisy Case				
SP	5.25	1.05	Impossible to discern	Impossible to discern
FM	5.7	1.05	12+	1.05
STFT			-	-

Table 2: Comparison of FWHM for each technique

In addition, it is important to note that the resolution was the best when measured along the Y direction. An important caveat, the experimental setup of the transducer assembly along with calibration process is very critical to measure consistent results. For example, if the two transducers are not located in the same plane but are offset or the focal point of the transducers maps to the intersection point.

In the presence of additive white noise, a horizontal scan using SP resulted in the signal completely buried in noise. The amount of noise did not affect FM Chirp cross-correlation processing as the signal got enhanced after cross-correlation and envelope detection. Table 3 lists the SNR calculated using Eq. (7.1) and Eq. (7.2). The gain in SNR for the FM cross-correlation cases were very close to the predicted value of 22dB. The predicted value can be calculated with the following information: input drive signal

duration ($90\,\mu s$) and the bandwidth of the transducer system 2MHz. SNR for a compressed pulse is calculated as follows:

$$SNR(dB) = 20\log_{10}\left[\sqrt{(T_{\text{duration of the drive signal}})\cdot(\text{Transducer bandwidth})}\right] \quad (7.3)$$

Scanning Technique	Input A-line SNR (dB)	Output SNR (dB)
SP horizontal scan	7.2344	12.4235
FM horizontal scan	14.3919	35.2218
SP vertical scan	1.4133	7.5521
FM vertical scan	6.3416	26.6132

Table 3: SNR comparison amongst the scanning techniques

The analysis of the improvement in resolution could be explained using Fig. 41. The resolution along the tight Y-direction depends on the pulse width of the compressed pulse. It is also a function of the selection of the time gate. The resolution along the broad X-direction of the PSF is controlled by the beam pattern created by the overlapping beams. It was in the order of a few mm's due to the use of unfocused transducers. Some general observations:

- The PSF of STFT and WV was slightly worse compared to SP and FM cross-correlation techniques

- The PSF of WV does not have an analysis window, yet the PSF is not any better than STFT
- The PSF along the horizontal direction could be tightened using focused transducers
- The time to compute STFT and WV is very large compared to SP and FM cross-correlation techniques

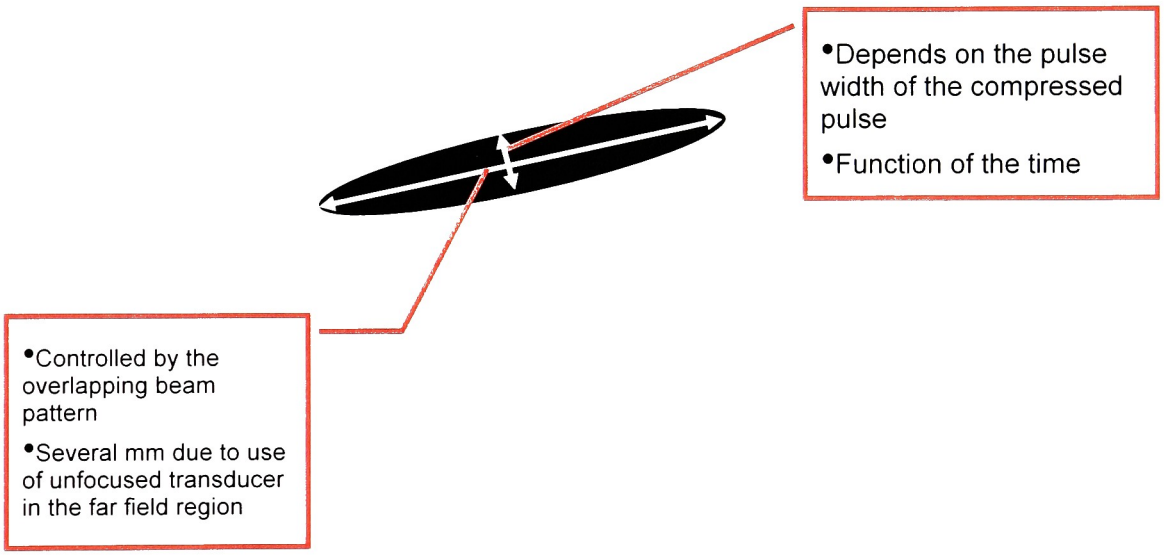

Figure 41: Analysis of PSF

V. CHAPTER SUMMARY

This chapter provided a brief experimental investigation of SP, FM and time-frequency transformation techniques developed in the previous chapters. Specifically, STFT and WV were extremely time consuming data processing methods as compared to SP or FM. The B-scan PSF images were compared only qualitatively. FWHM provided a important metric in quantitatively comparing the resolutions between the various techniques. The experimental results prove that FM cross-correlation processing appears to have the highest resolution followed by SP and STFT/WV. In addition, FM cross-correlation processing performed much better than SP or STFT in the presence of simulated additive white noise with an improvement of 22dB.

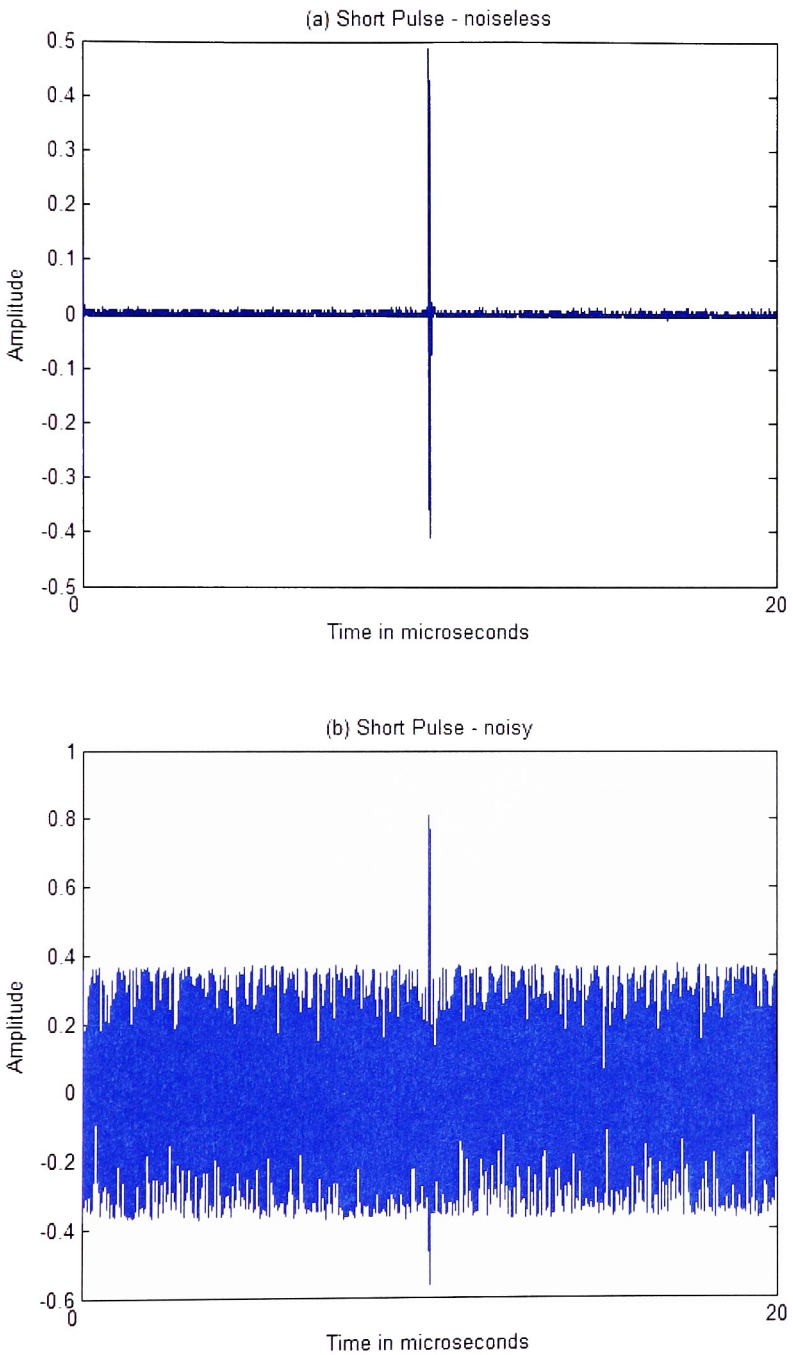

Figure 42: Short Pulse signal displaying additive white noise for a single A-line

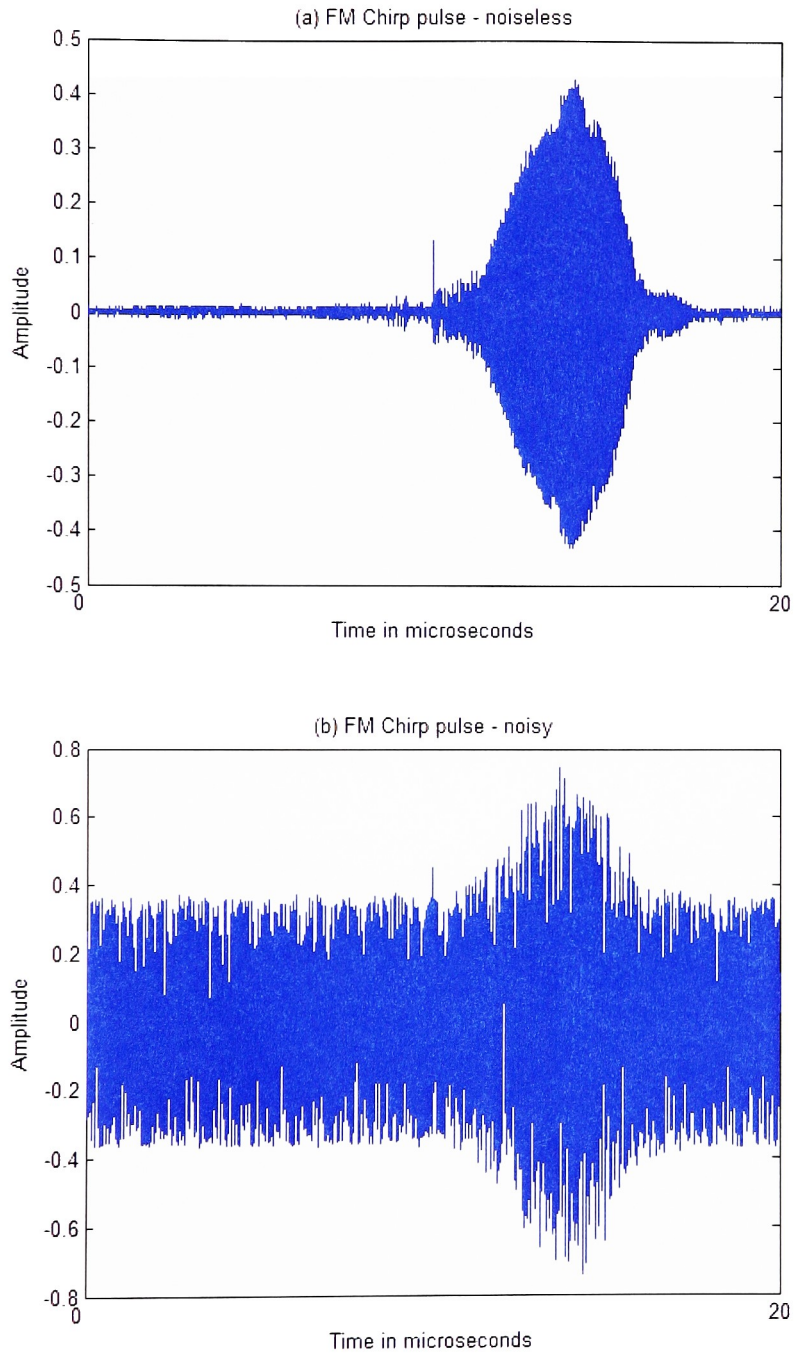

Figure 43: FM Chirp Pulse signal displaying additive white noise for a single A-line

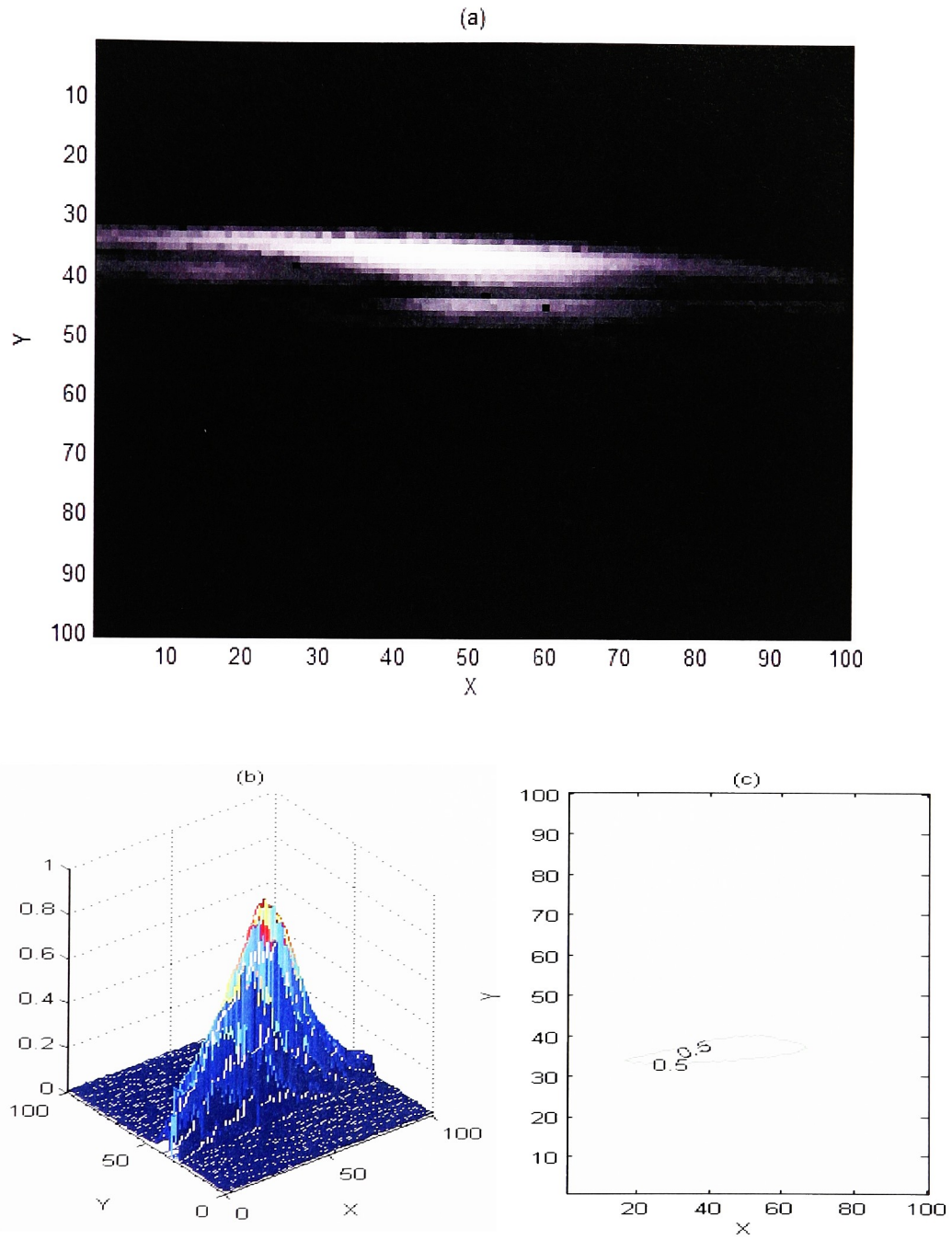

Figure 44: Short Pulse at a single time gate – noise-free – vertical scan (1pixel = 0.15mm)

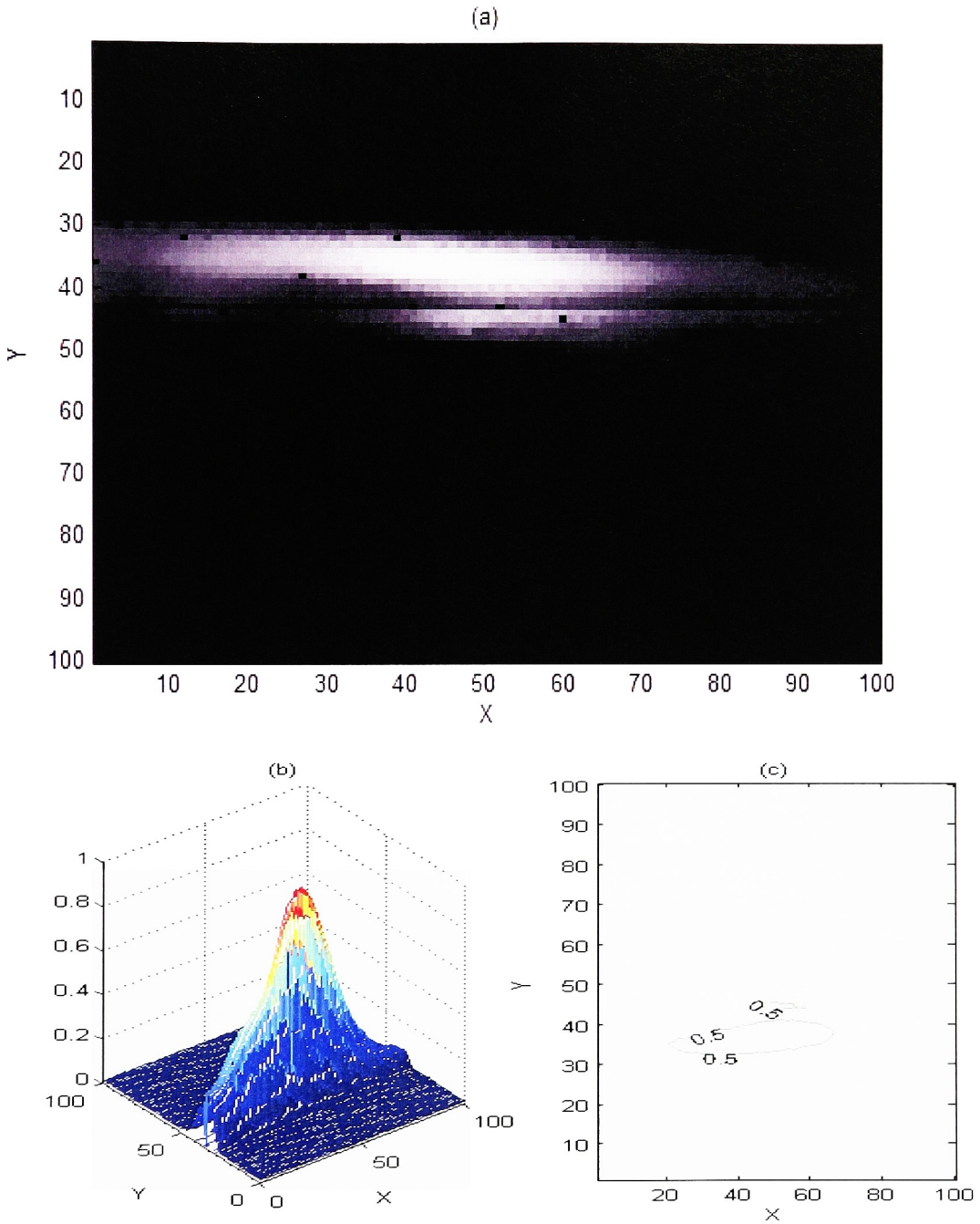

Figure 45: Short Pulse averaged between +/- 5 points around the time gate – noise-free – vertical scan (1pixel = 0.15mm)

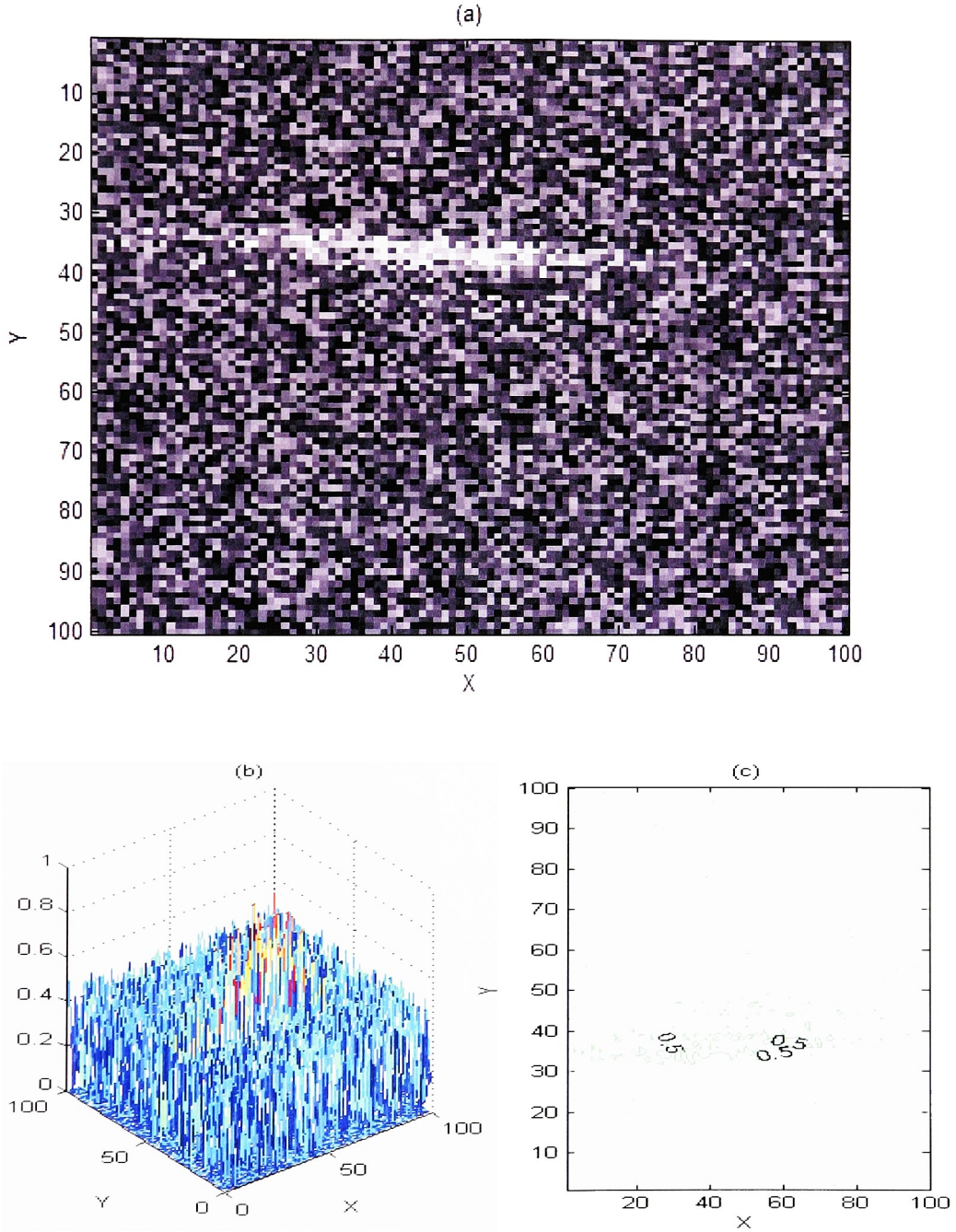

Figure 46: Short Pulse at a single time gate – noisy – vertical scan (1pixel = 0.15mm)

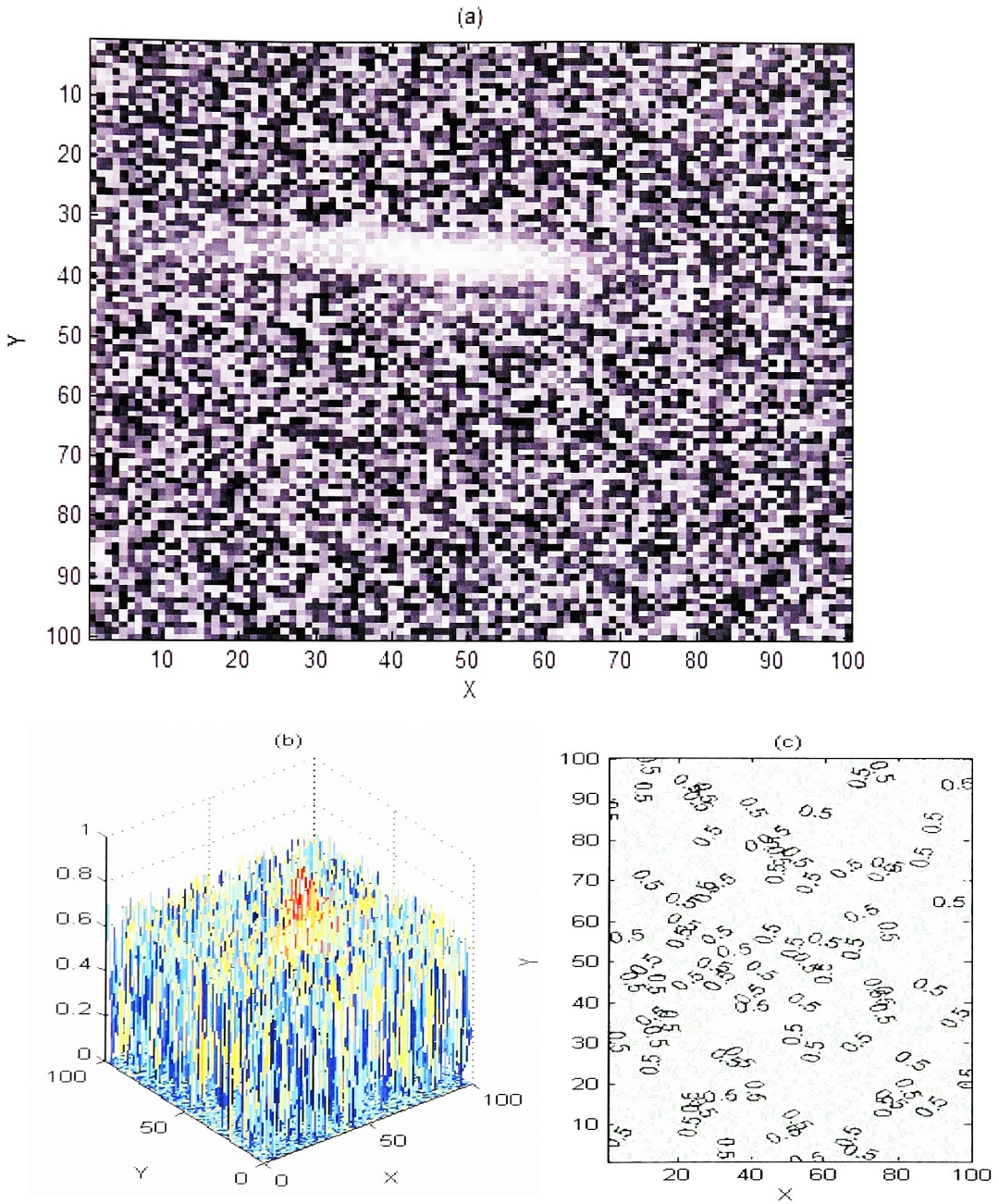

Figure 47: Short Pulse averaged between +/- 5 points around the time gate – noisy – vertical scan (1pixel = 0.15mm)

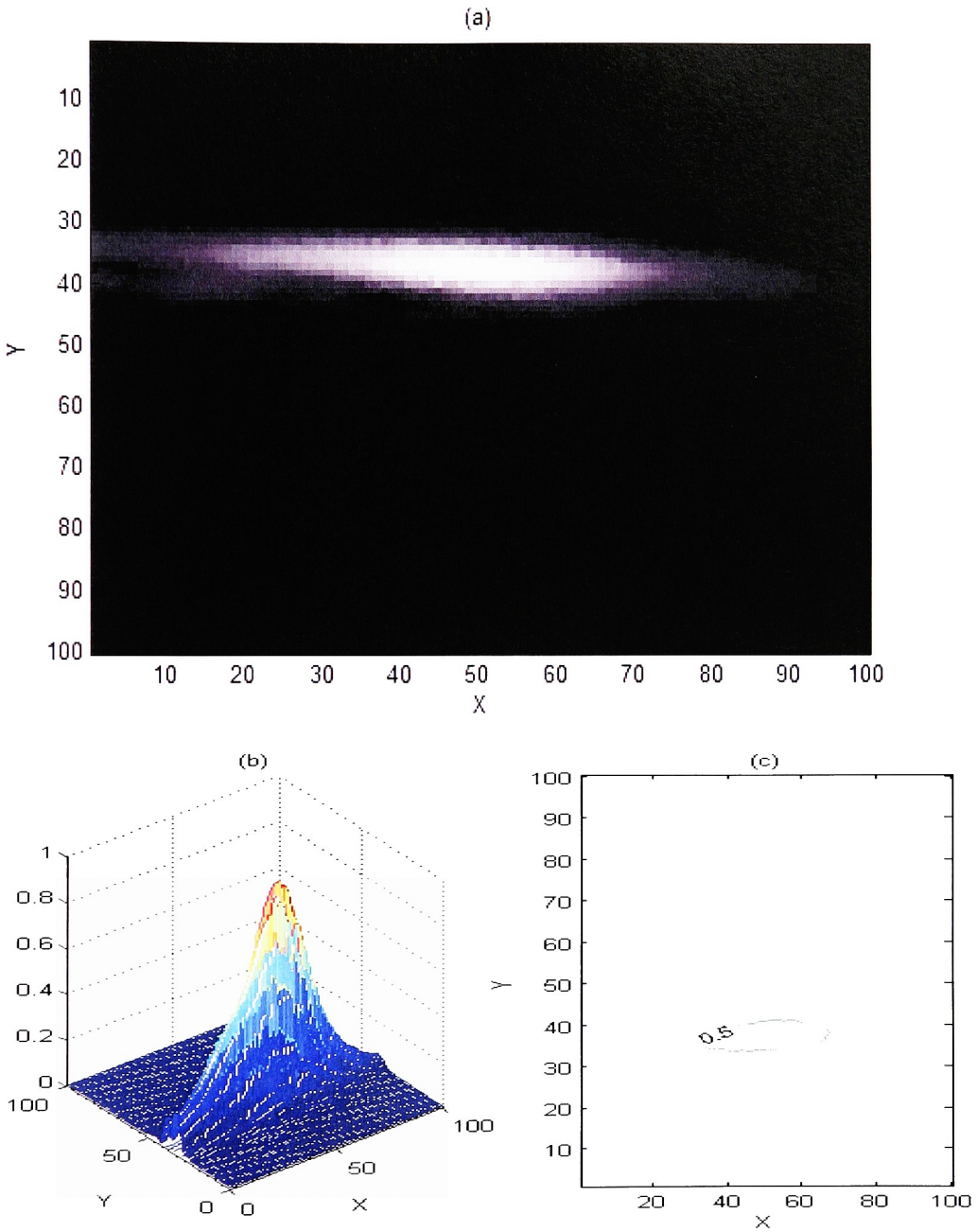

Figure 48: FM Chirp Pulse at a single time gate – noise-free – vertical scan (1pixel = 0.15mm)

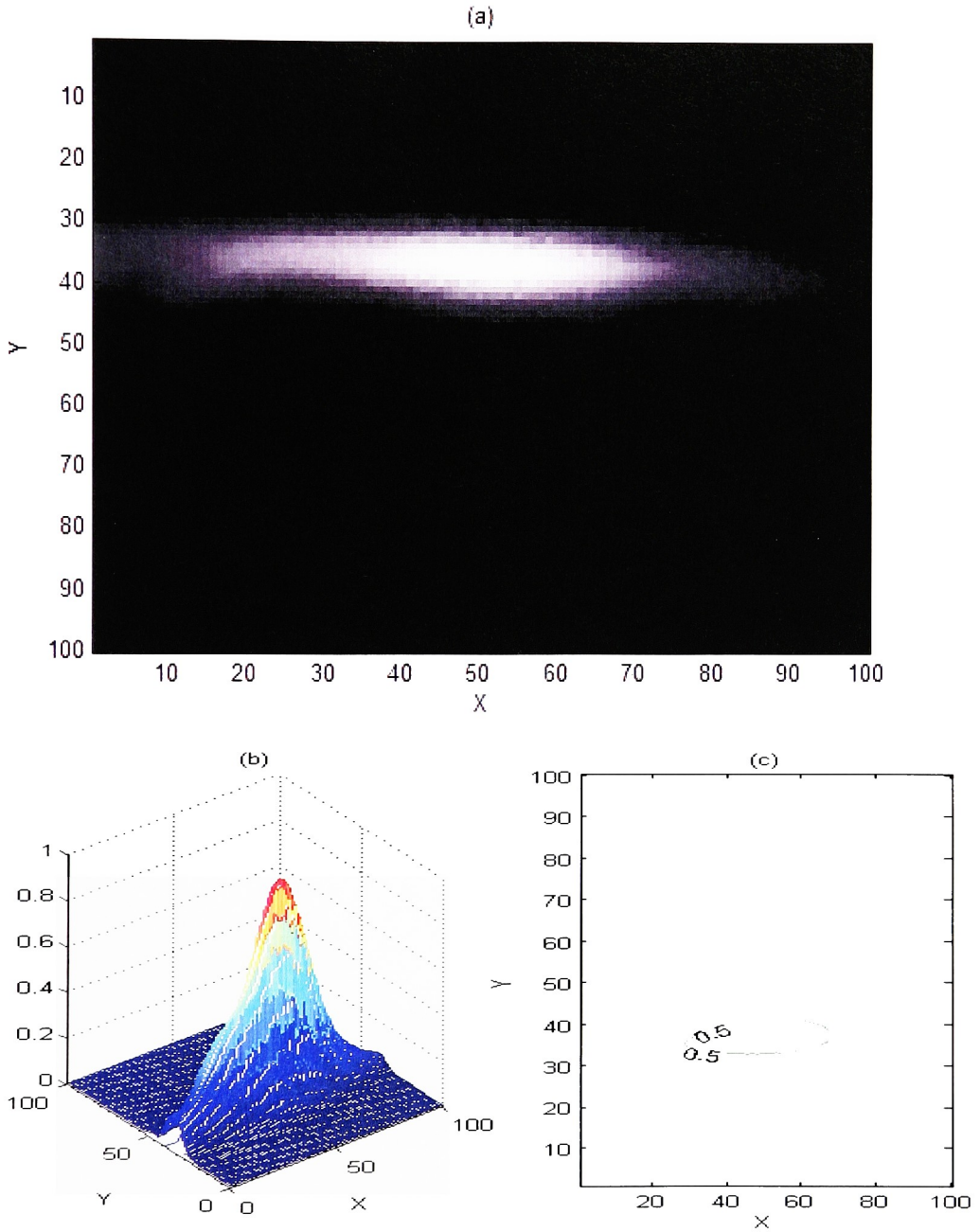

Figure 49: FM Chirp Pulse averaged between +/- 5 points around the time gate – noise-free – vertical scan (1pixel = 0.15mm)

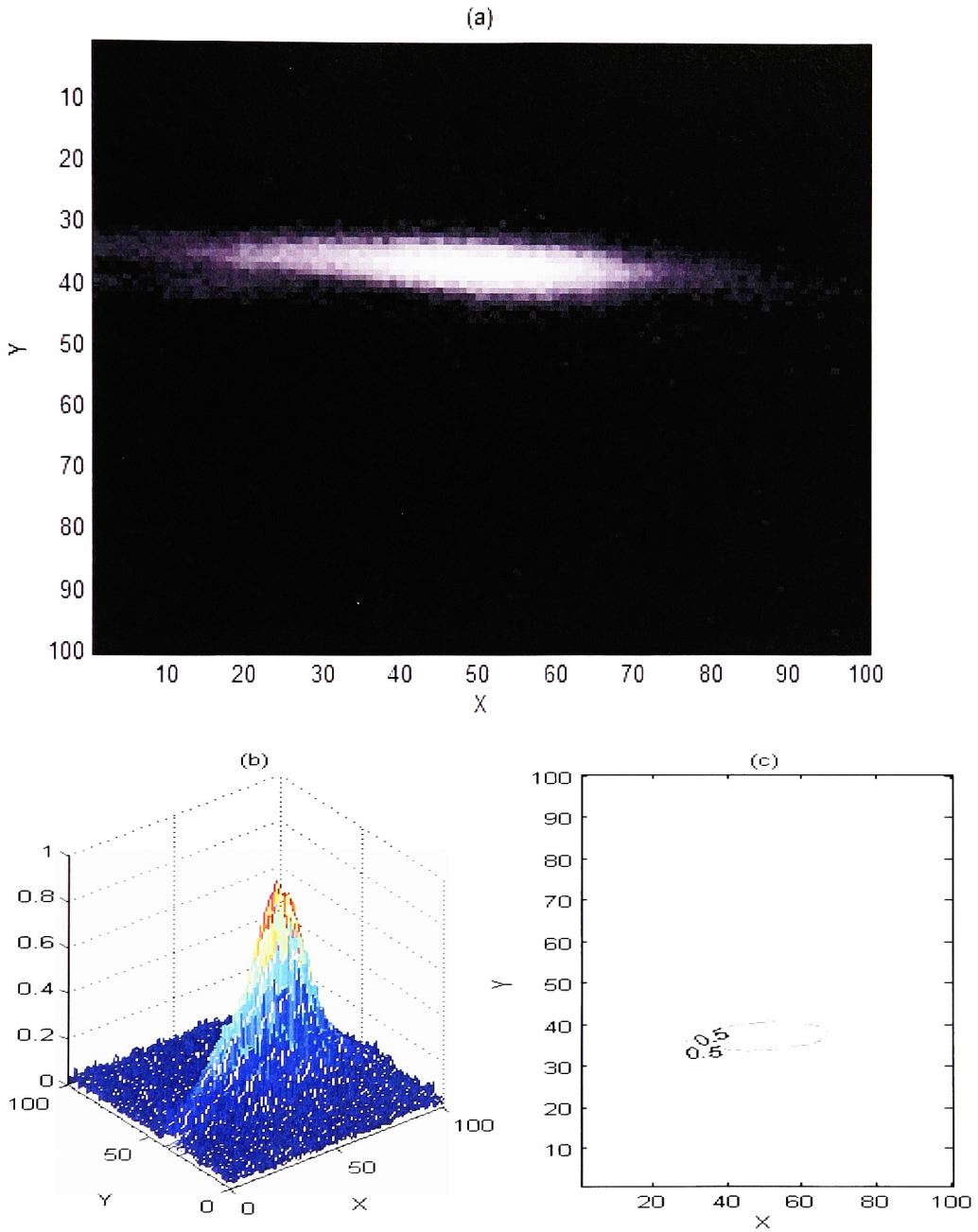

Figure 50: FM Chirp Pulse at a single time gate – noisy – vertical scan (1pixel = 0.15mm)

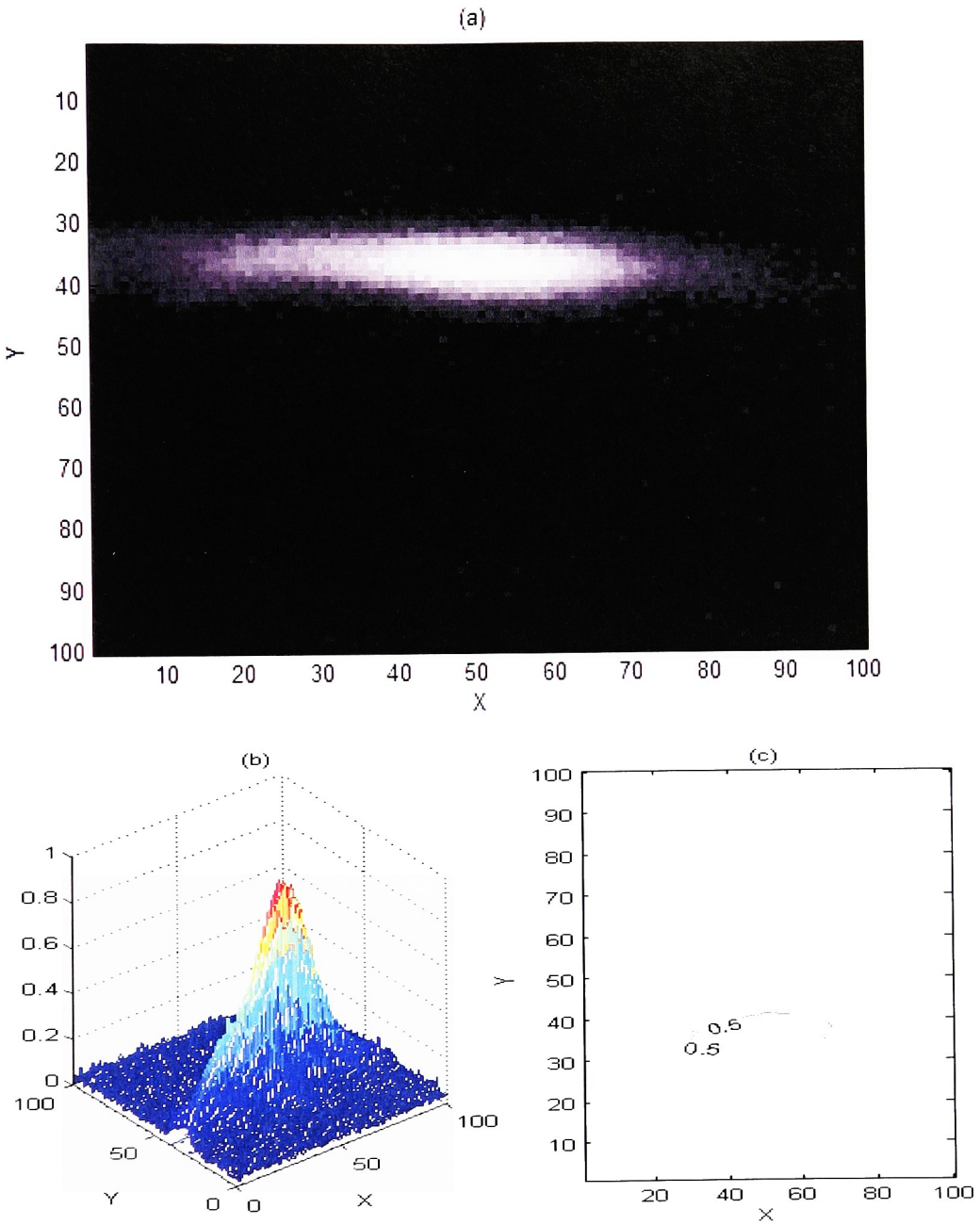

Figure 51: FM Chirp Pulse averaged between +/- 5 points around the time gate – noisy – vertical scan (1pixel = 0.15mm)

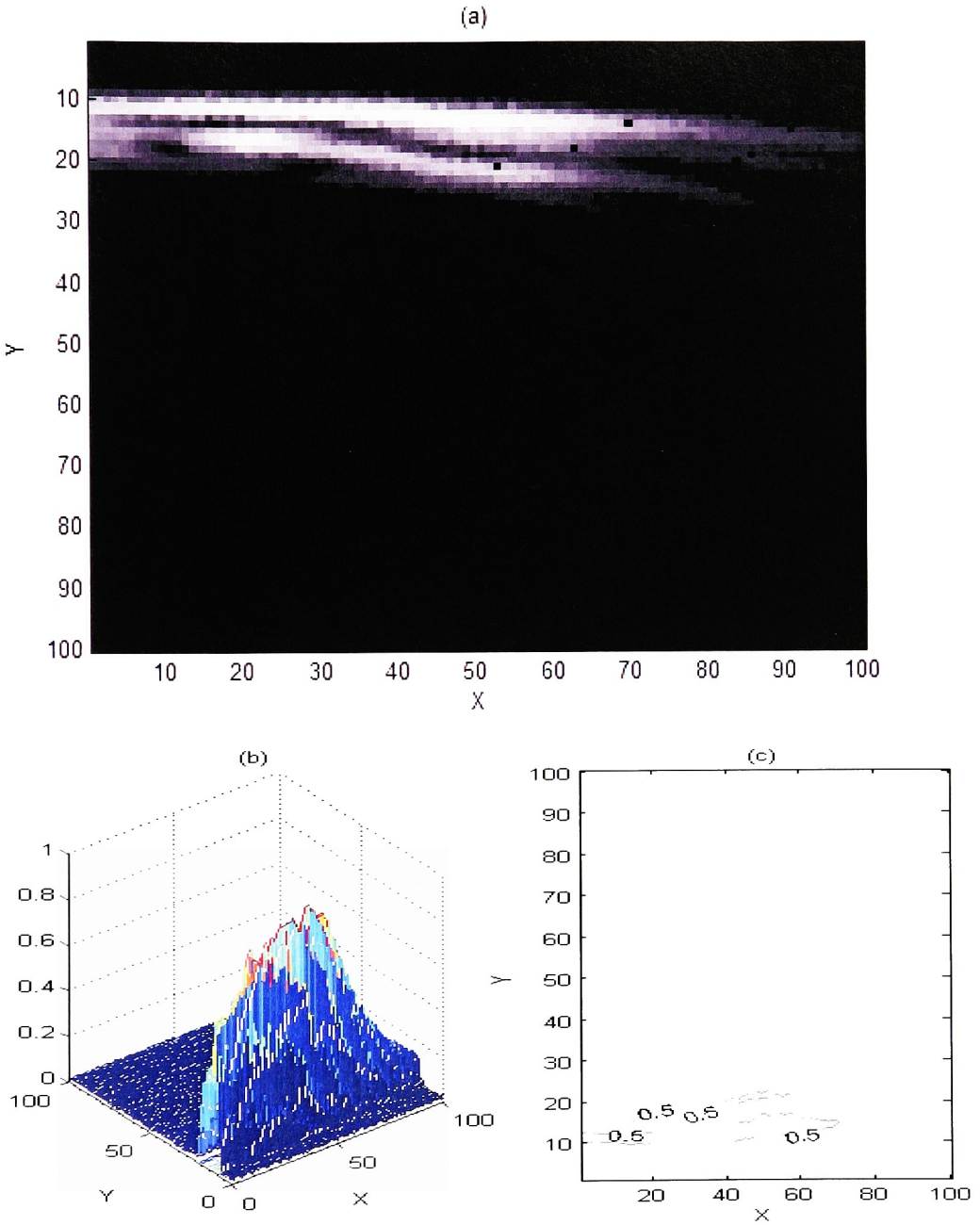

Figure 52: Short Pulse at a single time gate – noise-free – horizontal scan (1pixel = 0.15mm)

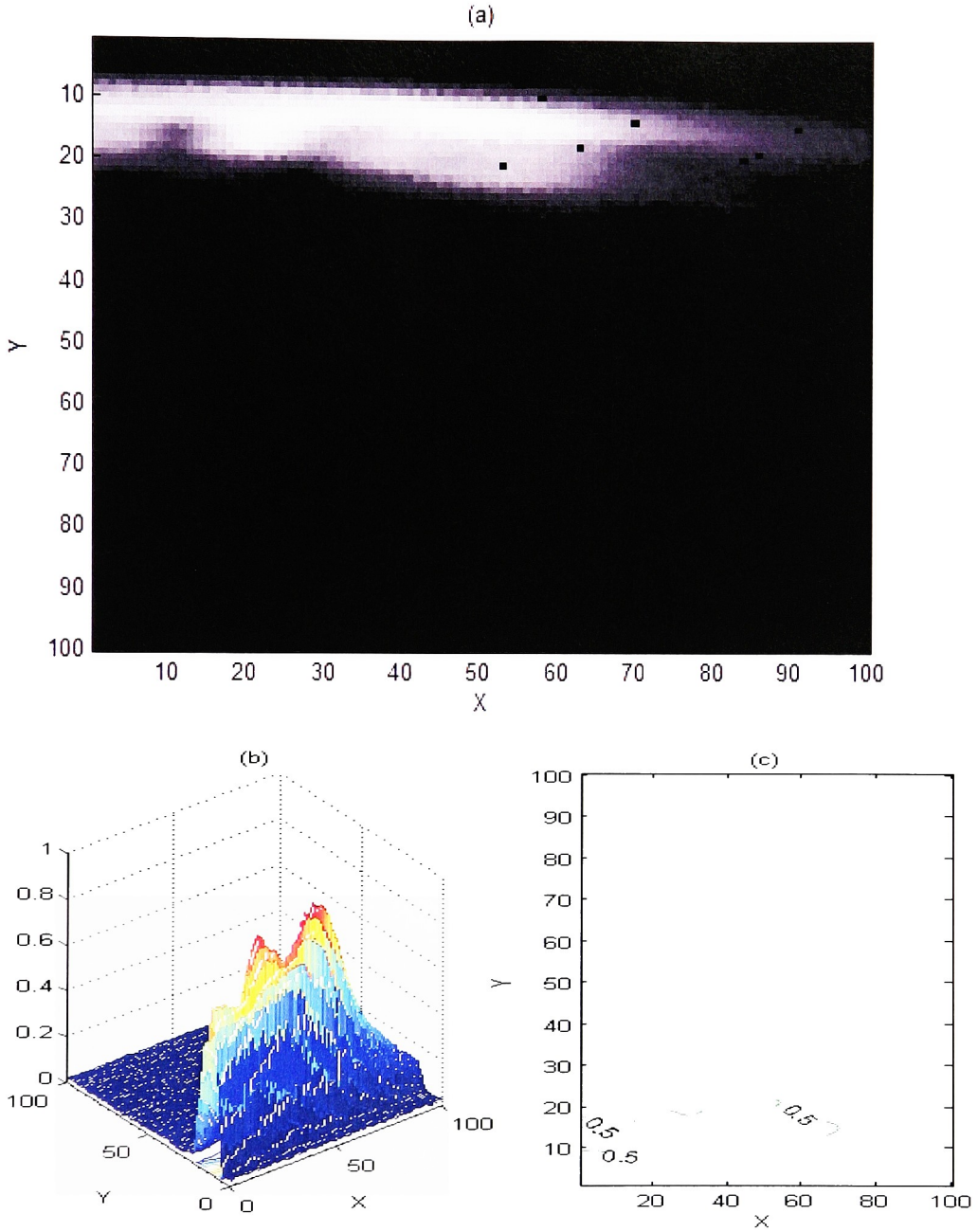

Figure 53: Short Pulse averaged between +/- 5 points around the time gate – noise-free - horizontal scan (1pixel = 0.15mm)

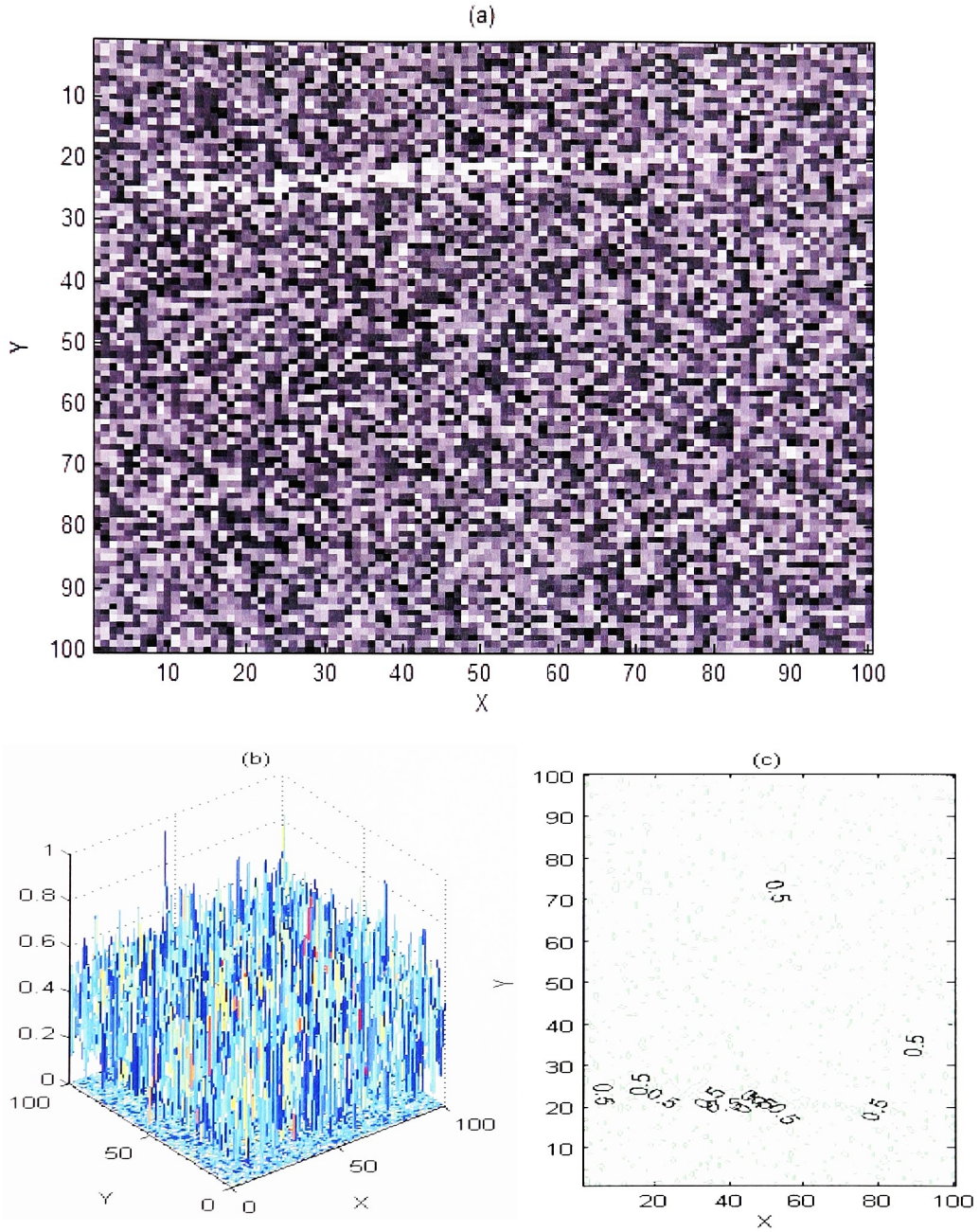

Figure 54: Short Pulse at a single time gate – noisy - horizontal scan (1pixel = 0.15mm)

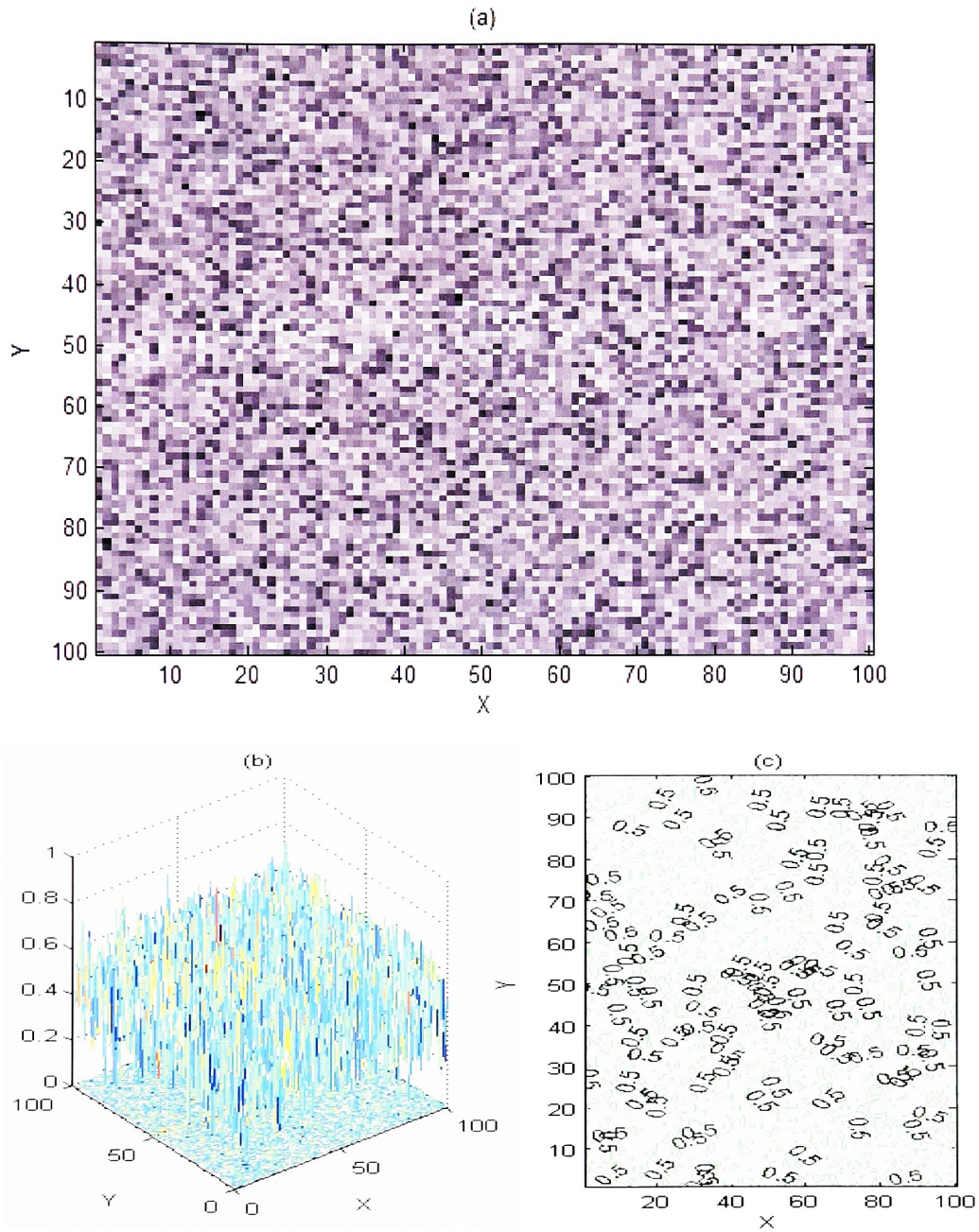

Figure 55: Short Pulse averaged between +/- 5 points around the time gate – noisy - horizontal scan (1pixel = 0.15mm)

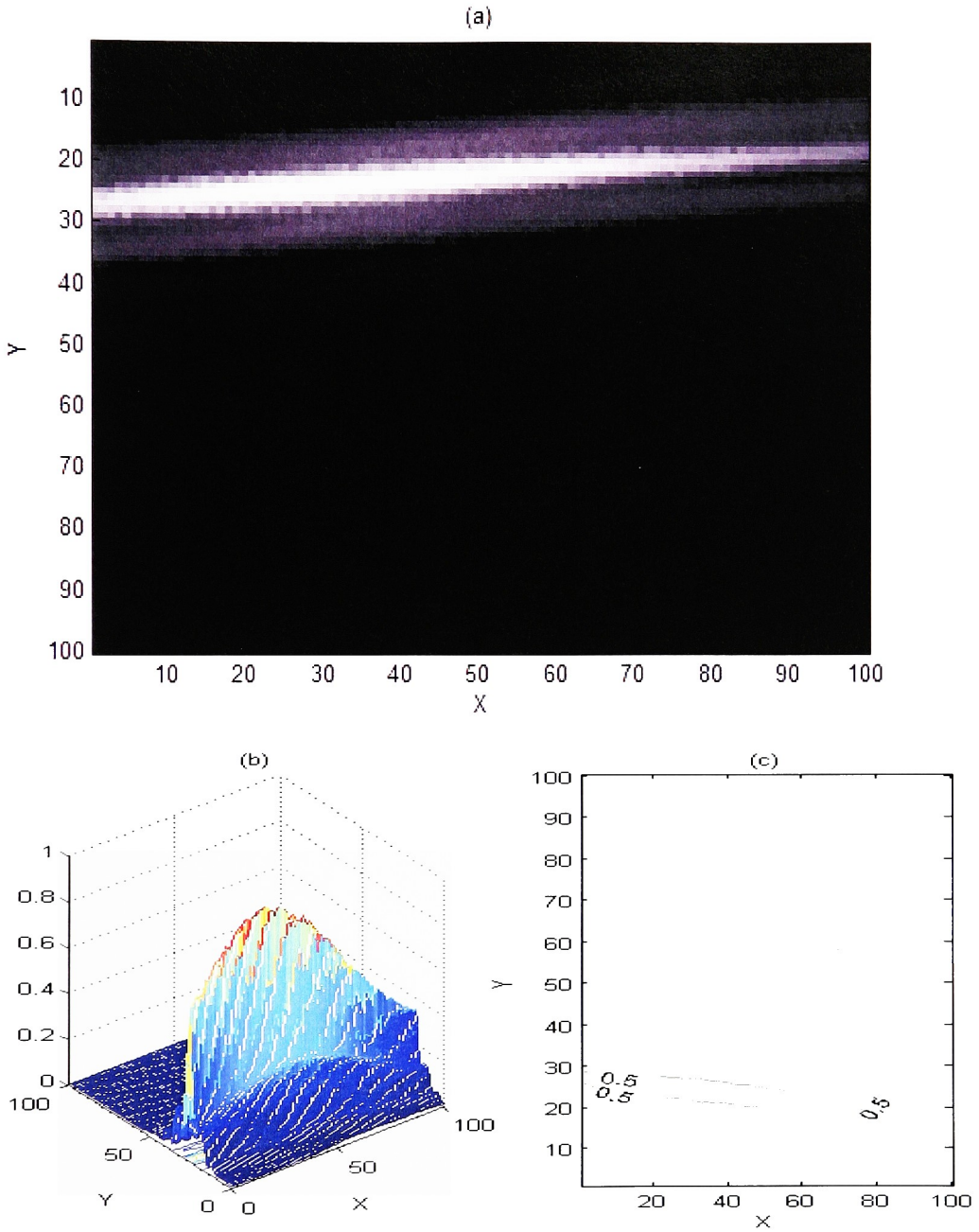

Figure 56: FM Chirp Pulse at a single time gate – noise-free - horizontal scan (1pixel = 0.15mm)

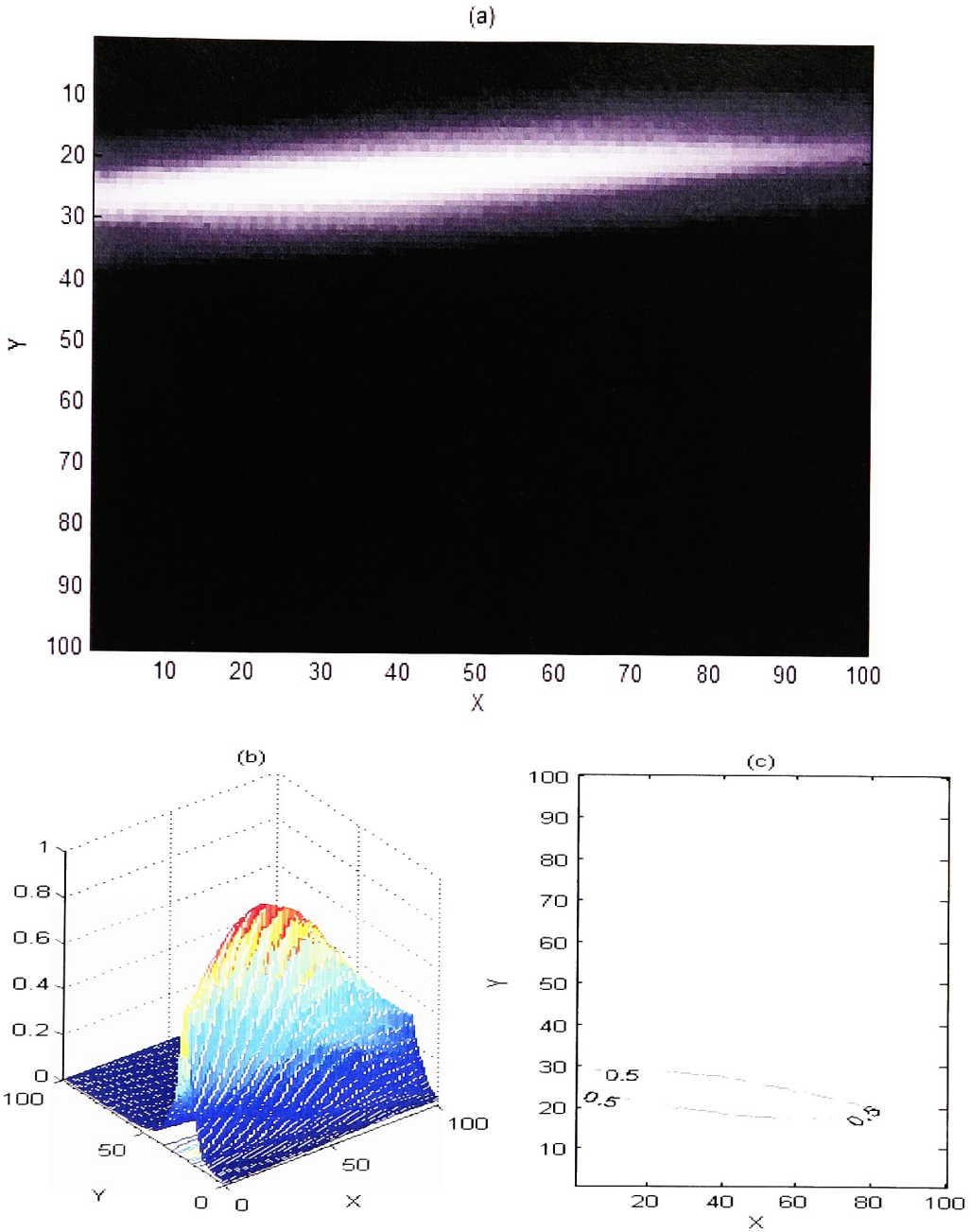

Figure 57: FM Chirp Pulse averaged between +/- 5 points around the time gate – noise-free - horizontal scan (1pixel = 0.15mm)

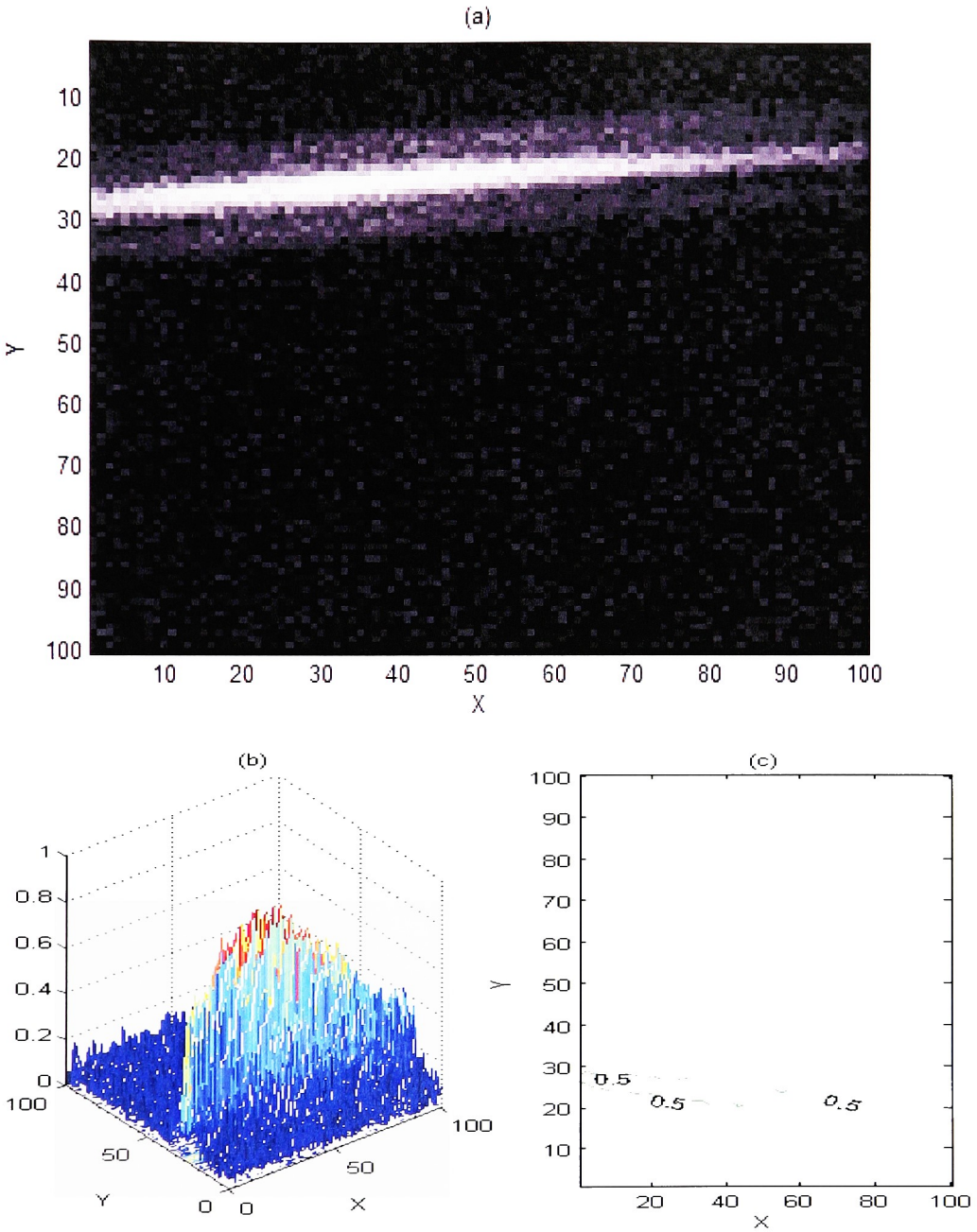

Figure 58: FM Chirp Pulse at a single time gate – noisy – horizontal scan (1pixel = 0.15mm)

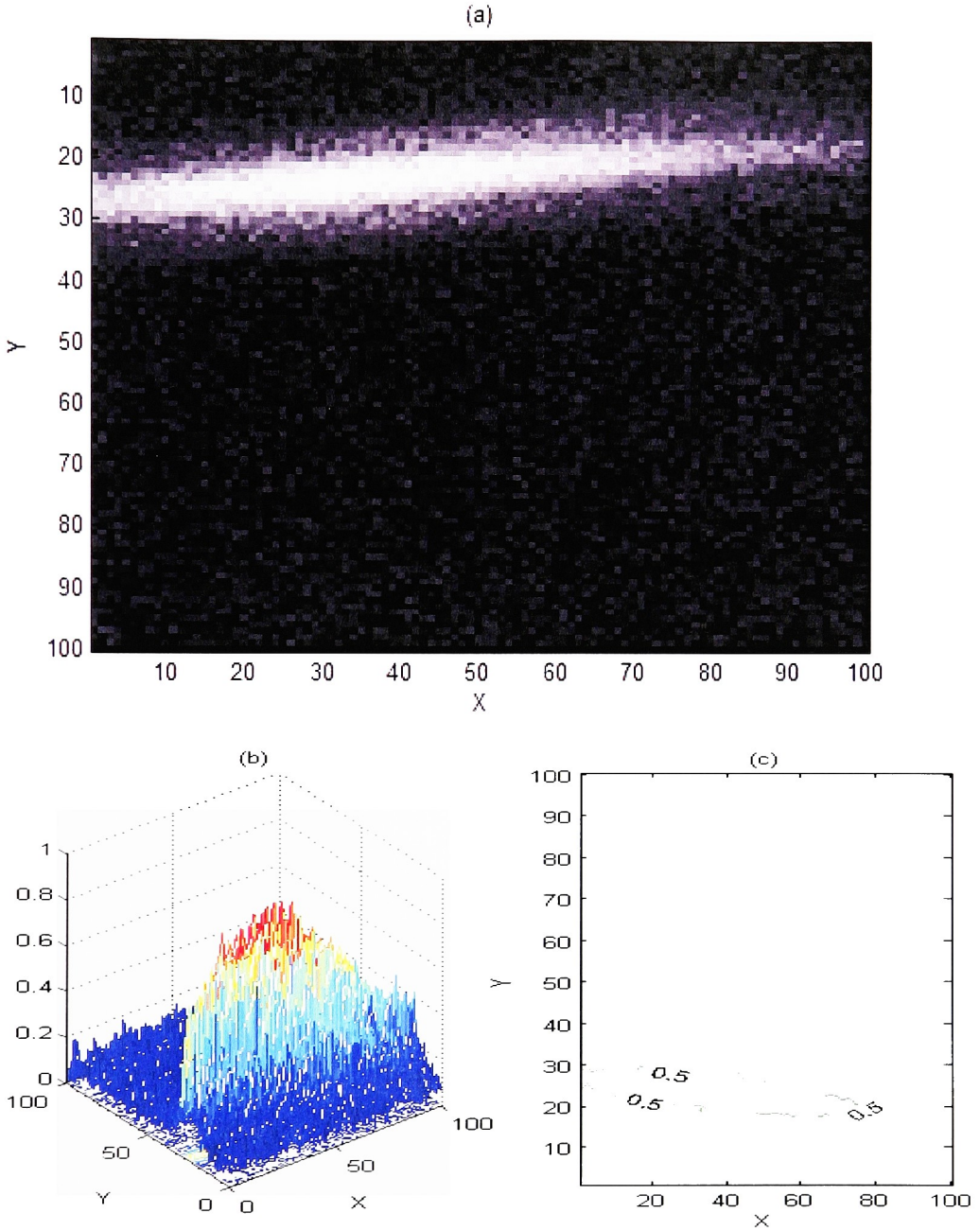

Figure 59: FM Chirp Pulse averaged between +/- 5 points around the time gate – noisy - horizontal scan (1pixel = 0.15mm)

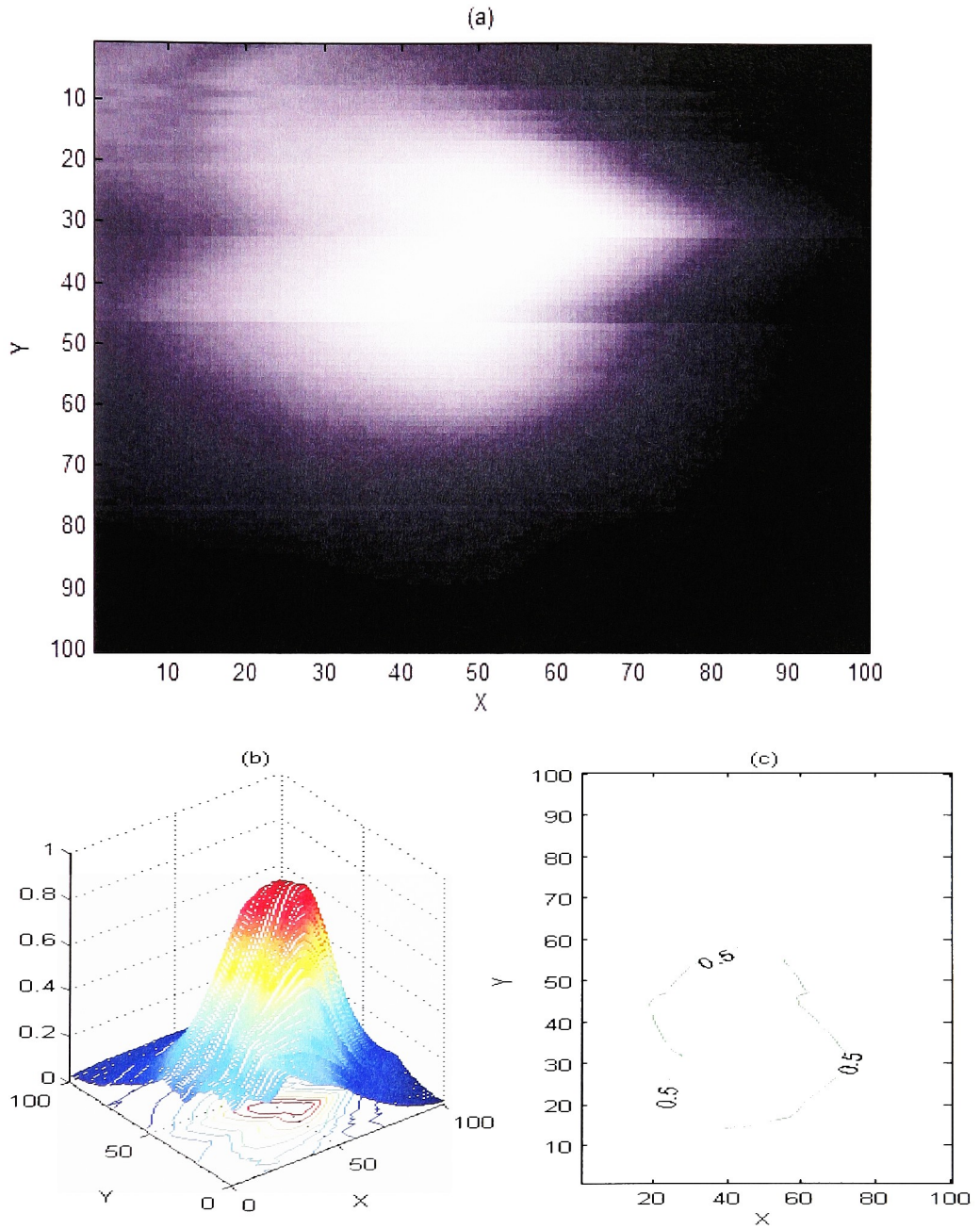

Figure 60: STFT calculated for a fixed slant window – noise-free – vertical scan (1pixel = 0.15mm)

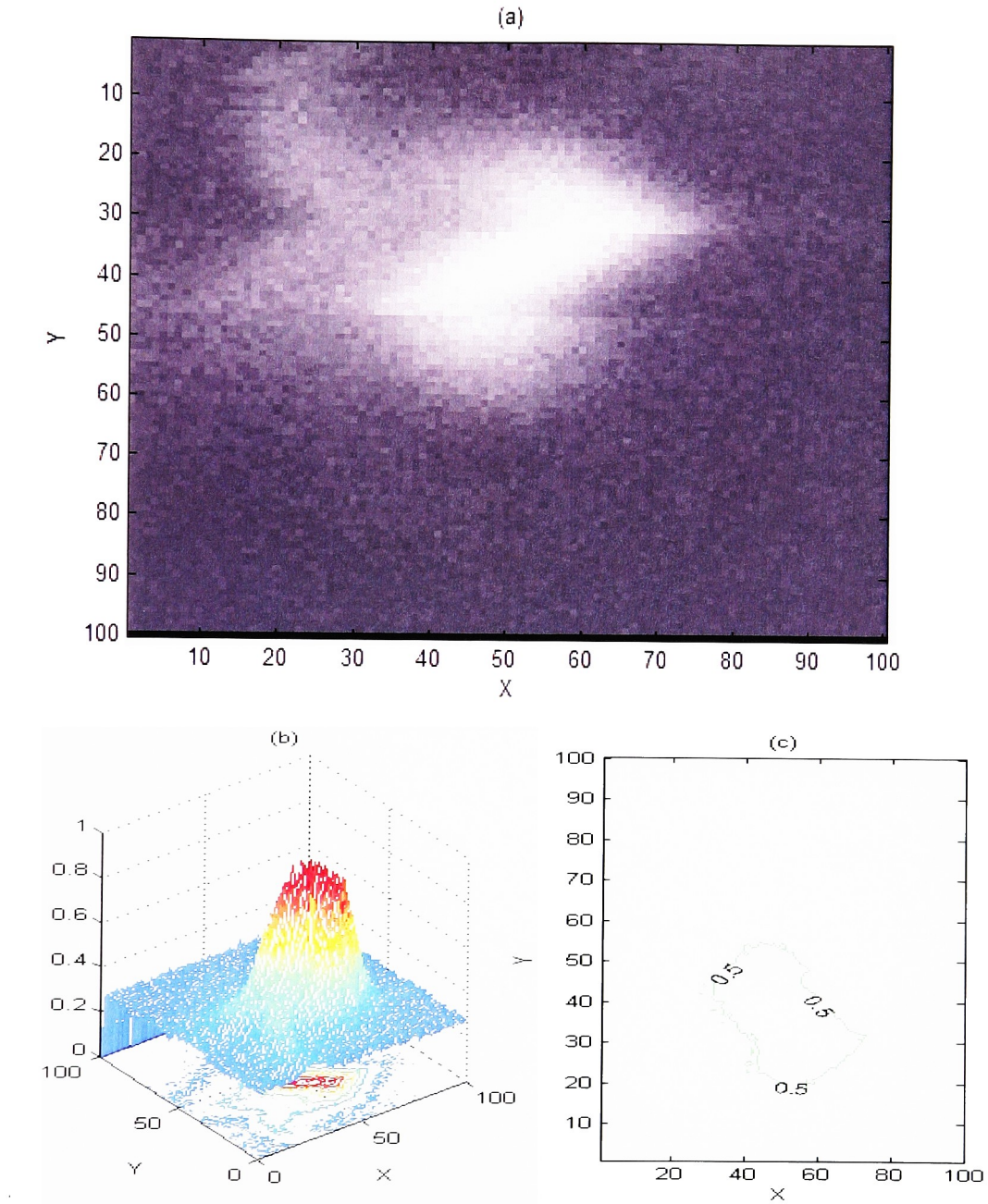

Figure 61: STFT calculated for a fixed slant window – noisy – vertical scan (1pixel = 0.15mm)

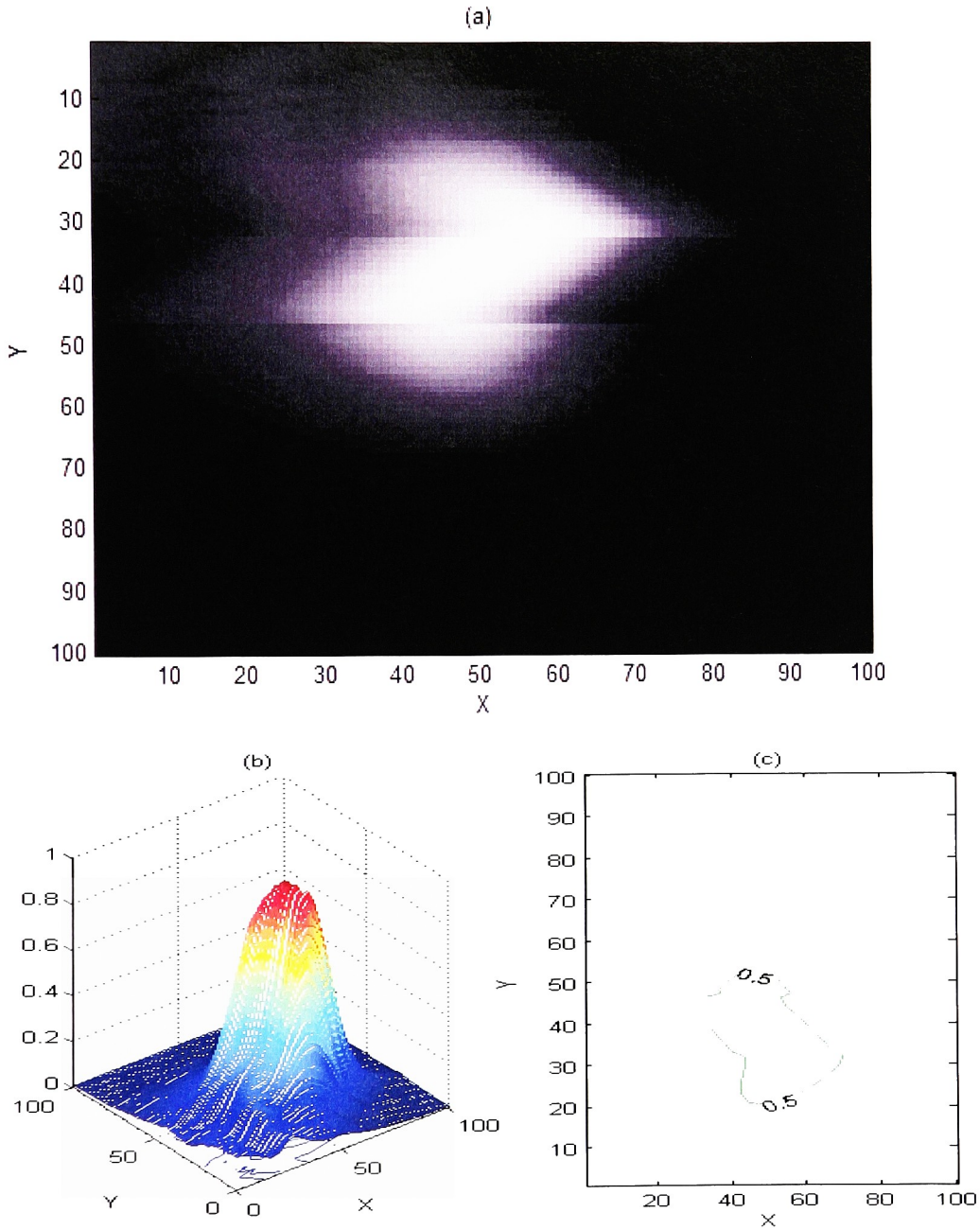

Figure 62: Wigner-Villet calculated for a fixed slant window – noise-free – vertical scan (1pixel = 0.15mm)

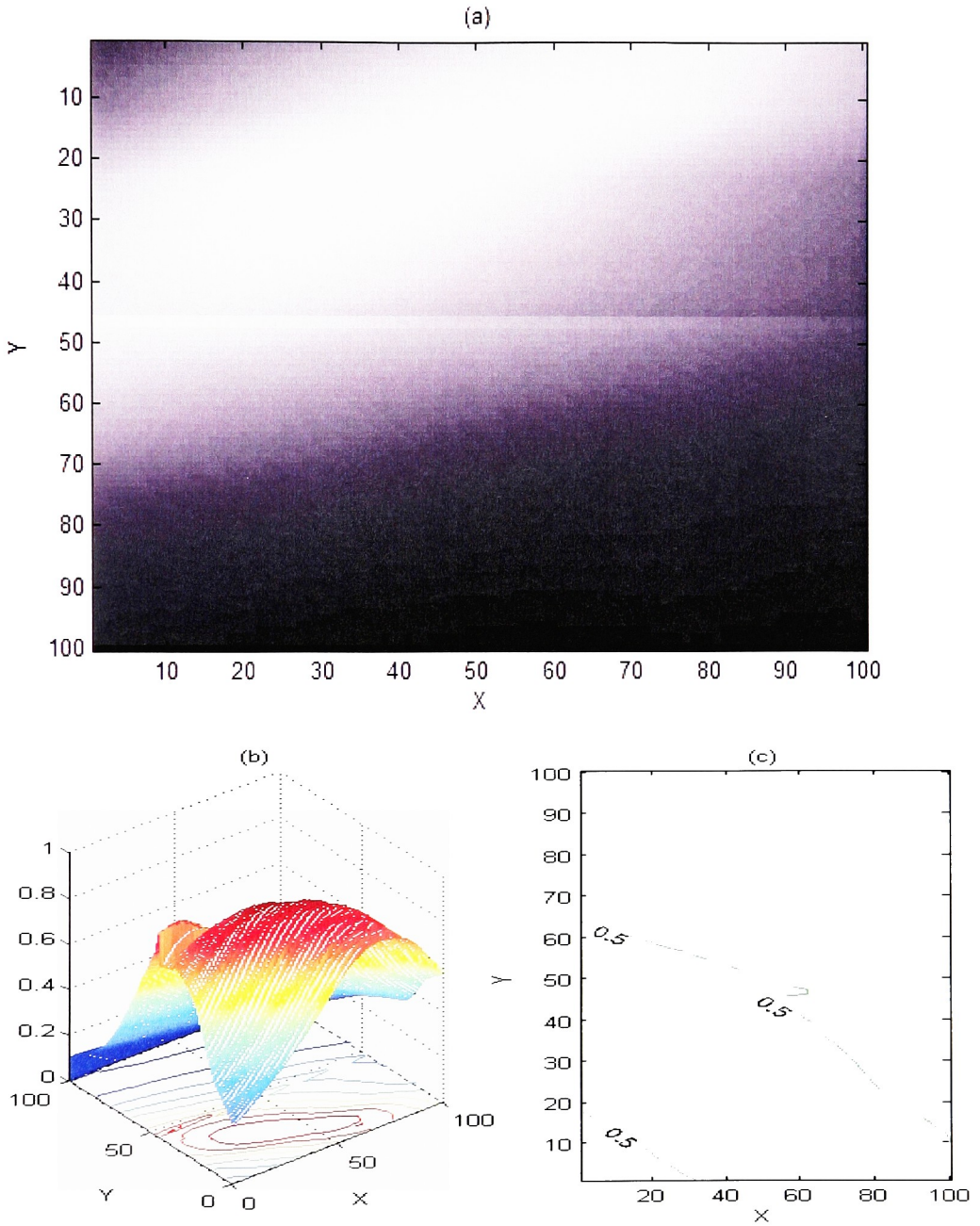

Figure 63: STFT calculated for a fixed slant window – noise-free – horizontal scan (1pixel = 0.15mm)

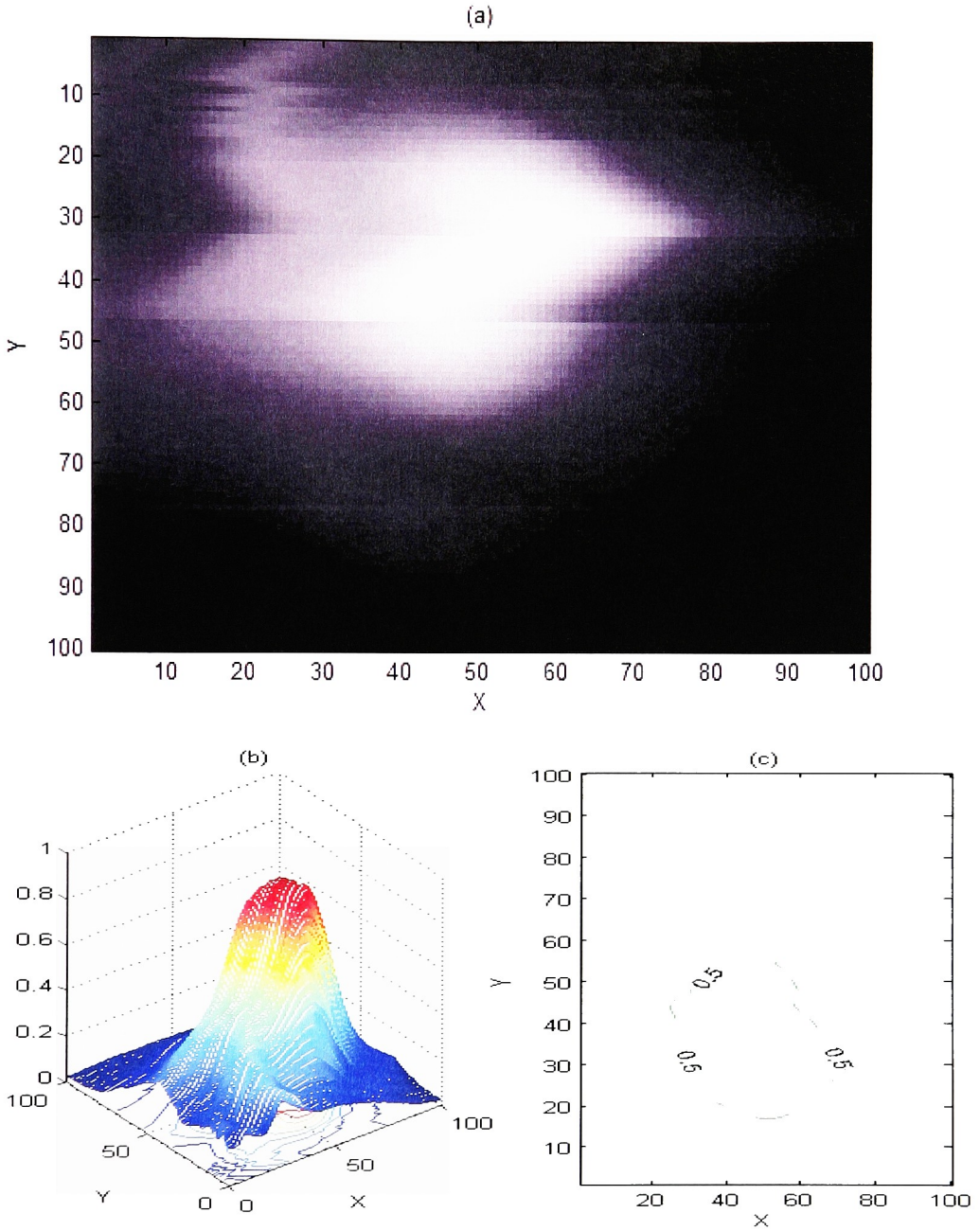

Figure 64: STFT calculated for a fixed time-gate summing up energy at all frequencies – noise-free – vertical scan (1pixel = 0.15mm)

Chapter 8

CONCLUSIONS, CONTRIBUTIONS AND RECOMMENDATIONS

This research has investigated the theory behind pulse compression processing and its applications using inverse boosted input drive signal and cross-beam protocol via C-scan imaging. We have designed a prototype system for cross-beam geometry and pulse compression has been incorporated. As expected short pulse and FM cross-correlation processing provided similar results on the PSF but STFT was slightly worse. SNR improvement via various techniques was quantitatively measured. Since FM cross-correlation and STFT are linear processes, the concept could be extended to tissue mimicking phantom study. We have provided a few cases of indirect experimental validation of the theory. STFT and Wigner-Villet transforms were explained in detail in the presence or absence of additive white noise. Despite all of these tasks, there is much more work to be done.

I. CONTRIBUTIONS OF THIS THESIS

A. Adaptive Inverse Boost Drive Signal

Chapter 4 presented a detailed theoretical treatment of theory behind PSF generated with pulse compression and inverse filtering. Analysis of the possible issues with pulse compression processing has also been discussed. We have derived the input drive signal

which is a rectangular linear chirp weighted by a Butterworth weighting. Experimental RF A-line data were captured for various phantom targets to help understand and analyze the use of the inverse boost technique. There are two steps during this process – the first pass in which a rectangular drive signal whose signal is weighted is impinged on the test target. The RF data from the first pass is used to generate the inverse boost drive signal. Since the transducer response is Gaussian shaped, the effect of the transducer frequency response is corrected by Inverse Boost technique. Samples from positive and negative phantoms were used to compare and constrast the various techniques.

B. Novel Cross-Beam Imaging to improve SNR

Generally in B-scan imaging, the transmit and receive functions are performed by the same transducer. The time duration of linear frequency modulated (LFM) signals gets limited to 10-20 μs, consequently limiting the time-bandwidth product. With separate transmit and receive transducers in cross-beam geometry, we have conquered this limitation. Now, the image has to be created with a C-scan process as described in Chapter 2. Chapter 6 of the dissertation compared and contrasted various processing schemes for this modality. Possibility of using time-frequency distributions such as Short-Time Fourier transform (STFT) and Wigner-Villet (WV) transform were compared to Short Pulse and FM Pulse cross-correlation techniques. The PSF was experimentally measured and evaluated for different schemes. It is a misnomer to look at the output and

call it the PSF. Tiny localized PSF's can be generated only by creating a phantom with very small plastic beads to replicate delta functions. Note that we were not measuring PSF but rather 2D projections of the wire target. The data which could be then back projected to a 3D space which describes accurately the PSF of the target.

C. System Architecture

We have built a prototype imaging system from the ground up which has demonstrated the applications of pulse compression in an ultrasound imaging system. The system is capable of providing any arbitrary input waveform in order to measure and analyze the system point spread function. Our architecture using National Instruments Virtual Instrumentation is a contribution in that it can be used as a framework upon which to build future research activities around pulse compression processing. It allows the researcher to make optimal change to the workflow mechanism to pre- and post-process raw input RF-data to generate B-scan as well as C-scan images.

II. RECOMMENDATIONS FOR FUTURE RESEARCH

This section points out four general aspects of the theory that demand future research.

Increased duration of the interrogating signal

In this research, we had investigated cross-beam geometry using interrogating pulse signals with time duration of 90 μs. Currently there is no limitation on increasing the duration of this signal further to improved SNR in pulse compression. Investigations could be performed to study the experimental limit on the time duration of the interrogating pulse.

Use of Focused transducers

Using cross-beam geometry, we were able to improve resolution only in the Y-direction which depended on the pulse width of the compressed pulse and the selection of the time gate criteria. The resolution along the X-direction was of the order of a few mm's which was controlled by the overlapping beam patterns of the two unfocused transducers. Investigation is required to prove that focused transducers would be able to increase the resolution along the X-direction.

Filtering in the Time-Frequency domain

The effect of noise filtering could be studied using STFT and its inverse as described in Fig. 65.

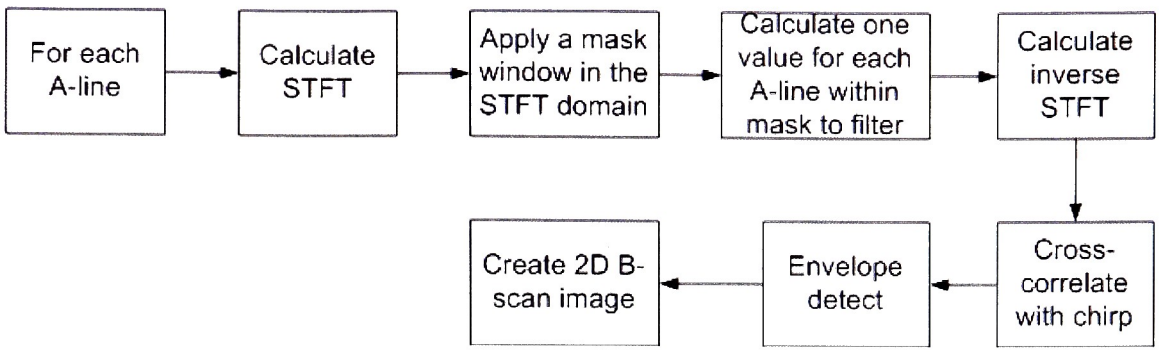

Figure 65: STFT filtering

For each A-line data, the short time fourier transform (STFT) would be calculated. Two scatterers will be distinguishable if they are located at a distance farther than the resolution cell volume. The mask in the time-frequency domain could be selected such that it would selectively filter only the scatterer in question and ignore the others. The energy in the time-frequency domain would now contain information only on the selected scatterer. Inverse STFT of the energy data would provide the time domain signal. These would then get cross-correlated and envelope detected to create the 2D PSF image.

In vivo Tissue Scanning

Most of the experimentation and analysis in this research has been conducted on attenuating and non-attenuating phantoms including wire targets which resemble actual tissue characteristics. It is certainly possible that inverse boost and cross-beam methodologies will perform better when imaging certain tissue types and worse when imaging others. It would be worthwhile to investigate *in vivo* scanning of various tissue

types to study where these techniques could be better suitable. In addition, it would be useful to validate whether LFM drive signals are currently used in commercial ultrasound scanners to understand the real-time processing issues. Clearly this is a long term project and requires reverse engineering the electronics to capture input/output drive/RF signals to/from the system.

Variation in parameters of the STFT

There are various parameters that control the size of the PSF using STFT technique. Investigation of the following parameters are required to understand their effect on the overall PSF:

- Variation in parameters of the slant window
- Variation in parameters of the analysis window
- Investigation of the use of a vertical time gate which represents the instantaneous frequency
- Investigation to understand the tradeoffs between resolution and improvement in SNR

III. POSSIBLE APPLICATIONS OF THIS RESEARCH

Improvement in SNR using both Amplitude Inverse Boost and Cross-beam C-scan scanning in conjunction

This research has shown that improvement in SNR due to the increased bandwidth of the transducer resulted in a 50-70% increase in the effective transducer bandwidth. Further improvement in SNR was made possible by increasing the time duration of the interrogating pulse while operating the transducers in transmit-receive mode using cross-beam geometry. SNR in pulse compression is defined as the product of the time duration of the signal and the bandwidth of the transducer. By utilizing the two methods in conjunction, the overall bandwidth of the system could be further increased.

Scanning using high frequency transducers

This research has investigated the applications of pulse compression using transducers whose center frequency was 5MHz. In traditional commercial ultrasound imaging, transducers with a frequency range less than 10MHz are currently in use. Further improvement in SNR by utilizing transducers in the range 10-20MHz and the artifacts produced needs to be investigated.

Localized scanning in Breast Imaging

An innovative approach using cross-beam scanning could be used to increase the SNR and push the limits of resolution in breast imaging. The proposed methodology

could be incorporated as an adjunct to a stereotactic mammography unit. A small area of size 10mm by 10mm of the suspected lesion in the compressed breast could be further interrogated with two separate transmit/receive high frequency (15-20 MHz) transducers. Since the amount of required scanning area is small, the time taken to scan and process a C-scan image will be minimal.

Chapter 9

REFERENCES

[1] S. Webb, *The Physics of Medical Imaging*, Adam Hilgor, Bristol and Philadelphia, 1988.

[2] A. Macovski, *Medical Imaging Systems*, Information and Systems Science Series, Englewood Cliffs, NJ: Prentice Hall, 1983.

[3] K. K. Shung, M. B. Smith and B. Tsui, *Principles of Medical Imaging*, Academic Press, New York, 1992.

[4] G. S. Kino, *Acoustic Waves, Devices, Imaging and Analog Signal Processing*, John Wiley & Sons, third edition, New York, 1982.

[5] P. N. T. Wells, *Biomedical Ultrasonics*, Academic Press, London, 1977.

[6] J. Beutel, H.L. Kundel and R. L. Van Metter, *Handbook of Medical Imaging*, vol. 1 Physics and Psychophysics, SPIE, ISBN: 0-8194-3621-6, SPIE Order No.: PM79.

[7] P. N. T. Wells, "Ultrasound Imaging," *J. of Biomedical Engineering,* vol. 10, no. 6, pp. 548-554, 1988.

[8] M. I. Skolnik, *Introduction to Radar Systems,* McGraw-Hill, Auckland, 1962.

[9] R. H. Dicke, Object detection system, U.S. Patent No. 2624876, Jan. 6, 1954.

[10] S. Darlington, Pulse transmission, U.S. Patent No. 2678997, May 18, 1954.

[11] C.E. Cook and C.E. Brockner, Pulse-type radar, U.S. Patent 3380054, Apr. 23, 1968.

[12] C.E. Cook and C.E. Brockner, Pulse stretching and compression radar system, U.S. Patent 3400396, Sept. 3, 1968.

[13] C.E. Cook and A.M. Fine, Pulse compression radar, U.S. Patent 3408650, Oct. 29, 1968.

[14] E. Huttman, German Patent No. 768,068, March 22, 1940.

[15] W.A. Cauer, German Patent No. 892, 772, December 19, 1950.

[16] D.O. Sproule and H.J. Hughes, British Patent No. 604,429, July 5, 1948.

[17] J.F. Cerar and C.E. Cook, Electronic means for suppressing range sidelobes and a compressed pulse signal, U.S. Patent 3281842, Oct. 25, 1966.

[18] R.L. Frank, Pulse burst compression radar, U.S. Patent 3090953, May 21, 1963.

[19] C.E. Cook and J.E. Chin, Velocity measuring radar apparatus for high speed vehicles, U.S. Patent 3105967, Oct. 1, 1963.

[20] C.E. Cook and W.M. Siebert, "The Early History of Pulse Compression Radar", *IEEE Trans. Aerospace and Electronic Systems*, vol.24, no.6, pp.825-833, 1988.

[21] P. Phillips, Medical diagnostic ultrasonic imaging system using coded transmit pulses, U.S. Patent 6213947, April 10, 2001.

[22] P. Phillips et al, Medical ultrasound diagnostic imaging method and system with nonlinear phase modulation pulse compression, US Patent 6241674, June 5, 2001.

[23] Y. Takeuchi, "An investigation of a spread energy method for medical ultrasound systems – Part one: theory and investigation", *Ultrasonics*, pp. 175-182, 1979.

[24] D. K. Barton, "Radars Volume 3: Pulse Compression," *Proceedings of the IEEE*, pp.1261, 1963.

[25] B. Boashash, "Estimating and interpreting the instantaneous frequency of a signal – Part 1: Fundamentals," *Proceedings of the IEEE*, vol. 80, no. 4, April 1992.

[26] R. N. Bracewell, *The Fourier Transform and Its Applications*, ISBN No.: 0-07-007013-X, McGraw-Hill Book Company, 1978.

[27] R. N. Bracewell, *Two-dimensional Imaging*, Prentice Hall Signal Processing Series, 1995.

[28] A. R. Brenner, K. Eck, W. Wilhelm and T. G. Noll, "Improved resolution and dynamic range in medical ultrasonic imaging using depth-dependent mismatched filtering," *1997 Symposium of the IEEE Transactions Ultrasonic, Ferroelectrics, Frequency Control,* Toronto, 1997.

[29] C. B. Burckhardt, "Speckle in ultrasound B-mode scans," *IEEE Trans. Sonics and Ultrasonics,* vol. SU-25, no. 1, pp. 1-6, 1978.

[30] C. E. Cook and M. Bernfeld, *Radar Signals – An Introduction to Theory and Application*, Academic Press, New York, 1967.

[31] H. Ermert, M. Pollakowski, C. Passmann and L. von Bernus, "Acoustical imaging using an optimal combination of signal prefiltering and pulse compression," *Acoustical Imaging*, vol.21, 1994.

[32] E. N. Fowle, "The design of FM pulse compression signals," *IEEE Trans. On Information Theory*, pp. 61-67, January 1964.

[33] J. Gaskill, *Linear Systems, Fourier Systems and Optics*. New York: Wiley, 1978.

[34] J. W. Goodman, "Some fundamental properties of speckle," J. of Opt. Soc. Am., vol. 66, no. 11, pp. 1145-1150, 1976.

[35] R.O. Harger, *Synthetic Aperture Radar Systems*, Academic Press, New York 1970.

[36] A. Hob, H. Ermert, S. El-Gammal and P. Altmeyer, "Signal processing in high-frequency broadband imaging systems for dermatological application.

[37] J.A. Jensen, Technical University of Denmark, URL: http://www.it.dtu.dk/~jaj/.

[38] L.F. Joynt, *A Stochastic Approach to Ultrasonic Tissue Characterization*, Ph.D. thesis, Stanford University, Stanford, CA, 1979.

[39] J. R. Klauder, A. C. Price, S. Darlington and W. J. Albersheim, "The theory and design of chirp radars," *Bell Systems Tech. Journal*, vol. 39, pp.745-809, 1960.

[40] Pai-Chi Li, E. Ebbini and M. O'Donnell, "A new filter design technique for coded excitation systems", *IEEE Trans. on Ultrasonics, Ferroelectrics, and Freq. Control,* vol. 39, pp. 700-707, 1992.

[41] Medical Ultrasound Imaging WWW Library, URL: http://www.sunnybrook.utoronto.ca:8080/~donald/us_www.htm.

[42] M. O' Donnell, "Coded excitation system for improving the penetration of real-time phased-array imaging systems," *IEEE Trans. On Ultrasonics, Ferrorelectrics, and Frequency Control*, vol. 39, no.3, pp. 341-351, May 1992.

[43] M. O'Donnell, University of Michigan, URL: http://bul.eecs.umich.edu/~odonnel/.

[44] Y. Ozaki, H. Sumitani, T. Tomoda and M. Tanaka, "A new system for real-time synthetic aperture ultrasonic imaging," *IEEE Transactions on Ultrasonics, Ferroelectrics and Frequency Control*, vol. 35, no. 6, November 1988.

[45] D. K. Peterson and G. S. Kino, "Real-time digital reconstruction: A description of imaging hardware and an analysis of quantization errors," *IEEE Transactions on Sonics and Ultrasonics,* vol. su-31, no. 4, July 1984.

[46] M. Pollakowski and H. Ermet, "Chirp signal matching and signal power optimization in pulse-echo mode ultrasonic nondestructive testing," *IEEE Transactions Ultrasonic, Ferroelectrics, Frequency Control*, 41, pp. 655-659, 1994.

[47] M. Pollakowski, "The application of the pulse-compression technique to ultrasonic non-destructive testing," Ph.D. Dissertation, Verlag Shaker, 1994.

[48] R. Raman and N. Rao, "Pre-enhancement of chirp signal for inverse filtering in medical ultrasound," *Proceedings 16th International Conference of IEEE Engineering in Medicine and Biology Society*, Baltimore, Maryland, vol .1, pp. 676-677, 1994.

[49] N. Rao and M. Aubry, "Evaluation of a pulse compression technique for ultrasound speckle reduction", *Electronic Letters*, 29(8), pp.649-651, 1993.

[50] N. Rao and H. Zhu, "Modelling ultrasound speckle formation and its dependence on imaging systems response", *Proc. SPIE Medical Imaging V: Image Physics*, 1443, pp.81-95, 1991.

[51] N. Rao, "Investigation of a pulse compression technique for medical ultrasound: a simulation study," *Medical & Biological Engineering and Computing*, 32 (2), pp. 181-188, 1994.

[52] N. Rao, S. Mehra, J. Bridges and S. Venkataraman, "Experimental point spread function of FM pulse imaging scheme," *Ultrasonic Imaging*, 17, pp. 114-141, 1995.

[53] J. Schmolke, D. Hiller, H. Ermert, J.O. Schaefer and G. Grabner, "Generation of optimal input signals for ultrasound pulse-echo systems", *1982 Ultrasonics Symposium*, pp. 929-934, 1982.

[54] P.M. Shankar, "Speckle reduction in ultrasound B-scans using weighted averaging in spatial compounding," *IEEE Trans. Ultras., Ferroelect. And Freq. Control,* vol. UFFC-33, no. 6, pp. 754-758, 1986.

[55] P.M. Shankar and V.L. Newhouse, "Speckle reduction with improved resolution in ultrasound images," *IEEE Trans. Sonics and Ultrasonics*, vo. SU-32, no. 4, pp. 537-543, 1985.

[56] G.E. Trahey, J. W. Allison, S. W. Smith and O. T. von Ramm, "A quantitative approach to speckle reduction via frequency compounding," *Ultras. Imag.,* vol. 8, no. 3, pp. 151-164, 1986.

[57] G. E. Trahey, J. W. Allison, S. W. Smith and O. T. von Ramm, "Simultaneous frequency and spatial compunding for increased speckle reduction," *Ultras. Imag.,* vol. 8, no. 1, p. 68, 1986.

[58] S. Venkataraman and N. A. H. K. Rao, "Combining pulse compression and adaptive drive signal design to inverse filter the transducer system response and improve resolution in medical ultrasound," *Medical & Biological Engineering and Computing*, 34, pp. 318-320, 1996.

[59] R.F. Wagner, S.W. Smith, J.M. Sandrik and H. Lopez, "Statistics of speckle in ultrasound B-scans," *IEEE Trans. Sonics and Ultrasonics*, vol. 30, no. 3, pp.156-173, 1983.

[60] R. F. Wagner, M. F. Insana and S. W. Smith, "Fundamental correlation lengths of coherent speckle in medical ultrasonic images," *IEEE Trans. Ultras., Ferroelect. And Freq. Control*, vol. 35, no. 1, pp. 34-44, 1988.

[61] P. M. Woodward, Probability and information theory with applications to radar, Pergamon Press, New York, 1953.

[62] B. Haider, P. A. Lewin and K.E. Thomenius, "Pulse elongation and deconvolution filtering for medical ultrasonic imaging", *IEEE Trans. Ultrason., Ferroelect., and Freq. Contr.*, vol. 45, no. 1, pp. 98-113, Jan. 1998.

[63] G. Hayward and J. Lewis, "A theoretical approach for inverse filter design in ultrasonic applications", *IEEE Trans. Ultrason., Ferroelect., and Freq. Contr.*, vol. 36, pp. 356-364, May 1989.

[64] N. Rao, "Frequency modulated pulse for ultrasonic imaging in an attenuating medium," Proc. 3rd Annual IEEE Symp. On *Computer based medical systems*, 1990, pp. 89-96.

[65] M. A. Malik, X. M. Jin and J. Saniie, "Joint time-frequency processing of ultrasonic signals", *Review of Progress in Quantitative Nondestructive Evaluation,* vol. 15, pp. 2089-2096, edited by D.O. Thompson and D.E. Chimenti, Plenum Press, NY 1996.

[66] M. Fink, F. Hottier and J. F. Cardoso, "Ultrasonic signal processing for in vivo attenuation measurement: Short time fourier analysis", *Ultrasonic Imaging 5,* pp. 117-135, 1983.

[67] S. K. Tang, "On the time-frequency analysis of signals that decay exponentially with time", *Journal of Sound and Vibration,* vol. 234(2), pp. 241-258, 2000.

[68] P. Flandrin, Time-Frequency/Time-Scale Analysis, Academic Press, ISBN 0122598709, San Diego, 1999.

[69] L. Cohen, Time-Frequency Analysis, Prentice-Hall Signal Processing Series, Pearson Education POD, ISBN 0135945321, January 1995.

[70] F. Hlawatsch and G. F. Boudreaux-Bartels, "Linear and Quadratic time-frequency signal representations", *IEEE SP Magazine*, pp. 21-67, April 1992.

[71] S. Qian, Introduction to time frequency and wavelet transforms, Prentice Hall PTR, ISBN 0130303607, November 2001.

[72] L. Cohen, "Time-Frequency Distributions – A Review", *Proceedings of the IEEE*, vol. 77, no. 7, pp. 941-979, July 1989.

[73] E.N. Fowle, "A general method for controlling the Time and Frequency envelopes of FM signals", *Report at MIT Lincoln Laboratory,* June 5, 1961.

[74] R.E. Millett, "A matched-filter pulse-compression system using a nonlinear FM waveform", *IEEE Trans. On Aerospace and Electronic Systems*, vol. AE5-6, no.1, Jan. 1970.

[75] T.X. Misaridis and J.A. Jensen, "An effective coded excitation scheme based on a predistorted FM signal and an optimized digital filter", *1999 IEEE Ultrasonics Symposium*,XXXX.

[76] G.R. Bashford and O.T. von Ramm, "Speckle structure in three dimensions", *J. Acoust. Soc. Am.*, **98** (1), pp. 35-42, July 1995.

[77] J.C. Bamber, *Advances in Ultrasound techniques and Instrumentation*, (ed. Peter Wells), chapter on Speckle Reduction, pp. 55-68, Churchill Livingstone Inc., New York.

[78] J. G. Abbott and F. L. Thurstone, "Acoustic speckle: Theory and experimental analysis", *Ultrason. Imag.*, vol. 1, pp. 303-324, 1979.

[79] C. R. Hill, J. C. Bamber, D. C. Crawford et al, "What might echography learn from imaging science?", *Ultrasound Med. Biol.*, 17:559, 1991.

[80] H. Lopez, M. H. Loew, P.F. Butler et al, "A clinical evaluation of constrast-detail analysis for ultrasound images", *Med. Physics*, 17:48, 1990.

[81] F. W. Kremkau, *Diagnostic Ultrasound: Principles and Instruments*, ISBN: 072169330X, W.B. Saunders, Philadelphia, Jan. 1995.

[82] S. C. Bushong, *Diagnostic ultrasound: Essentials of Medical Imaging Series*, ISBN: 007012017X, McGraw-Hill/Appleton & Lange, Feb. 1999.

[83] E. Brookner, "Phased array radars", *Scientific Amer.*, 252, no. 2, p. 94, 1985.

[84] J. T. Ylitalo and H. Ermert, "Ultrasound synthetic aperture imaging: Monostatic approach", *IEEE Trans. Ultras., Ferroelect. And Freq. Control*, vol. 41, no. 3, May 1994.

[85] G. S. Jeng, S. Huang, P. C. Li and J. Tsao, "A novel pulse compression technique using inverse filtering in frequency domain", *2001 IEEE Ultrasonics Symposium*, pp. 1535-1538, 2001.

[86] C. A. Hwang and R. J. Keeler, "Sample phase aspects of FM pulse compression waveform", *1995 IEEE*, pp. 2126-2128, 1995.

[87] Z. Qunying, Y. Xuexian and H. Yueqiu, "Effect of sampling rate on SNR in digital pulse compression system", pp. 23-26, 1998.

[88] J. Shen and E. S. Ebbini, "A new coded-excitation ultrasound imaging system – Part I: Basic principles", *IEEE Trans. Ultras., Ferroelect. And Freq. Control*, vol. 43, no. 1, pp.131-140, Jan. 1996.

[89] J. Shen and E. S. Ebbini, "A new coded-excitation ultrasound imaging system – Part II: Basic principles", *IEEE Trans. Ultras., Ferroelect. And Freq. Control*, vol. 43, no. 1, pp.141-148, Jan. 1996.

[90] A. Zeira, E. M. Zeira and S. K. Holland, "Pseudo-Wigner distribution for analysis of pulsed Doppler ultrasound", *IEEE Trans. Ultras., Ferroelect. And Freq. Control*, vol. 41, no. 3, May 1994.

[91] S. I. Parks and M. Linzer, "Application of pulse compression technique to medical ultrasound", in 1976 Proc. Of SPIE: *Optical Instrumentation in Medicine V*, vol. 96, pp. 349-353, 1976.

[92] N. Rao and M. Aubry, "Evaluation of a pulse compression technique for spatial structure characterization", *IEEE Trans. Ultras., Ferroelect. And Freq. Control* , vol. 41, pp.660-663, 1994.

[93] K.V. Gurumurthy and R. M. Arthur, "A dispersive model for the propagation of ultrasound in soft tissue", *Ultrasonic Imaging*, 4, pp. 355-377, 1981.

[94] A. C. Kak and K. A. Dines, "Signal processing of broadband pulsed ultrasound", *IEEE Trans. Biomed. Eng.*, BME-25, pp. 321-344, 1978.

[95] E. L. Key, E. N. Fowle and R. D. Haggarty, "A method of designing signals of large time-bandwidth product," *IRE Intl. Convention Record*, pt. 4, pp. 146-155, 1961.

[96] F. Auger, P. Flandrin, O. Lemoine and P. Goncalves, "Time-Frequency Toolbox for Matlab", http://crttsn.univ-nantes.fr/~auger/tftb.html.

[97] J. Lee and J. Kim, "Development of enhanced Wigner-Ville distribution function", *Mech. Systems and Signal Processing*, vol. 15, no.2, pp. 367-398, 2001.

[98] H. Mendonca, J. Machado da Silva and J. S. Matos, "ADC testing using joint time-frequency analysis", *Computer Standards and Interfaces*, vol. 23, pp. 129-135, 2001.

[99] P. Flandrin and P. Goncalves, "Geometry of Affine Time-Frequency distributions", *Applied and Computational Harmonic Analysis*, vol. 3, pp. 10-39, 1996.

[100] G. Cloutier, D. Chen and L. Durand, "Performance of time-frequency representation techniques to measure blood flow turbulence with pulsed-wave doppler ultrasound", *Ultras. In Med. & Biol.*, vol. 27, no. 4, pp. 535-550, 2001.

[101] K. J. W. Taylor et. al, "Ultrasound as a complement to mammography and breast examination to characterize breast masses", *Ultras. In Med. & Biol.*, vol. 28, no. 1, pp. 19-26, 2002.

[102] J. Carson and T. Fry, "Variable frequency electric circuit theory with application to the theory of frequency modulation", *Bell System Tech. J.*, vol. 16, pp. 513-540, 1937.

[103] B. Van der Pol, "The fundamental principles of frequency modulation," *Proc. IEE*, vol. 93 (III), pp. 153-158, 1946.

10. APPENDICES

This research utilized MATLAB V6.5.1 as the algorithm developing tool. A collection of program scripts developed for the calculation of envelope, PSF, generating inverse boosted signal, time-frequency domain processing, etc. are listed in the appendices that follow. When running the attached program scripts related to time-frequency analysis, the time-frequency toolbox created by F. Auger, P. Flandrin, O. Lemoine and P. Goncalves should be installed and was indispensable. User should include the "tftb" files and subfolders to the search path when working with the MATLAB environment. The program scripts developed for each module of this research are shown in the following appendices.

APPENDIX A: TRANSDUCER CHARACTERISTICS

The ultrasonic transducers used during the imaging experiments were Accuscan paintbrush transducers. An important advantage of this design is that it minimizes objectionable sensitivity peaks due to diffraction effects at the ends of each transducer element. The factory default characteristics are described below:

Transducer Description

a. For the Amplitude Boost Experimentation

P/N: ACCUSCAN-S Frequency: 2.25MHz

S/N: A306S-SU Element size: 0.375 inches

Designation: Immersion type

b. For the Cross-beam geometry Experimentation

In this case, two transducers were used, one for the transmit and the other for the receive mode. Both the transducers operated at 5MHZ.

(i) Transmit mode

P/N: ACCUSCAN-S Frequency: 5MHz

S/N: A326S-SU Element size: 0.375 inches

Designation: Immersion type

(ii) Receive mode

P/N: ACCUSCAN-S Frequency: 5MHz

S/N: A310-SU Element size: 0.25 inches

Designation: Immersion type

APPENDIX B: LABVIEW PROGRAM

National Instruments LabView is a graphical development environment used to create flexible and scalable test, measurement and control applications rapidly. During the second half of our research, the synthetic waveform generator and digitizer were replaced by two PCI bus based cards that were installed on the PC. Instrumentation components were created using Labview IVI in order to control input/output (I/O), stepper motor, waveform generator and digitizer. The following Virtual Instrument (VI) panel was created to display, capture and store 1D RF data to the monitor/file systems. The same user interface (UI) was also used to control the position, direction and revolution step size of the XY stepper motors.

SaveData5112.vi:

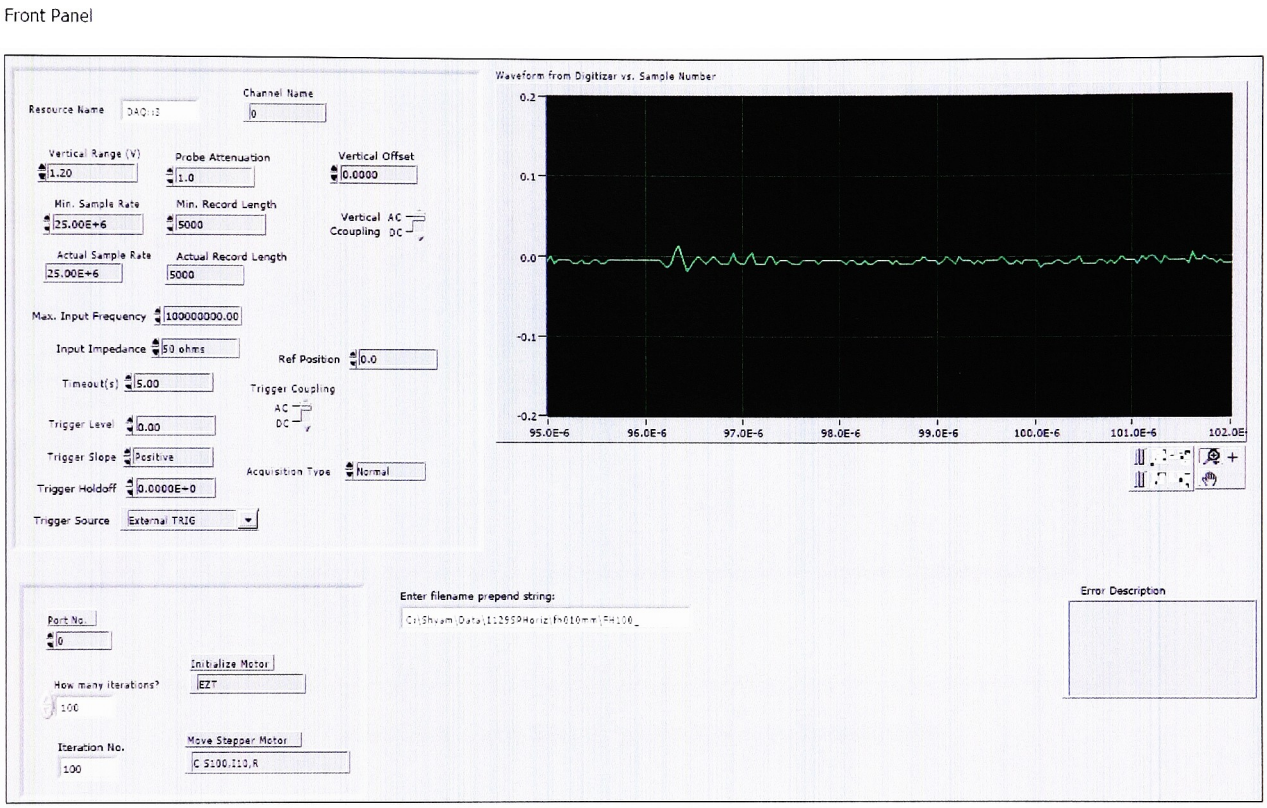

Figure 1: Custom Virtual Instrument used to control the ultrasound imaging system

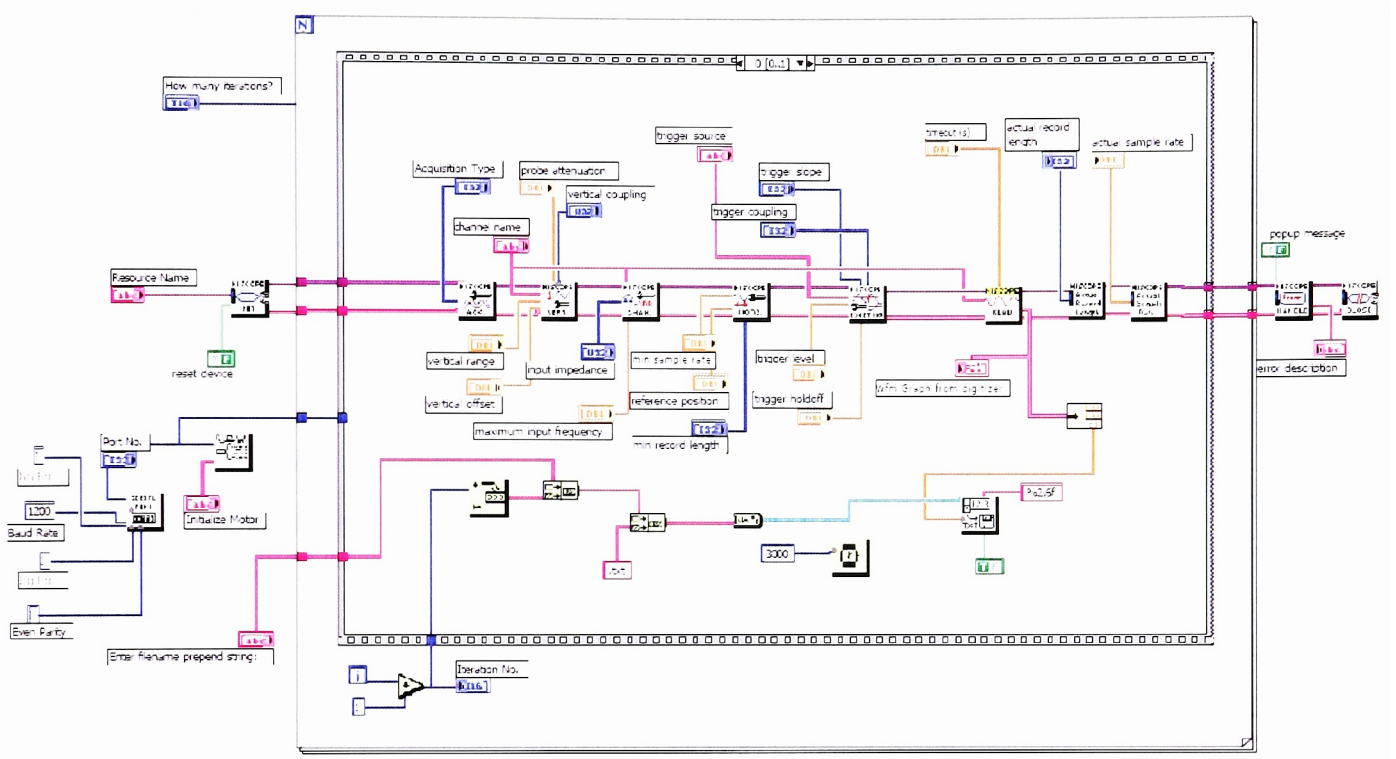

Figure 2: VI components connected to create a process imaging pipe

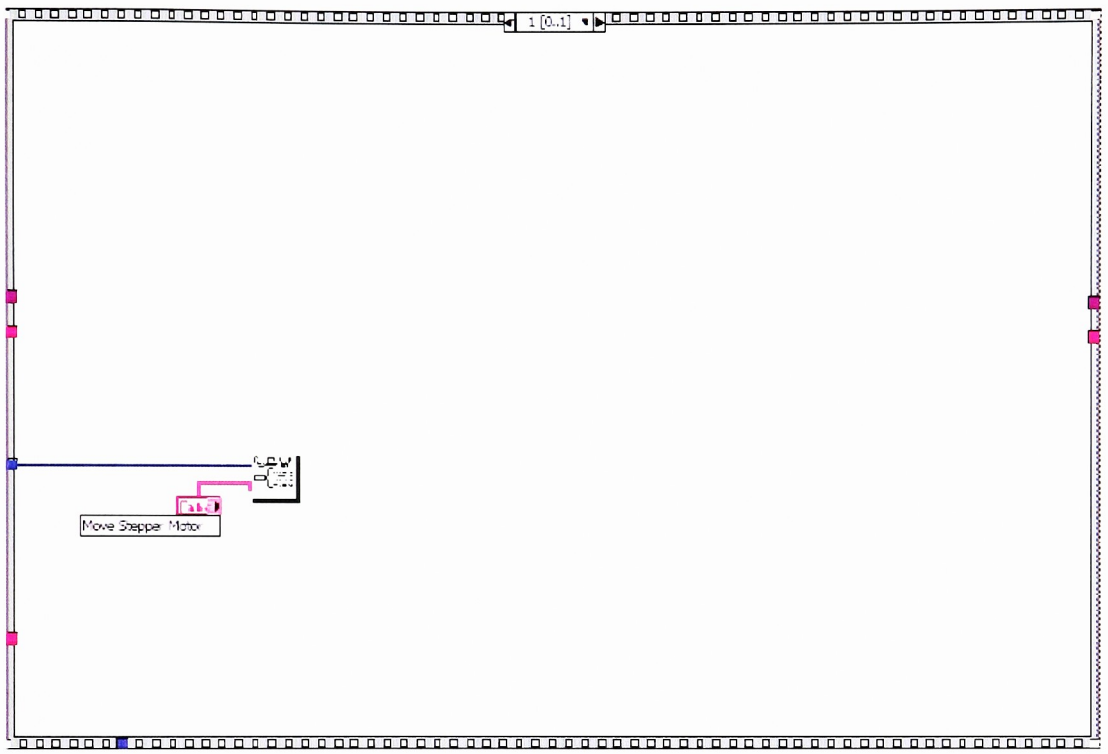

Figure 3: Second page of the VI depicting the stepper motor control

APPENDIX C: CHARACTERISTICS OF MATERIALS IN SOUND

Material	Speed, c ms^{-1}	Acoustic impedance, z $kg\ m^{-2}\ s^{-1}$	Attenuation $dB\ cm^{-1}\ MHz^{-1}$
Water	1497	1.49	0.001
Air	330		10 $dB\ cm^{-1}$ @ 1 MHz
Bone	2900	5.37	4.06
Liver, Pig	1570	1.67	0.11
Lung			40 $dB\ cm^{-1}$ @ 1 MHz
Muscle	1585		1.65-1.75 $dB\ cm^{-1}$ @ 1 MHz
Fat, Pig	1479	1.39	0.30
Blood	1580	1.67	0.11
Aluminum	6419	17.33	0.006
Glass, Pyrex	5640	12.63	0.001